# Site U1599[1]

T.H. Druitt, S. Kutterolf, T.A. Ronge, S. Beethe, A. Bernard, C. Berthod, H. Chen, S. Chiyonobu, A. Clark, S. DeBari, T.I. Fernandez Perez, R. Gertisser, C. Hübscher, R.M. Johnston, C. Jones, K.B. Joshi, G. Kletetschka, O. Koukousioura, X. Li, M. Manga, M. McCanta, I. McIntosh, A. Morris, P. Nomikou, K. Pank, A. Peccia, P.N. Polymenakou, J. Preine, M. Tominaga, A. Woodhouse, and Y. Yamamoto[2]

**Keywords**

**Core descriptions**

**Supplementary material**

**References (RIS)**

## 1. Background and objectives

Site U1599 is located ~6 km north of Anafi Island within the upper reaches of the Anafi Basin at a water depth of 592 meters below sea level (mbsl) (Figure **F1**). Permission to drill in this location was granted by the International Ocean Discovery Program (IODP) Environmental Protection and Safety Panel during the expedition (proposed Site CSK-22A). Three holes (U1599A–U1599C) were drilled to a maximum recovery depth of 698.1 meters below seafloor (mbsf) (all depths below seafloor are given using the core depth below seafloor, Method A [CSF-A] scale, except in **Operations**, where the drilling depth below seafloor [DSF] scale is used), with average hole core recoveries ranging 51%–83% (Figure **F2**).

Whereas Site U1592 is situated on the axis of the Anafi Basin and penetrated a thick basin fill including mass-transported material, Site U1599 is located on the southeast margin of the basin. It was chosen to offer a condensed sequence of tephra without quantities of mass-wasting debris. As
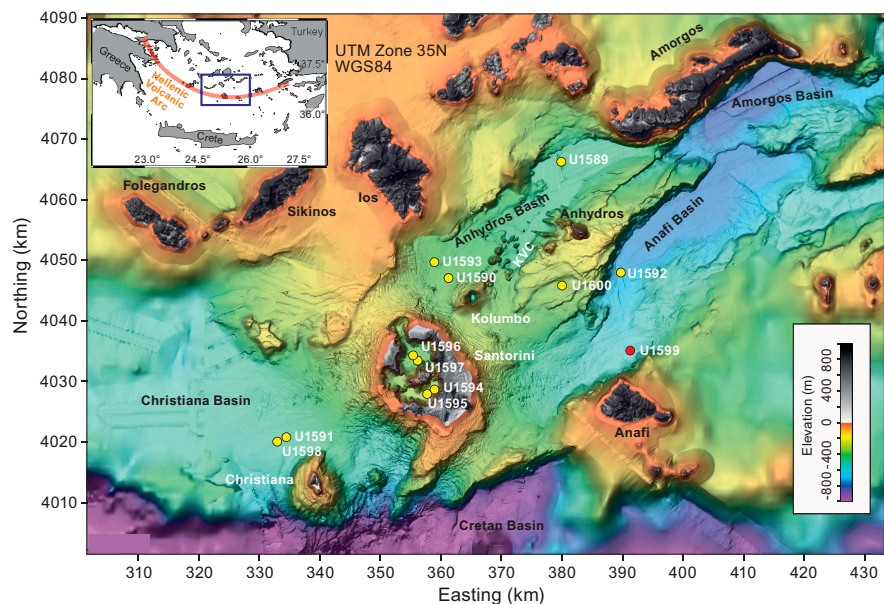


**Figure F1.** Site map. Red = Site U1599, yellow = other sites. Inset = location map. See Figure F1 in the Site U1589 chapter (Druitt et al., 2024a) for the swath data on which this map is based. KVC = Kolumbo volcanic chain.
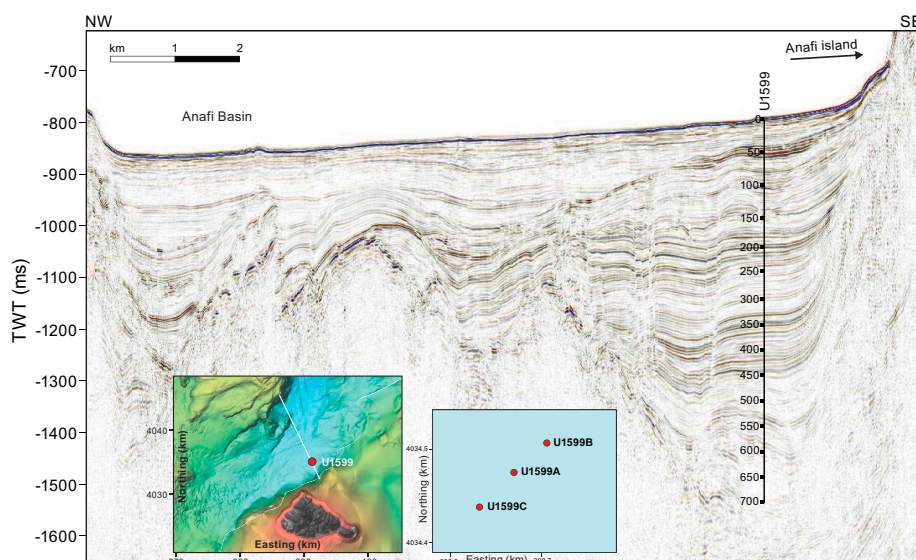
**Figure F2.** Seismic profile across the Anhydros Basin along Seismic Line HH06-16. Insets: location of Site U1599 and Holes U1599A–U1599C. Depths in meters. TWT = two-way traveltime.

such, it provided a complete stratigraphy of volcanic tephra from Santorini and Kolumbo. The same six seismic units (U1–U6, from the bottom up; Preine et al., 2022a, 2022b) present at Site U1592 are present at Site U1599. Site U1599 is located within the area of the 2015 PROTEUS seismic tomography experiment, during which subbottom profiling, gravity, and magnetic data were also recorded (Hooft et al., 2017).

Drilling at Site U1599 enabled us to reconstruct a near-complete volcanic stratigraphy consistent with both onshore and offshore constraints and pinned by chronological markers from biostratigraphy, magnetostratigraphy, and sapropel records. Benthic foraminifera from fine-grained sediments provided estimates of paleowater depths and, via integration with seismic profiles and chronologic data, of time-integrated basin subsidence rates. Drilling in the Anafi Basin addressed scientific Objectives 1–4 and 6 of the Expedition 398 Scientific Prospectus (Druitt et al., 2022). It was complemented by Site U1589 in the Anhydros Basin because each basin tapped a different sediment distributary branch of the Christiana-Santorini-Kolumbo volcanic system.

## 2. Operations

The vessel arrived at Site U1599 on 25 January 2023 at 2115 h, ending the transit and marking the start of Site U1599.

### 2.1. Hole U1599A

The crew made up the advanced piston corer/extended core barrel (APC/XCB) bottom hole assembly (BHA) with a bit. The BHA was run in to 585.7 meters below rig floor (mbrf). On 26 January 2023, following 12.75 h awaiting approval for the site, the go-ahead was given at 1315 h. The APC barrel was fired for Core 1H from 599.0 mbrf. Once retrieved, it was discovered the core barrel had parted at the midconnection. The pipe tally and the precision depth recorder were verified. A second attempt was made with the APC system; unfortunately, the result was the same—a parted core barrel.

An XCB barrel was dropped. Hole U1599A (36°26.9592′N, 25°46.8005′E) was spudded at 1535 h with a solid tag at 602.5 mbrf. After retrieval, the barrel had zero recovery, but it was obvious the coring system had been in the ground.

Given continuing uncertainty of the stiffness of the formation, the coring approach was switched to half-length APC (HLAPC) for Core 2F from 9.7 mbsf. The 97% recovery showed the material was suitable for piston coring. It was assumed there was some tightly compacted layer at the mudline.

Coring was then switched to the APC system with Cores 3H–9H at 71.4 mbsf (Table T1). The formation stiffened up quickly, forcing the change to HLAPC coring for Core 10F and all the way through Core 44F to 245.4 mbsf, the final depth for Hole U1599A. There was an unsuccessful overpull of 60,000 lb on Core 44F. An attempt was made to drill over the barrel for ~30 min. The driller aired down the compensator and applied 100,000 lb overpull, which freed the barrel. The decision was made to terminate the hole.

**Table T1.** Core summary, Site U1599. mbsf = meters below seafloor. NA = not applicable. DSF = drilling depth below seafloor. X = XCB, F = HLAPC, H = APC, numeric core type = drilled interval, R = RCB. (Continued on next two pages.) **Download table in CSV format.**

**Hole U1599A**
Latitude: 36°26.9592′N
Longitude: 25°46.8005′E
Water depth (m): 591.19
Date started (UTC): 1915 h; 25 January 2023
Date finished (UTC): 1945 h; 27 January 2023
Time on hole (days): 2.02
Penetration (mbsf): 245.4
Cored interval (m): 245.4
Recovered length (m): 204.57
Recovery (%): 83.36
Drilled interval (m): NA
Drilled interval (no.): 0
Total cores (no.): 44
APC cores (no.): 7
HLAPC cores (no.): 36
XCB cored (no.): 1

**Hole U1599B**
Latitude: 36°26.9764′N
Longitude: 25°46.8237′E
Water depth (m): 591.68
Date started (UTC): 1945 h; 27 January 2023
Date finished (UTC): 0130 h; 29 January 2023
Time on hole (days): 1.24
Penetration (mbsf): 241
Cored interval (m): 241
Recovered length (m): 199.13
Recovery (%): 82.63
Drilled interval (m): NA
Drilled interval (no.): 0
Total cores (no.): 40
APC cores (no.): 10
HLAPC cores (no.): 29
XCB cored (no.): 1

**Hole U1599C**
Latitude: 36°26.9389′N
Longitude: 25°46.7762′E
Water depth (m): 592.68
Date started (UTC): 1315 h; 30 January 2023
Date finished (UTC): 2345 h; 1 February 2023
Reentered (UTC): 0230 h; 7 February 2023
Finished (UTC): 1945 h; 9 February 2023
Time on hole (days): 4.6
Penetration (mbsf): 697.8
Cored interval (m): 474.8
Recovered length (m): 244.18
Recovery (%): 51.43
Drilled interval (m): 233
Drilled interval (no.): 1
Total cores (no.): 49
RCB cores (no.): 49

| Core | Top depth drilled DSF (m) | Bottom depth drilled DSF (m) | Interval advanced (m) | Recovered length (m) | Core recovery (%) | Core on deck date (2023) | Core on deck time UTC (h) |
|---|---|---|---|---|---|---|---|
| 398-U1599A- | | | | | | | |
| 1X | 0.0 | 9.7 | 9.7 | 0.00 | 0 | 26 Jan | 1400 |
| 2F | 9.7 | 14.4 | 4.7 | 4.55 | 97 | 26 Jan | 1440 |
| 3H | 14.4 | 23.9 | 9.5 | 8.65 | 91 | 26 Jan | 1525 |
| 4H | 23.9 | 33.4 | 9.5 | 9.66 | 102 | 26 Jan | 1640 |
| 5H | 33.4 | 42.9 | 9.5 | 10.16 | 107 | 26 Jan | 1705 |
| 6H | 42.9 | 52.4 | 9.5 | 3.60 | 38 | 26 Jan | 1735 |
| 7H | 52.4 | 61.9 | 9.5 | 9.84 | 104 | 26 Jan | 1805 |
| 8H | 61.9 | 71.4 | 9.5 | 7.74 | 81 | 26 Jan | 1850 |
| 9H | 71.4 | 80.9 | 9.5 | 9.95 | 105 | 26 Jan | 1940 |
| 10F | 80.9 | 85.6 | 4.7 | 4.70 | 100 | 26 Jan | 2015 |
| 11F | 85.6 | 90.3 | 4.7 | 1.94 | 41 | 26 Jan | 2035 |
| 12F | 90.3 | 95.0 | 4.7 | 5.04 | 107 | 26 Jan | 2105 |
| 13F | 95.0 | 99.7 | 4.7 | 4.91 | 104 | 26 Jan | 2130 |
| 14F | 99.7 | 104.4 | 4.7 | 4.77 | 101 | 26 Jan | 2155 |

**Table T1 (continued).** (Continued on next page.)

| Core | Top depth drilled DSF (m) | Bottom depth drilled DSF (m) | Interval advanced (m) | Recovered length (m) | Core recovery (%) | Core on deck date (2023) | Core on deck time UTC (h) |
|---|---|---|---|---|---|---|---|
| 15F | 104.4 | 109.1 | 4.7 | 4.87 | 104 | 26 Jan | 2240 |
| 16F | 109.1 | 113.8 | 4.7 | 4.42 | 94 | 26 Jan | 2310 |
| 17F | 113.8 | 118.5 | 4.7 | 5.00 | 106 | 26 Jan | 2335 |
| 18F | 118.5 | 123.2 | 4.7 | 4.90 | 104 | 27 Jan | 0000 |
| 19F | 123.2 | 127.9 | 4.7 | 4.94 | 105 | 27 Jan | 0045 |
| 20F | 127.9 | 132.6 | 4.7 | 4.89 | 104 | 27 Jan | 0115 |
| 21F | 132.6 | 137.3 | 4.7 | 4.16 | 89 | 27 Jan | 0150 |
| 22F | 137.3 | 142.0 | 4.7 | 4.55 | 97 | 27 Jan | 0240 |
| 23F | 142.0 | 146.7 | 4.7 | 4.44 | 94 | 27 Jan | 0325 |
| 24F | 146.7 | 151.4 | 4.7 | 4.90 | 104 | 27 Jan | 0400 |
| 25F | 151.4 | 156.1 | 4.7 | 2.47 | 53 | 27 Jan | 0430 |
| 26F | 156.1 | 160.8 | 4.7 | 2.94 | 63 | 27 Jan | 0505 |
| 27F | 160.8 | 165.5 | 4.7 | 3.15 | 67 | 27 Jan | 0540 |
| 28F | 165.5 | 170.2 | 4.7 | 4.29 | 91 | 27 Jan | 0610 |
| 29F | 170.2 | 174.9 | 4.7 | 4.58 | 97 | 27 Jan | 0635 |
| 30F | 174.9 | 179.6 | 4.7 | 4.04 | 86 | 27 Jan | 0710 |
| 31F | 179.6 | 184.3 | 4.7 | 3.82 | 81 | 27 Jan | 0730 |
| 32F | 184.3 | 189.0 | 4.7 | 0.00 | 0 | 27 Jan | 0815 |
| 33F | 189.0 | 193.7 | 4.7 | 4.55 | 97 | 27 Jan | 0840 |
| 34F | 193.7 | 198.4 | 4.7 | 2.66 | 57 | 27 Jan | 0915 |
| 35F | 198.4 | 203.1 | 4.7 | 3.82 | 81 | 27 Jan | 1040 |
| 36F | 203.1 | 207.8 | 4.7 | 0.01 | 0 | 27 Jan | 1130 |
| 37F | 207.8 | 212.5 | 4.7 | 5.00 | 106 | 27 Jan | 1205 |
| 38F | 212.5 | 217.2 | 4.7 | 4.58 | 97 | 27 Jan | 1250 |
| 39F | 217.2 | 221.9 | 4.7 | 1.31 | 28 | 27 Jan | 1330 |
| 40F | 221.9 | 226.6 | 4.7 | 4.82 | 103 | 27 Jan | 1355 |
| 41F | 226.6 | 231.3 | 4.7 | 4.92 | 105 | 27 Jan | 1430 |
| 42F | 231.3 | 236.0 | 4.7 | 4.98 | 106 | 27 Jan | 1525 |
| 43F | 236.0 | 240.7 | 4.7 | 5.06 | 108 | 27 Jan | 1600 |
| 44F | 240.7 | 245.4 | 4.7 | 4.99 | 106 | 27 Jan | 1750 |
| 398-U1599B- | | | | | | | |
| 1X | 0.0 | 9.7 | 9.7 | 0.00 | 0 | 27 Jan | 2155 |
| 2H | 9.7 | 19.2 | 9.5 | 5.19 | 55 | 27 Jan | 2230 |
| 3H | 19.2 | 28.7 | 9.5 | 8.75 | 92 | 27 Jan | 2310 |
| 4H | 28.7 | 38.2 | 9.5 | 9.71 | 102 | 27 Jan | 2345 |
| 5H | 38.2 | 47.7 | 9.5 | 9.77 | 103 | 28 Jan | 0040 |
| 6H | 47.7 | 57.2 | 9.5 | 6.10 | 64 | 28 Jan | 0110 |
| 7H | 57.2 | 66.7 | 9.5 | 9.59 | 101 | 28 Jan | 0145 |
| 8H | 66.7 | 76.2 | 9.5 | 9.79 | 103 | 28 Jan | 0215 |
| 9H | 76.2 | 85.7 | 9.5 | 6.72 | 71 | 28 Jan | 0250 |
| 10H | 85.7 | 95.2 | 9.5 | 9.63 | 101 | 28 Jan | 0330 |
| 11H | 95.2 | 104.7 | 9.5 | 10.00 | 105 | 28 Jan | 0400 |
| 12F | 104.7 | 109.4 | 4.7 | 4.41 | 94 | 28 Jan | 0505 |
| 13F | 109.4 | 114.1 | 4.7 | 4.82 | 103 | 28 Jan | 0530 |
| 14F | 114.1 | 118.8 | 4.7 | 4.85 | 103 | 28 Jan | 0550 |
| 15F | 118.8 | 123.5 | 4.7 | 5.00 | 106 | 28 Jan | 0615 |
| 16F | 123.5 | 128.2 | 4.7 | 5.03 | 107 | 28 Jan | 0640 |
| 17F | 128.2 | 132.9 | 4.7 | 4.98 | 106 | 28 Jan | 0700 |
| 18F | 132.9 | 137.6 | 4.7 | 5.03 | 107 | 28 Jan | 0810 |
| 19F | 137.6 | 142.3 | 4.7 | 3.97 | 84 | 28 Jan | 0835 |
| 20F | 142.3 | 147.0 | 4.7 | 3.02 | 64 | 28 Jan | 0900 |
| 21F | 147.0 | 151.7 | 4.7 | 4.70 | 100 | 28 Jan | 0920 |
| 22F | 151.7 | 156.4 | 4.7 | 1.60 | 34 | 28 Jan | 0945 |
| 23F | 156.4 | 161.1 | 4.7 | 2.00 | 43 | 28 Jan | 1010 |
| 24F | 161.1 | 165.8 | 4.7 | 2.46 | 52 | 28 Jan | 1045 |
| 25F | 165.8 | 170.5 | 4.7 | 4.40 | 94 | 28 Jan | 1125 |
| 26F | 170.5 | 175.2 | 4.7 | 4.88 | 104 | 28 Jan | 1145 |
| 27F | 175.2 | 179.9 | 4.7 | 4.09 | 87 | 28 Jan | 1210 |
| 28F | 179.9 | 184.6 | 4.7 | 1.61 | 34 | 28 Jan | 1230 |
| 29F | 184.6 | 189.3 | 4.7 | 3.65 | 78 | 28 Jan | 1315 |
| 30F | 189.3 | 194.0 | 4.7 | 2.46 | 52 | 28 Jan | 1355 |
| 31F | 194.0 | 198.7 | 4.7 | 1.96 | 42 | 28 Jan | 1430 |
| 32F | 198.7 | 203.4 | 4.7 | 3.77 | 80 | 28 Jan | 1510 |
| 33F | 203.4 | 208.1 | 4.7 | 4.65 | 99 | 28 Jan | 1610 |
| 34F | 208.1 | 212.8 | 4.7 | 4.70 | 100 | 28 Jan | 1640 |
| 35F | 212.8 | 217.5 | 4.7 | 2.10 | 45 | 28 Jan | 1715 |
| 36F | 217.5 | 222.2 | 4.7 | 4.72 | 100 | 28 Jan | 1820 |
| 37F | 222.2 | 226.9 | 4.7 | 4.27 | 91 | 28 Jan | 1900 |
| 38F | 226.9 | 231.6 | 4.7 | 4.88 | 104 | 28 Jan | 1945 |

**Table T1 (continued).**

| Core | Top depth drilled DSF (m) | Bottom depth drilled DSF (m) | Interval advanced (m) | Recovered length (m) | Core recovery (%) | Core on deck date (2023) | Core on deck time UTC (h) |
|---|---|---|---|---|---|---|---|
| 39F | 231.6 | 236.3 | 4.7 | 4.95 | 105 | 28 Jan | 2020 |
| 40F | 236.3 | 241.0 | 4.7 | 4.92 | 105 | 28 Jan | 2120 |
| 398-U1599C- | | | | | | | |
| 11 | 0.0 | 223.0 | 223.0 | ****Drilled interval**** | | 31 Jan | 0240 |
| 2R | 223.0 | 232.5 | 9.5 | 8.08 | 85 | 31 Jan | 0425 |
| 3R | 232.5 | 242.1 | 9.6 | 5.67 | 59 | 31 Jan | 0545 |
| 4R | 242.1 | 251.8 | 9.7 | 8.96 | 92 | 31 Jan | 0705 |
| 5R | 251.8 | 261.5 | 9.7 | 4.91 | 51 | 31 Jan | 0800 |
| 6R | 261.5 | 271.2 | 9.7 | 6.87 | 71 | 31 Jan | 0920 |
| 7R | 271.2 | 280.9 | 9.7 | 8.85 | 91 | 31 Jan | 1045 |
| 8R | 280.9 | 290.6 | 9.7 | 4.51 | 46 | 31 Jan | 1215 |
| 9R | 290.6 | 300.3 | 9.7 | 6.60 | 68 | 31 Jan | 1345 |
| 10R | 300.3 | 310.0 | 9.7 | 0.17 | 2 | 31 Jan | 1530 |
| 11R | 310.0 | 319.7 | 9.7 | 9.94 | 102 | 31 Jan | 1705 |
| 12R | 319.7 | 329.4 | 9.7 | 0.00 | 0 | 31 Jan | 1845 |
| 13R | 329.4 | 339.1 | 9.7 | 5.21 | 54 | 31 Jan | 2035 |
| 14R | 339.1 | 348.8 | 9.7 | 2.61 | 27 | 31 Jan | 2155 |
| 15R | 348.8 | 358.5 | 9.7 | 4.00 | 41 | 31 Jan | 2340 |
| 16R | 358.5 | 368.2 | 9.7 | 0.17 | 2 | 1 Feb | 0115 |
| 17R | 368.2 | 377.9 | 9.7 | 7.09 | 73 | 1 Feb | 0250 |
| 18R | 377.9 | 387.6 | 9.7 | 0.02 | 0 | 1 Feb | 0415 |
| 19R | 387.6 | 397.3 | 9.7 | 9.03 | 93 | 1 Feb | 0600 |
| 20R | 397.3 | 407.0 | 9.7 | 8.67 | 89 | 1 Feb | 0720 |
| 21R | 407.0 | 416.7 | 9.7 | 0.04 | 0 | 1 Feb | 0845 |
| 22R | 416.7 | 426.4 | 9.7 | 9.34 | 96 | 1 Feb | 1015 |
| 23R | 426.4 | 436.1 | 9.7 | 0.00 | 0 | 1 Feb | 1140 |
| 24R | 436.1 | 445.8 | 9.7 | 7.57 | 78 | 1 Feb | 1310 |
| 25R | 445.8 | 455.5 | 9.7 | 4.46 | 46 | 1 Feb | 1440 |
| 26R | 455.5 | 465.2 | 9.7 | 5.86 | 60 | 7 Feb | 1320 |
| 27R | 465.2 | 474.9 | 9.7 | 4.40 | 45 | 7 Feb | 1500 |
| 28R | 474.9 | 484.6 | 9.7 | 3.29 | 34 | 7 Feb | 1625 |
| 29R | 484.6 | 494.3 | 9.7 | 4.15 | 43 | 7 Feb | 1815 |
| 30R | 494.3 | 504.0 | 9.7 | 3.32 | 34 | 7 Feb | 1945 |
| 31R | 504.0 | 513.7 | 9.7 | 4.92 | 51 | 7 Feb | 2125 |
| 32R | 513.7 | 523.4 | 9.7 | 7.37 | 76 | 7 Feb | 2300 |
| 33R | 523.4 | 533.1 | 9.7 | 5.12 | 53 | 8 Feb | 0030 |
| 34R | 533.1 | 542.8 | 9.7 | 2.47 | 25 | 8 Feb | 0210 |
| 35R | 542.8 | 552.5 | 9.7 | 1.41 | 15 | 8 Feb | 0330 |
| 36R | 552.5 | 562.2 | 9.7 | 3.25 | 34 | 8 Feb | 0550 |
| 37R | 562.2 | 571.9 | 9.7 | 6.40 | 66 | 8 Feb | 0810 |
| 38R | 571.9 | 581.6 | 9.7 | 8.71 | 90 | 8 Feb | 1040 |
| 39R | 581.6 | 591.3 | 9.7 | 7.81 | 81 | 8 Feb | 1240 |
| 40R | 591.3 | 601.0 | 9.7 | 7.25 | 75 | 8 Feb | 1445 |
| 41R | 601.0 | 610.7 | 9.7 | 7.87 | 81 | 8 Feb | 1655 |
| 42R | 610.7 | 620.4 | 9.7 | 3.16 | 33 | 8 Feb | 1850 |
| 43R | 620.4 | 630.1 | 9.7 | 3.32 | 34 | 8 Feb | 2035 |
| 44R | 630.1 | 639.8 | 9.7 | 0.04 | 0 | 8 Feb | 2155 |
| 45R | 639.8 | 649.5 | 9.7 | 0.02 | 0 | 8 Feb | 2325 |
| 46R | 649.5 | 659.2 | 9.7 | 0.22 | 2 | 9 Feb | 0055 |
| 47R | 659.2 | 668.9 | 9.7 | 4.38 | 45 | 9 Feb | 0325 |
| 48R | 668.9 | 678.6 | 9.7 | 8.35 | 86 | 9 Feb | 0620 |
| 49R | 678.6 | 688.2 | 9.6 | 8.51 | 89 | 9 Feb | 0915 |
| 50R | 688.2 | 697.8 | 9.6 | 9.81 | 102 | 9 Feb | 1255 |
| | | Totals: | 1184.2 | 647.88 | | | |

The string was pulled up with the top drive from 240.7 to 185.4 mbsf, and the bit cleared the seafloor at 2145 h, ending Hole U1599A.

## 2.2. Hole U1599B

The vessel was offset 50 m northeast of Hole U1599A, and the seafloor was tagged at 604.0 mbsf. Hole U1599B (36°26.9764′N, 25°46.8237′E) was spudded at 2330 h on 27 January 2023 with Core 1X to 9.7 mbsf. Coring was switched to the APC system for Cores 2H–11H at 95.2 mbsf. Overpulls of 35,000 and 30,000 lb were seen on Cores 10H and 11H, respectively. Coring was again switched,

this time to the HLAPC system, for Core 12F from 104.7 mbsf through Core 40F at 241.0 mbsf, the final depth for Hole U1599B.

The drill string was tripped up with the top drive, and the bit cleared the seafloor at 0100 h and the rotary table at 0255 h. The drill floor was secured, and the thrusters were raised starting at 0324 h. All thrusters were up and secure, the vessel was under bridge control, and the sea passage started at 0336 h.

## 2.3. Hole U1599C

Hole U1599C (36°26.9389′N, 25°46.7762′E) was spudded on 30 January 2023 at 1925 h. A seafloor depth of 604.0 mbrf was used by offset. Drill-ahead without recovery progressed to 223.0 mbsf at 0445 h. RCB coring commenced with Core 2R on 30 January and proceeded through 1 February and Core 25R to 455.5 mbsf. The drill string was tripped from 455.5 to 404.9 mbsf. The top drive was racked back, and the pipe trip up continued to 55.6 mbsf.

Next, the rig crew pulled the upper guide horn (UGH) in preparation for launching a free-fall funnel (FFF). The FFF was assembled and welded in the moonpool. The FFF was launched at 2005 h and immediately chased with the vibration isolated television (VIT) camera at 2015 h.

At the seafloor, the VIT camera verified the FFF had landed successfully. The pipe was tripped up and out of the hole from 55.6 mbsf to 516.7 mbrf with the camera observing. The bit cleared the seafloor at 2117 h and seemed to leave the FFF undisturbed.

The VIT was back on deck at 2209 h. The rig crew then reinstalled the UGH and reassembled the rig floor. The pipe trip continued to 145.0 mbrf. The bit cleared the rotary table at 0025 h, and the rig floor was secured. The vessel was switched to bridge control at 0130 h on 2 February. All thrusters were up and secure, with the start of the sea passage to Site U1595 at 0142 h, ending Site U1599 for the time being.

After arrival on 5 February, the crew made up the RCB BHA with the bit used previously. Winds were forecast to rise above 40 kt with gusts over 50 kt, exceeding shallow operations limits. The vessel began waiting on weather with the pipe down, beginning at 0915 h on 6 February. The ship was offset 5.5 nm west in dynamic positioning (DP) mode to deeper water, away from Anafi Island, which was on the leeward side.

At 1840 h on 6 February, in anticipation of the weather coming down, the ship started the DP move back over Hole U1599C. The move was completed at 0100 h on 7 February, and the vessel went back to work following 39.75 h of waiting on weather.

The VIT was deployed. While the camera system was being lowered, the vessel was maneuvered for reentry for about 30 min, reentering Hole U1599C at 0230 h. The VIT was retrieved and back on deck at 0345 h.

The pipe was tripped in to 56.6 mbsf, and the top drive was assembled. A wash barrel was dropped. The trip in with the top drive progressed to 410.0 mbsf, where an obstruction was found. The wash barrel was recovered, a center bit was dropped, and the hole was reamed down to 455.5 mbsf.

At 1300 h on 7 January, RCB coring commenced with Core 26R from 455.5 mbsf and continued to 9 January through Core 50R at 697.8 mbsf, the final depth for Hole U1599C.

The drill string was tripped with the top drive, and the bit cleared the rotary table at 2030 h. The rig floor was secured, with all equipment put away, at 2130 h.

The thrusters were raised and the vessel brought under bridge control at 2134 h. All thrusters were up and secure, and the start of the sea passage to Heraklion at 2142 h marked the end of Site U1599.

All total, Hole U1599C took 4.6 days.

# 3. Lithostratigraphy

Cores from Site U1599 recovered a relatively coherent stratigraphy from 0 to 698.01 mbsf in three holes (Figure F3); however, there was no core recovery in the first cores of Holes U1599A and U1599B. Hole U1599A consists of Sections 2F-1 through 44F-CC (9.7–245.69 mbsf), Hole U1599B consists of Sections 2H-1 through 40F-CC (9.7–241.22 mbsf), and Hole U1599C consists of Sections 2R-1 through 50R-CC (223–697.8 mbsf). Recovery in Hole U1599C began at 223 mbsf using RCB coring with the goal of overlapping the bottoms of Holes U1599A and U1599B to get better recovery.

The recovered material is unlithified sediment in Holes U1599A and U1599B, with mixed volcanic, tuffaceous, and nonvolcanic material in the uppermost ~220 m (Lithostratigraphic Unit I), which transitions to dominantly ooze interspersed with minor volcanic and tuffaceous sediments for the following ~25 m (Unit II). Unit III consists of ~300 m of dolomitic marl with organic-rich–dominated intervals, followed by ~144 m of micrites and calcareous sandstones (Unit IV).
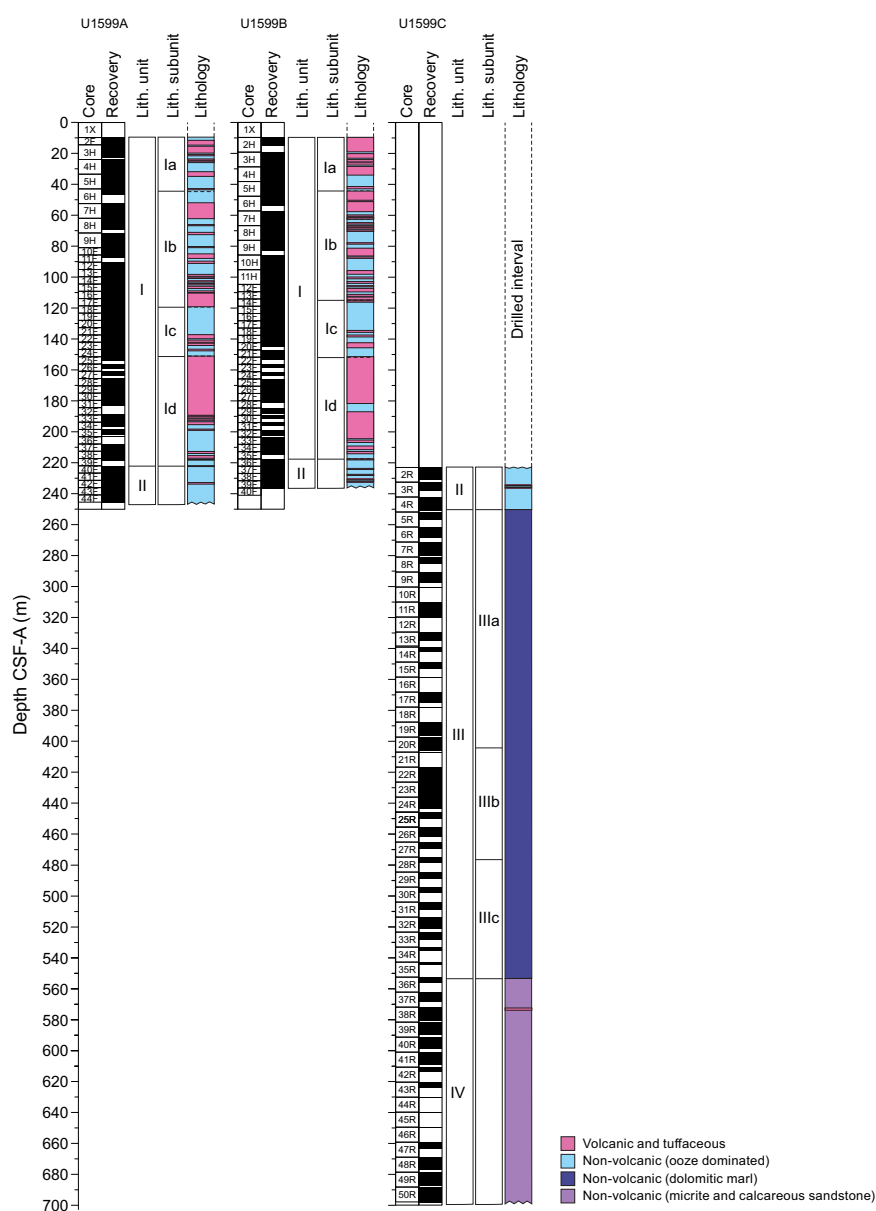


**Figure F3.** Lithostratigraphy, Site U1599. Lithostratigraphic Unit I is divided into four subunits that are further characterized in Figures F4 and F5. Unit color = dominant lithology.

Smear slides for microscopic analyses were prepared to confirm macroscopic descriptions of distinct lithology changes at the section level, such as identification of vitric ash particles in tuffaceous lithologies or crystals in ash layers.

The succession of volcanic layers and tuffaceous or nonvolcanic layers defines four subunits in Unit I (Ia–Id). These subunit distinctions are corroborated by physical property data (i.e., magnetic susceptibility [MS] and natural gamma radiation [NGR]) (see **Physical properties**). Units II and IV do not exhibit sufficient variation to warrant subunits; however, in Unit III a multicore organic-rich lithology allows for designation of Subunits IIIa–IIIc.

X-ray diffraction (XRD) data were obtained from 21 interstitial water (IW) squeeze cake sediment residues from Hole U1599A, 2 from Hole U1599B, and 16 from Hole U1599C. Additionally, two further samples from Hole U1599C were analyzed using XRD.

Figure **F3** summarizes the lithostratigraphy of Site U1599, displaying core recovery and lithostratigraphic units and subunits in Holes U1599A–U1599C. Table **T2** provides the upper and lower boundaries, thicknesses, biostratigraphic ages (see **Biostratigraphy**), and lithologic summaries of the units and subunits. Figure **F4** graphically presents the relative proportions of volcanic, tuffaceous, and nonvolcanic lithologies with lithostratigraphic units and subunits. Figure **F5** presents grain size distributions of the sediments in all units, in particular the changes in grain size within the volcanic- and tuffaceous-dominated units to graphically show the distribution of ash, lapilli-ash, and lapilli in those units. Figure **F6** displays different types of core disturbance observed at Site U1599.

The following sections describe (1) the effects of core disturbance; (2) the four lithostratigraphic units and subunits; (3) correlations between Holes U1599A, U1599B, and U1599C; and (4) XRD results from Site U1599.

## 3.1. Core disturbance

Several types of core disturbance disrupt the lithostratigraphy at Site U1599 (Figure **F6**):

- Uparching: slight to moderate coring-induced shear between the sediment and core liner resulting in bedding uniformly dragged downward along the core margins (Figure **F6A**). In these intervals, original lithofacies and sedimentary structures are usually slightly to severely disturbed but can still be recognized visually.
- Cracks: slight brecciation in the original lithologies, typically a result of drilling-related brittle rock failure (Figure **F6B**).

**Table T2.** Lithostratigraphic units and subunits, Site U1599. * = bottom depth of Subunit Ic is greater than top depth of Subunit Id due to core expansion. ** = bottom not recovered or end of hole. **Download table in CSV format.**

| Lith. unit | Subunit | Top depth (mbsf) | Top hole, core, section, interval (cm) | Bottom depth (mbsf) | Bottom hole, core, section, interval (cm) | Thickness (m) | Lithologic summary |
|---|---|---|---|---|---|---|---|
| | | | 398- | | 398- | | |
| I | Ia | 9.70 | U1599A-2F-1, 0 | 45.13 | U1599A-6H-2, 73 | 35.43 | Ooze and organic-rich ooze dominated with intermixed ash, lapilli-ash, and tuffaceous ooze |
| | | 9.70 | U1599B-2H-1, 0 | 42.61 | U1599B-5H-3, 140 | 32.91 | |
| | Ib | 45.13 | U1599A-6H-3, 0 | 119.52 | U1599A-18F-1, 102 | 74.39 | Mixed intervals of ash, ooze, organic-rich ooze, and ooze with dispersed ash pods, with one large lapilli and lapilli-ash interval; ash intervals are typically dark colored |
| | | 42.61 | U1599B-5H-3, 140 | 116.63 | U1599B-14F-2, 116 | 74.02 | |
| | Ic | 119.52 | U1599A-18F-1, 102 | 151.58* | U1599A-24F-CC, 17 | 32.06 | Ooze and organic-rich ooze dominated with lesser volcanic and tuffaceous intervals |
| | | 116.63 | U1599B-14F-2, 116 | 151.68 | U1599B-21F-4, 75 | 35.05 | |
| | Id | 151.40* | U1599A-24F-CC, 17 | 222.31 | U1599A-40F-1, 41 | 70.91 | Volcanic-dominated with abundant white lapilli, lapilli-ash, and ash intervals; intercalated oozes become more abundant downhole |
| | | 151.70 | U1599B-22F-1, 0 | 217.67 | U1599B-36F-1, 17 | 65.97 | |
| II | | 222.31 | U1599A-40F-1, 41 | 245.66** | U1599A-44F-CC, 22 | 23.35 | Ooze and organic-rich ooze with lesser thin ash and tuffaceous intervals; organic-rich oozes become more abundant downhole |
| | | 217.67 | U1599B-36F-1, 17 | 241.19** | U1599B-40F-CC, 17 | 23.52 | |
| | | 223.00 | U1599C-2R-1, 0 | 251.04 | U1599C-4R-4, 140 | 28.04 | |
| III | IIIa | 247.70 | U1599C-4R-5, 0 | 403.31 | U1599C-20R-6, 48 | 155.61 | Greenish gray to dark greenish gray/dark olive-gray dolomitic marl and organic-rich dolomitic marl |
| | IIIb | 403.31 | U1599C-20R-6, 48 | 476.65 | U1599C-28R-2, 55 | 73.34 | Organic-rich dolomitic marl |
| | IIIc | 476.65 | U1599C-28R-2, 55 | 552.82 | U1599C-36R-1, 32 | 76.17 | Gray to dark gray dolomitic marl and organic-rich dolomitic marl |
| IV | | 552.82 | U1599C-36R-1, 32 | 698.01 | U1599C-50R-CC, 10 | 145.19 | Micrite-dominated with interbedded calcareous sandstones |

- Mixed sediment: occurs in water-saturated, granular core sections where grains and clasts flow and mix, producing moderately to severely disturbed, partially overprinted, sedimentary structures and stratigraphy (Figure **F6C**).
- Soupy: typically restricted to water-saturated intervals of unconsolidated ash, overprinting original sedimentary or depositional structures (Figure **F6D**).
- Sediment flowage: produced by high shearing rates between cored sediments and the core liner that typically leave a smear or thin trail of displaced sediment along the outside rim of the core (Figure **F6E**).
- Core voids: up to ~5 cm voids in the original lithologies were observed in a few instances (Figure **F6F**), for example in cores that experienced basal flow-in (Jutzeler et al., 2014), core extension, or low recovery. Original lithofacies and sedimentary structures are fully destroyed in these intervals.
- Fall-in: at the top of cores, granular material from the top of the hole may fall in and accumulate at the bottom until the next core is recovered (Figure **F6G**). In these intervals, original lithofacies and sedimentary structures are usually destroyed.
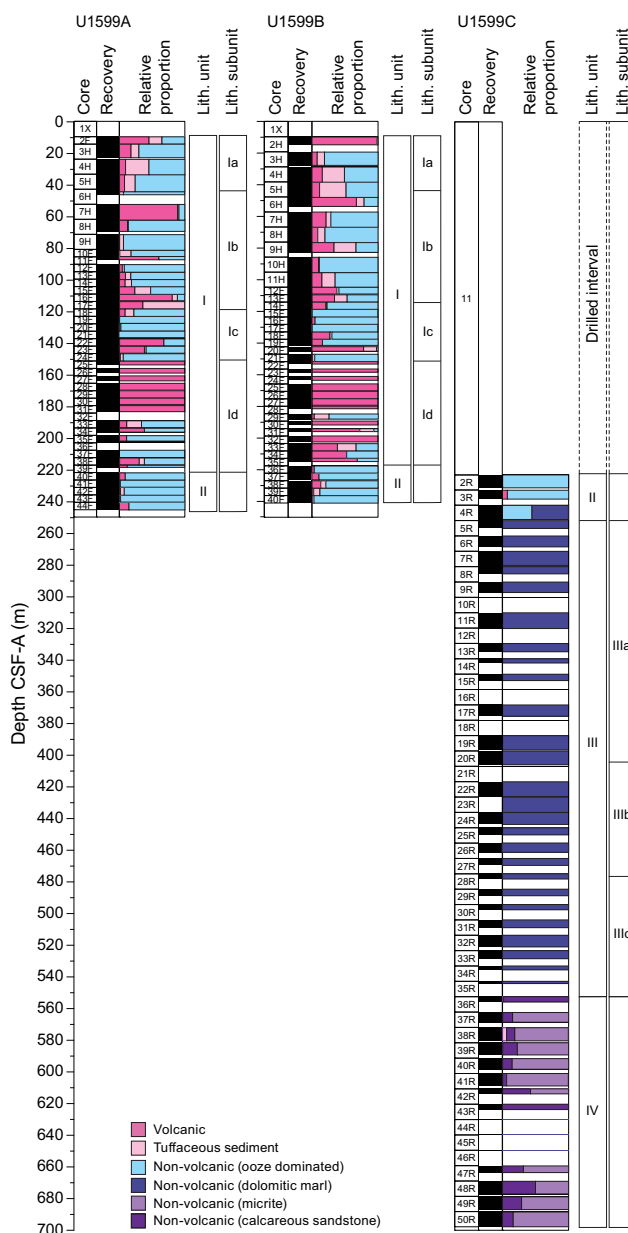


**Figure F4.** Relative percentages of volcanic, tuffaceous, and nonvolcanic lithologies, Site U1599.

- Biscuiting: fractured disc-shaped pieces ranging in size from a few to more than 10 cm thick, often packed with sheared and remolded core material mixed with drill slurry, filling gaps between brittle biscuits (Figure **F6H**). The degree of biscuiting ranges from slight to severe, depending on the size of the biscuits and the proportion of biscuits to infill material.
- Artificial size and density segregation: likely to occur during drilling or with postrecovery core handling processes on board (e.g., inclining, shaking, and plunging cores on the core receiving platform to compact sediments), or while the core is lying flat on deck (Jutzeler et al., 2014). Such core disturbance is observed most often in volcanic sediments because increased porosity allows sucking in of seawater during hydraulic piston coring. The resulting soupy texture allows material to flow within the core liner. Secondary normal or reverse grading, or density separation of clasts, may occur as a result of this disturbance and obscure primary sedimentary features.
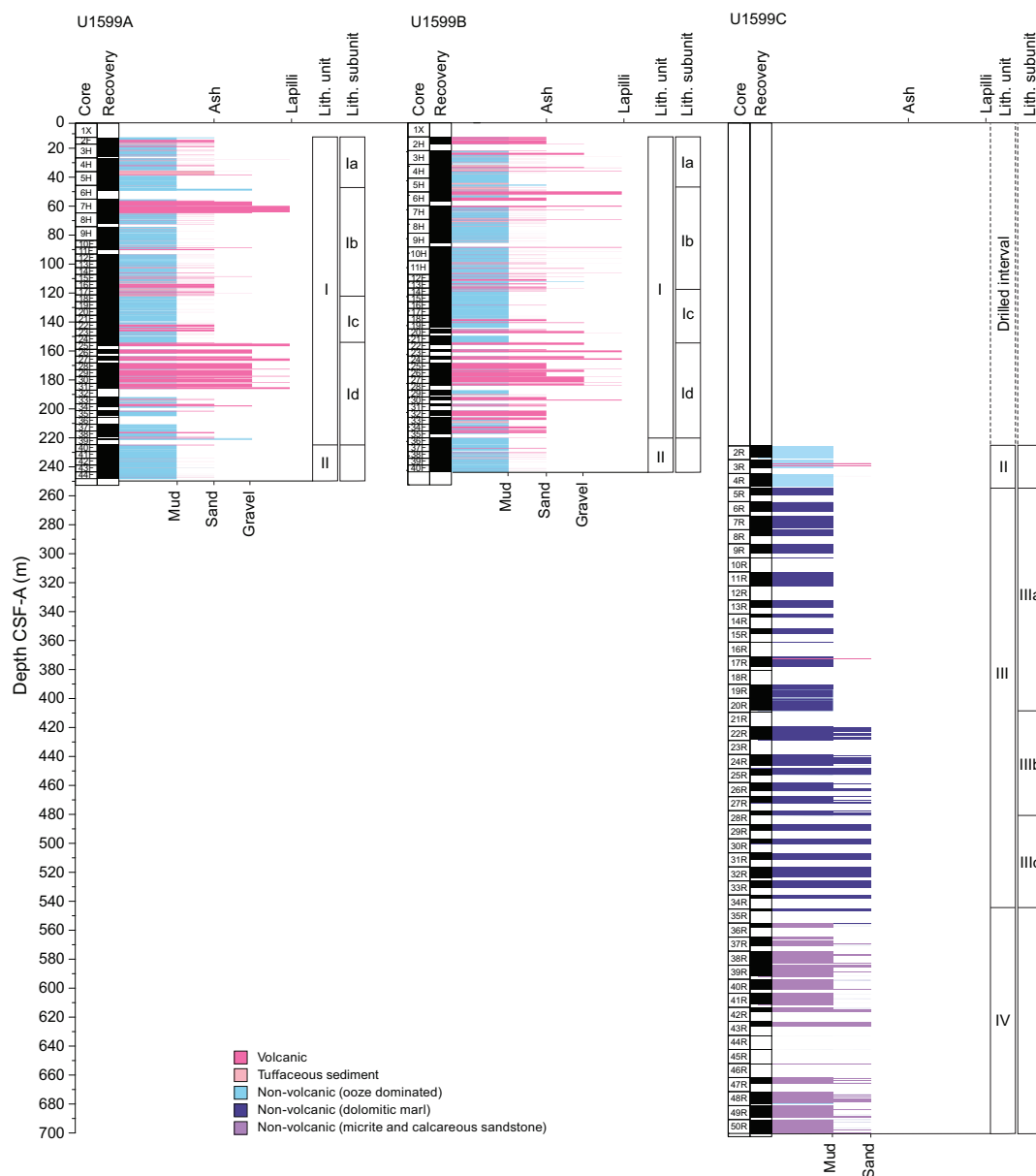


**Figure F5.** Grain size distributions of volcanic, tuffaceous, and nonvolcanic sediments. Length of colored bars = relative grain size (ash = <2 mm; lapilli = 2–64 mm; mud = <63 µm; sand = 0.063–2 mm), with separate scales shown for volcanic grain size (top) and nonvolcanic grain size (bottom; used for tuffaceous and nonvolcanic sediments). Mixed lithologies such as lapilli-ash (dark pink) that have relative grain sizes between two categories are plotted between ticks.

## 3.2. Description of units and subunits

The sediments recovered from Holes U1599A–U1599C comprise four lithostratigraphic units (I–IV) (Figure F3). Unit I is divided into four subunits (Ia–Id), and Unit III is divided into three subunits (IIIa–IIIc) (Figures F3, F4, F5; Table T2). The lithologies of these units and subunits are described below.

### 3.2.1. Unit I

Intervals: 398-U1599A-2F-1, 0 cm, to 40F-1, 41 cm; 398-U1599B-2H-1, 0 cm, to 36F-1, 17 cm
Thicknesses: Hole U1599A = 212.61 m; Hole U1599B = 207.97 m
Depths: Hole U1599A = 9.71–222.31 mbsf; Hole U1599B = 9.7–217.67 mbsf
Age: Holocene to Middle Pleistocene
Lithology: volcanic (ash, lapilli-ash, and lapilli) and tuffaceous sediments with ooze and organic-rich ooze

Unit I extends from 9.7 to 222.31 mbsf in Hole U1599A and 9.7 to 217.67 mbsf in Hole U1599B (Table T2). There was no recovery in the first core of either of these holes. Unit I consists of ooze and organic-rich ooze intercalated with volcanic sediments in the uppermost 45 m (Subunit Ia) followed by a lapilli-dominated sequence that transitions to mixed intervals of ash, ooze, organic-rich ooze, and ooze with dispersed ash pods in the next 74 m (Subunit Ib); 33 m of organic-rich ooze with lesser volcanic and tuffaceous intervals (Subunit Ic); and finally a volcanic-dominated succession of white lapilli, lapilli-ash, and ash intervals with lesser ooze intervals for the final ~70 m (Subunit Id) (Figures F3, F4, F5). Volcanic intervals commonly have sharp bottom contacts with
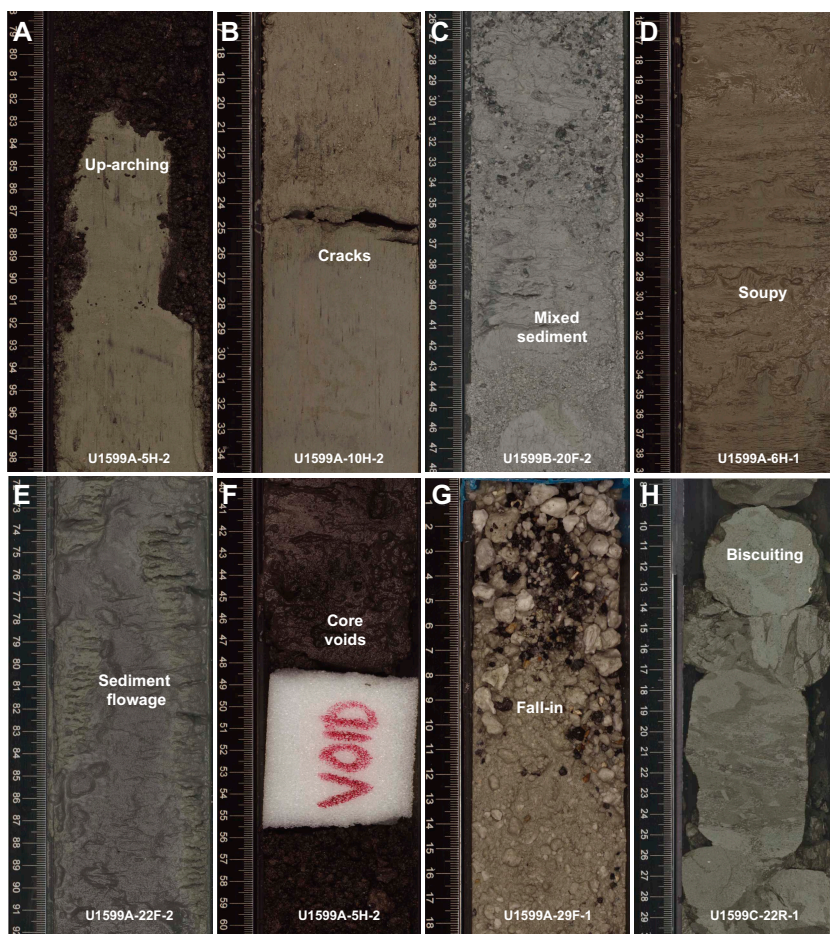


**Figure F6.** Core disturbances, Site U1599. A. Uparching. B. Crack. C. Mixed sediments. D. Soupy. E. Sediment flowage. F. Core voids. G. Fall-in. H. Biscuiting.

tuffaceous or nonvolcanic lithologies. Figure **F7** highlights core images of the most common lithologies collected from each of the subunits from Unit I. Figure **F8** shows representative smear slides from these lithologies.

Volcanic lithologies (>75% volcanic particles; glass shards, pumice, and crystals) comprise ash, lapilli-ash, and lapilli, based on the relative abundance of ash-sized (<2 mm) and lapilli-sized (2–64 mm) particles, as described in **Lithostratigraphy** in the Expedition 398 methods chapter (Kutterolf et al., 2024a), with ash and lapilli used when the proportion of one size was >75% abundance and lapilli-ash used when both sizes were present but at <75% abundance (Fisher and Schmincke, 1984).

Macroscopically, ash layers in Unit I are typically gray and well sorted, range in grain size from fine to coarse ash, and are variably admixed with nonvolcanic sediment at the upper contact. Thicknesses of volcanic intervals in Unit I are highly variable, from centimeter scale to meter scale (e.g., a 12 cm thick ash layer in Section 398-U1599A-13F-1 as compared to an 870 cm thick lapilli-ash/lapilli interval in Subunit Ib). They are frequently characterized by a sharp base and a more diffuse and often bioturbated upper boundary that grades into tuffaceous sediments or ooze. Microscopic observations of smear slides were useful for identification of vitric ash particles in tuffaceous sediments and for specific minerals, especially biotite.

Lapilli and lapilli-ash layers are typically dark gray to dark brownish gray or white and range from a few centimeters to several meters thick. They are often truncated at the lower boundary by loss of recovery, so recovered contacts with underlying material are rare. Where recovered, bottom contacts of these coarser units are sharp or bioturbated and commonly affected by uparching drilling disturbance.

Subunits were defined by the relative proportion of volcanic/tuffaceous intervals and nonvolcanic intervals, as well as by grain size:

- Subunit Ia (Sections 398-U1599A-2F-1, 0 cm, through 6H-2, 73 cm [9.7–45.13 mbsf], and 398-U1599B-2H-1, 0 cm, through 5H-3, 140 cm [9.7–42.61 mbsf]): ooze and organic-rich ooze dominated with intermixed ash, lapilli-ash, and tuffaceous ooze.
- Subunit Ib (Sections 398-U1599A-6H-3, 0 cm, through 18F-1, 102 cm [45.13–119.52 mbsf], and 398-U1599B-5H-3, 140 cm, through 14F-2, 116 cm [42.61–116.63 mbsf]): mixed intervals of ash, ooze, organic-rich ooze, and ooze with dispersed ash pods, with one large lapilli and lapilli-ash sequence. Ash intervals are typically dark colored.
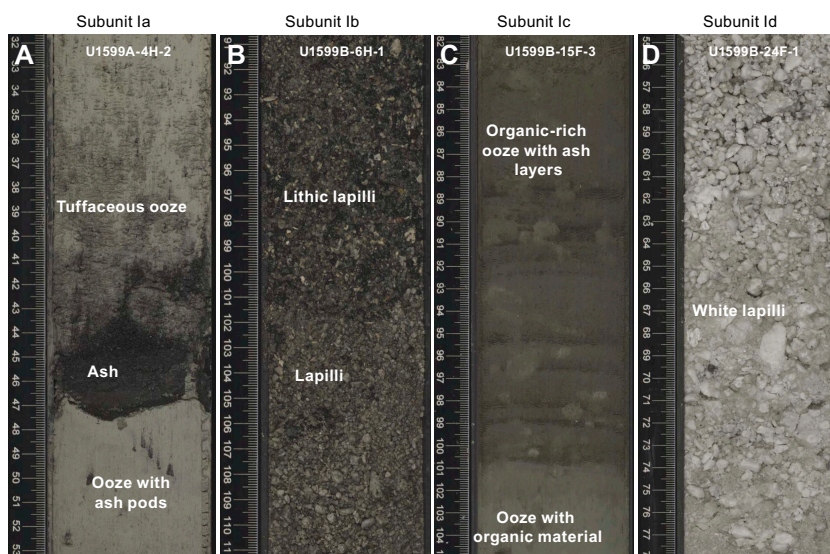


**Figure F7.** Common lithologies from Unit I, Site U1599. A. Tuffaceous ooze with underlying 2 cm thick fine ash and ooze with ash pods. B. Lithic lapilli and lapilli. C. Organic-rich ooze with ash layers overlying ooze with organic material. D. Beautiful white lapilli.

- Subunit Ic (Sections 398-U1599A-18F-1, 102 cm, through 24F-CC, 17 cm [119.52–151.58 mbsf], and 398-U1599B-14F-2, 116 cm, through 21F-4, 75 cm [116.63–151.68 mbsf]): ooze and organic-rich ooze dominated with lesser volcanic and tuffaceous intervals. (Note: The depth in meters below seafloor for the bottom of Subunit Ic is deeper than the top of Subunit Id because of core expansion.)
- Subunit Id (Sections 398-U1599A-24F-CC, 17 cm, through 40F-1, 41 cm [151.4–222.31 mbsf], and 398-U1599B-22F-1, 0 cm, through 36F-1, 17 cm [151.7–217.67 mbsf]): volcanic dominated with abundant white lapilli, lapilli-ash, and ash intervals. Intercalated oozes become more abundant downhole.

### 3.2.1.1. Subunit Ia

Subunit Ia is 35.43 m thick in Hole U1599A and 32.91 m thick in Hole U1599B. It extends from 9.7 to 45.13 mbsf in Hole U1599A (Sections 2F-1, 0 cm, through 6H-2, 73 cm) and from 9.7 to 42.61 mbsf in Hole U1599B (Sections 2H-1, 0 cm, through 5H-3, 140 cm) (Figures **F3, F4, F5**; Table **T2**). The subunit is dominated by ooze and organic-rich ooze intermixed with ash, lapilli-ash, and tuffaceous ooze. Subunit Ia starts with gray bioclastic gravelly muddy sand that has a slightly uparching but sharp bottom contact to an underlying ooze. Ooze intervals display slight bioturbation and are light greenish gray to greenish gray to gray. This lithology contains ash pods and shell fragments, gastropods, and coral fragments (Figure **F7A**). Intercalated volcanic intervals are mainly well-sorted, dark-colored ash layers with sharp lower contacts and gradational upper contacts (Figure **F7A**). The few lapilli and lapilli-ash layers observed contain pumice and scoria. Only one organic-rich ooze is present in Subunit Ia in Sections 398-U1599A-4H-5 and 4H-6 and 398-U1599B-3H-7. This interval is very dark olive-gray and is characterized by planar thin laminations (<0.3 cm), ash pods, and moderate bioturbation. Tuffaceous lithologies include tuffaceous mud,
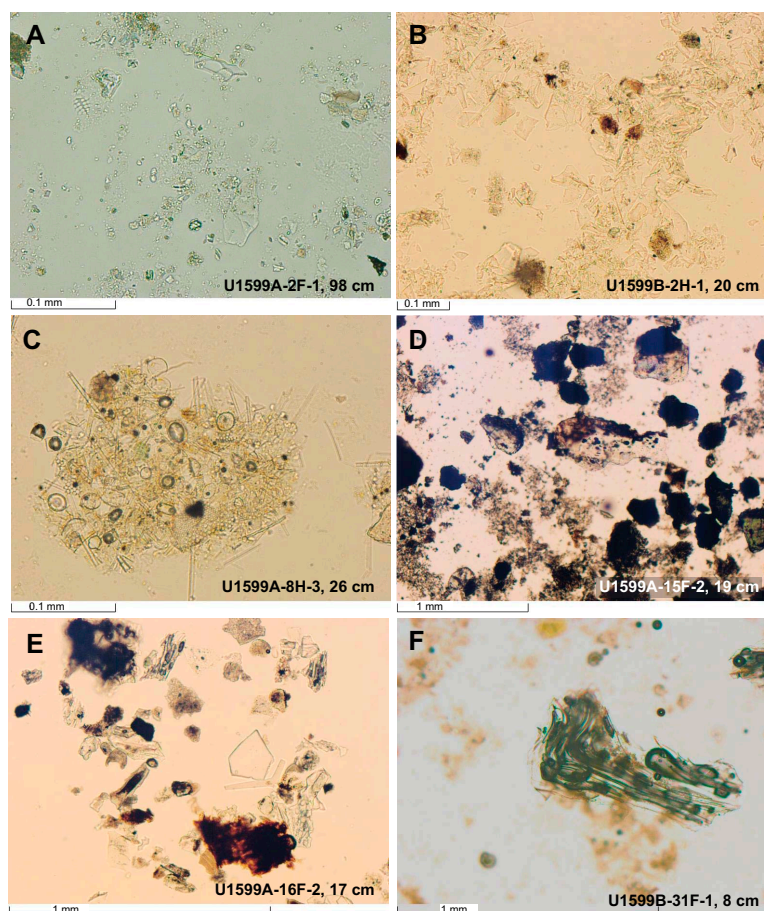


**Figure F8.** Representative lithologies from Unit I, Site U1599. (A) Ooze with ash and (B) ash (Subunit Ia), (C) organic-rich ooze and (D, E) crystal-rich ash (Subunit Ib), and (F) ooze (Subunit Id).

tuffaceous sand, and tuffaceous ooze with grain size varying from mud to pebble. They contain ash pods, pumice lapilli, and lithics; are well sorted; and show a large range in color from greenish gray, dark gray, light olive-gray, gray, grayish brown, and light brownish gray. Subunit Ia ends with a 9.13 m thick interval of well-sorted greenish gray ooze and tuffaceous ooze. This last ooze interval is characterized by low MS and high NGR compared to the beginning of the next subunit (see **Physical properties**).

Selected smear slides of representative lithologies of Subunit Ia are shown in Figure **F8**. A sample of ooze with ash (Figure **F8A**) is characterized by calcareous nannofossils, a variety of microfossils, authigenic calcite, and glass. An ash sample (Figure **F8B**) is dominated by colorless blocky to pumiceous glass shards and minor other components, including sedimentary lithics, crystals (e.g., feldspar), and microfossils.

### 3.2.1.2. Subunit Ib
Subunit Ib is 74.39 m thick in Hole U1599A and 74.02 m thick in Hole U1599B. It extends from 45.13 to 119.52 mbsf in Hole U1599A (Sections 6H-3, 0 cm, through 18F-1, 102 cm) and from 42.61 to 116.63 mbsf in Hole U1599B (Sections 5H-3, 140 cm, through 14F-2, 116 cm) (Figures **F3**, **F4**, **F5**; Table **T2**). This subunit consists of mixed intervals of dark-colored ash, ooze, organic-rich ooze, and ooze with dispersed ash pods.

The subunit begins with a transition from ooze to a gravelly sand with shells in both holes. This interval contains volcanic, metamorphic, sedimentary, and biogenic lithics and is followed by 8.73 m of moderately sorted lapilli and lapilli-ash with grain size ranging from coarse ash to lapilli (Figure **F7B**).

Between 53.26 and 61.99 mbsf, Core 398-U1599A-7H comprises a normal-graded succession from lapilli to lapilli-ash to ash from Sections 7H-1 (top) to 7H-7 (bottom), with nonvolcanic ooze and tuffaceous ooze intervals at the top (Section 7H-1) and bottom (Section 7H-CC) (Figure **F9**). Clasts consist of subrounded gray, white, and banded pumice; black volcanic lithics; and red oxidized volcanic lithics. This normally graded succession of volcanic deposits is not present in Hole U1599B.

Some intraclasts of ooze and shell fragments are also observed within this subunit. The end of this subunit correlates to a sharp decrease in MS (see **Physical properties**).
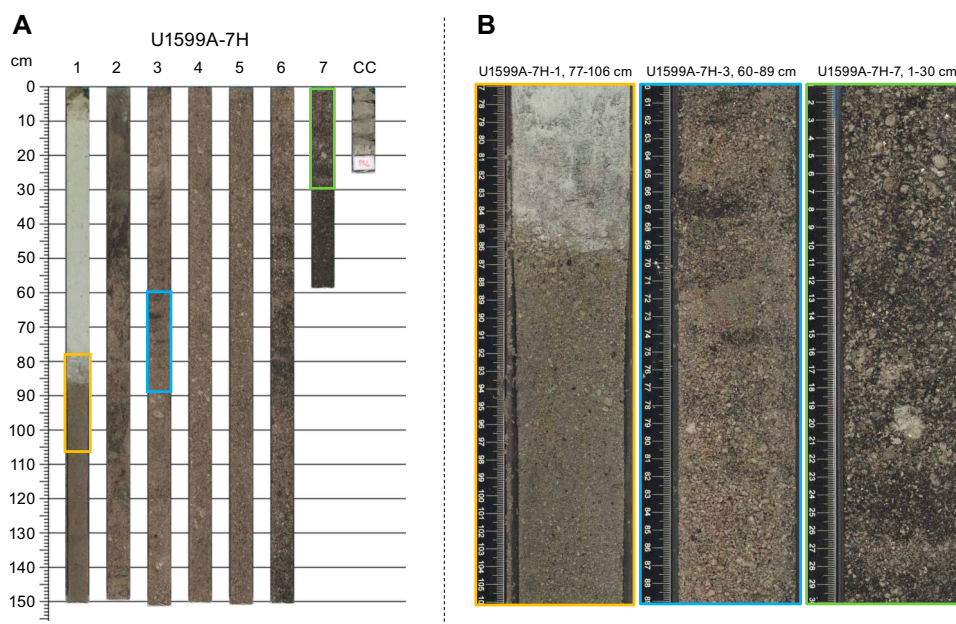


**Figure F9.** A. Normally graded lapilli to lapilli-ash to ash succession extending over several core sections (Subunit Ib), bounded between two ooze intervals (398-U1599A-7H). B. Three core sections showing the grain size change from lapilli at the bottom (7H-7) to lapilli-ash (7H-3) to ash at the top (7H-1).

Selected smear slides of representative lithologies of Subunit Ib are shown in Figure **F8**. A sample of organic-rich ooze (Figure **F8C**) is characterized by its almost entirely biogenic composition and, in this case, predominantly siliceous organisms (e.g., diatoms and radiolarians). This particular sample is a notable exception to the calcareous (nannofossil) oozes generally observed at Site U1599. A crystal ash sample (Figure **F8D**) is dominated by crystals (e.g., feldspar and pyroxene) and volcanic lithics. Some crystals contain melt inclusions. Another crystal ash sample from Subunit Ib (Figure **F8E**) contains a higher proportion of blocky to pumiceous transparent glass as well as a minor amount of biotite and biogenic material.

### 3.2.1.3. Subunit Ic

Subunit Ic is 32.06 m thick in Hole U1599A and 35.05 m thick in Hole U1599B. It extends from 119.52 to 151.58 mbsf in Hole U1599A (Sections 18F-1, 102 cm, through 24F-CC, 17 cm) and from 116.63 to 151.68 mbsf in Hole U1599B (Sections 14F-2, 116 cm, through 21F-4, 75 cm) (Figures **F3**, **F4**, **F5**; Table **T2**). Subunit Ic is marked by a distinctive change in lithology to nonvolcanic and ooze-dominated sediments compared to the previous subunit, corroborated by a sharp decrease in MS and an increase in thermal conductivity (see **Physical properties**). The subunit consists of a package of light greenish gray to olive-gray ooze intercalated with light brownish gray to very dark gray organic-rich (sapropelic) ooze (Figure **F7C**) punctuated by several ash layers. Organic-rich ooze intervals display moderate bioturbation and traces of *Zoophycos*. Thin, dark ash layers are well sorted and are characterized by grain size ranging from fine to coarse ash, sharp lower contacts, and gradational upper contacts. Three ~1 m thick gray soupy volcanic intervals are observed at the bottom of this subunit. In Hole U1599A, these volcanic intervals consist of drilling-disturbed soupy ash (no internal sedimentary structures visible), whereas in Hole U1599B distinct volcanic intervals consist of both ash and lapilli-ash containing subangular white and gray pumice, red oxidized pumice, plagioclase crystals, and shell fragments.

### 3.2.1.4. Subunit Id

Subunit Id is 70.91 m thick in Hole U1599A and 65.97 m thick in Hole U1599B. It extends from 151.4 to 222.31 mbsf in Hole U1599A (Sections 24F-CC, 17 cm, through 40F-1) and 151.7 to 217.67 mbsf in Hole U1599B (Sections 22F-1, 0 cm, through 36F-1, 17 cm) (Figures **F3**, **F4**, **F5**; Table **T2**). It consists of white to gray subangular to subrounded ash, lapilli-ash, and lapilli for the first 30–40 m (Figure **F7D**). These intervals are moderately to poorly sorted and are sometimes normally graded. The remainder of the subunit consists of volcanic intervals (ash, tuffaceous ooze, and lapilli-ash) intermixed with nonvolcanic intervals (ooze and sand). These are generally light gray ashes interlayered with gray to greenish-gray tuffaceous ooze or ooze with ash.

In Hole U1599A, a gravelly interval composed of volcanic and sedimentary lithics and shell fragments is observed at 217.25–218.42 mbsf, and in Hole U1599B, a similar deposit is observed at 191.1–191.67 mbsf.

An exemplary smear slide of ooze with ash is shown in Figure **F8F**. The ooze contains abundant nannofossils with a minor amount of sand-sized blocky and pumiceous volcanic glasses.

### 3.2.2. Unit II

> Intervals: 398-U1599A-40F-1, 41 cm, to 44F-CC, 22 cm (bottom of the hole); 398-U1599B-36F-1, 17 cm, to 40F-CC, 17 cm (bottom of the hole); and 398-U1599C-2R-1, 0 cm, to 4R-4, 140 cm
> Thicknesses: Hole U1599A = 23.35 m; Hole U1599B = 23.52 m; Hole U1599C = 28.04 m
> Depths: Hole U1599A = 222.31–245.66 mbsf; Hole U1599B = 217.67–241.19 mbsf; Hole U1599C = 223–251.04 mbsf
> Age: Middle Pleistocene to Early Pleistocene
> Lithology: ooze and organic-rich ooze with lesser thin ash and tuffaceous intervals; organic-rich oozes become more abundant downhole

Unit II was recovered in all three holes and is the thinnest unit at Site U1599 (ranging 23–28 m). It is composed dominantly of ooze and organic-rich ooze with intermittent ash layers throughout. The subunit begins in Holes U1599A and U1599B below the last thick volcanic interval of Unit I and represents the first appearance of multiple cores of ooze and organic-rich ooze with a few thin

ash layers (Figure **F10**). The top of Unit II was not recovered in Hole U1599C; however, one notable correlation of an ooze interval was established at ~244 mbsf between Holes U1599A, U1599B, and U1599C (see **Correlations between holes**). Oozes generally appear gray to greenish gray and have slight bioturbation; the majority contain ash pods or foraminifera (Figure **F10A**). Volcanic intervals are less abundant in Unit II, but where they do occur, they vary in thickness from a few centimeters up to ~45 cm. They are light gray to dark gray or black and range from fine to coarse ash. Their bottom boundaries are usually sharp, whereas their top boundaries are irregular or gradational (Figure **F10B**). Intervals of organic-rich (sapropelic) ooze occur throughout Unit II, often identified by a gradational change from greenish gray ooze to olive-gray ooze with moderate bioturbation (Figure **F10C**). These organic-rich intervals are generally 20–30 cm thick.

Selected smear slides of representative lithologies of Unit II are shown in Figure **F11**. An ash layer collected in Section 398-U1599A-42F-4, 26 cm, consists of blocky and nonvesicular glass fragments, calcite, pyroxene, feldspar, and opaques (Figure **F11A**). Calcareous tuffaceous sand contains abundant calcite and trace foraminifera, diatoms, radiolaria, pyroxene, and feldspar (Figure **F11B**). A few blocky and nonvesicular glass fragments are also observed.



**Figure F10.** Common lithologies from Unit II, Hole U1599C. A. Ooze with slight bioturbation (*Zoophycos* traces). B. Organic-rich ooze intercalated with a 13 cm thick ash layer. C. Organic-rich ooze.
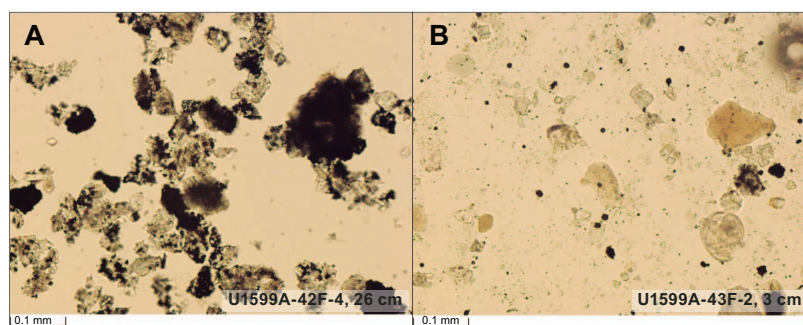


**Figure F11.** Representative lithologies from Unit II, Hole U1599A. A. Ash. B. Calcareous tuffaceous sand.

### 3.2.3. Unit III

Interval: 398-U1599C-4R-5, 0 cm, to 36R-1, 32 cm
Thickness: 305.12 m
Depth: 247.7–552.82 mbsf
Age: Early Pleistocene to Pliocene
Lithology: dolomitic marl and organic-rich dolomitic marl

Unit III extends from 247.7 to 552.82 mbsf in Hole U1599C (Sections 4R-5, 0 cm, through 36R-1, 32 cm) (Figures F3, F4, F5; Table T2). The total thickness of this unit is 305.12 m.

The upper boundary of Unit III is defined by the appearance of dolomitic marl, a consolidated sediment in comparison to the previously unlithified sediments. Dolomitic marl was macro- and microscopically identified in Core 398-U1599C-5R, but XRD results show that it also occurs in Core 4R, thus defining the boundary between Units II and III. Unit III consists of gray to light greenish gray dolomitic marl with periodic intervals of organic-rich dolomitic marl and mudstone. Dolomite was defined macroscopically by its gritty texture and use of 20% HCl, which reacted strongly with the rock compared to 10% HCl. The presence of dolomite throughout this unit was confirmed by XRD (see X-ray diffraction). Disseminated sulfides are present throughout the unit.

Subunits were defined by the relative proportion of organic-rich intervals:

- Subunit IIIa (Sections 398-U1599C-4R-5, 0 cm, through 20R-6, 48 cm; 247.7–403.31 mbsf): greenish gray to dark greenish gray/dark olive-gray dolomitic marl and organic-rich dolomitic marl.
- Subunit IIIb (Sections 398-U1599C-20R-6, 48 cm, through 28R-2, 55 cm; 403.31–476.65 mbsf): organic-rich dolomitic marl.
- Subunit IIIc (Sections 398-U1599C-28R-2, 55 cm, through 36R-1, 32 cm; 476.65–552.82 mbsf): gray to dark gray dolomitic marl and organic-rich dolomitic marl.

#### 3.2.3.1. Subunit IIIa

Subunit IIIa extends from 247.7 to 403.31 mbsf in Hole U1599C (Sections 4R-5, 0 cm, through 20R-6, 48 cm) (Figures F3, F4, F5; Table T2). The subunit consists of greenish gray to light greenish gray dolomitic marl with periodic intervals of organic-rich dolomitic marl and mudstone (Figure F12A). Dolomitic sand intervals are slightly bioturbated, whereas organic-rich intervals are moderately to highly bioturbated and display numerous well-preserved traces of *Chondrites* and
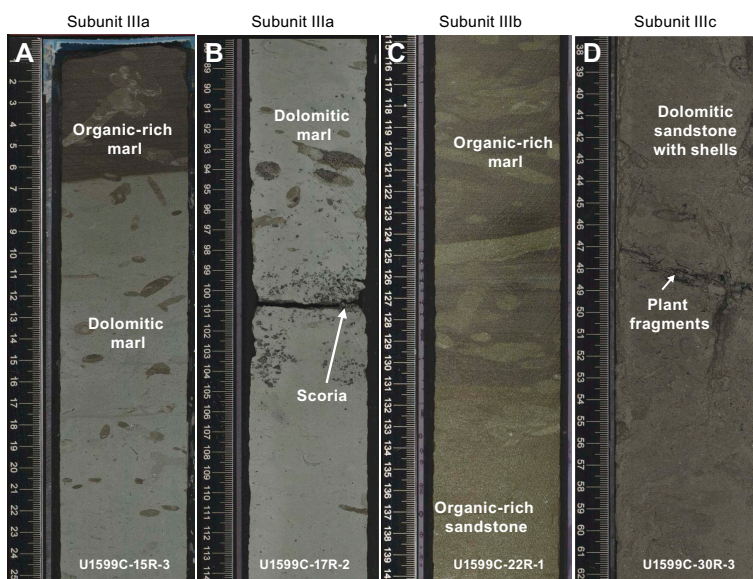


**Figure F12.** Common lithologies from Unit III, Hole U1599C. A. Organic-rich marl overlying dolomitic marl. B. Dolomitic marl with scoria. C. Organic-rich marl and sandstone with moderate bioturbation. D. Dolomitic sandstone with plant fragments.

*Zoophycos* (Figure **F12C**). The organic-rich intervals are commonly thinly laminated (<0.3 cm thick) and display a gradational upper contact and a horizontal sharp lower contact. In the lower part of the subunit (below 329.4 mbsf), the fine-grained and well-sorted lithologies are characterized by the presence of shell fragments.

Three intervals, 333.22–333.37, 341.63–341.69, and 370.70–371.91 mbsf (Sections 398-U1599C-13R-3, 14R-CC, 17R-2, and 17R-3) (Figure **F12B**), contain ash and lapilli. Clasts are angular scoria lapilli, subangular and subrounded pumice, plagioclase, pyroxene, and biotite. In the first two intervals, white pumice with crystals is dominant and gray and banded pumice are present but rare.

An exemplary smear slide of a dolomitic marl of Subunit IIIa is shown in Figure **F13A**. Sample 398-U1599C-5R-4, 83 cm, consists of dolomite, abundant calcareous nannofossils, glaucophane, and sedimentary lithics.

### 3.2.3.2. Subunit IIIb
Subunit IIIb extends from 403.31 to 476.65 mbsf in Hole U1599C (Sections 20R-6, 48 cm, through 28R-2, 55 cm) (Figures **F3**, **F4**, **F5**; Table **T2**). It mainly consists of dark gray organic-rich dolomitic marl and mudstone/sandstone with shells intercalated with thin intervals of gray dolomitic marl with organic material (Figure **F12C**). Subunit IIIb is darker colored than Subunits IIIa and IIIc because of its high organic content. Bioturbation is slight to moderate across the entire subunit with numerous well-preserved traces of *Chondrites* and *Zoophycos* (Figure **F12C**). Organic-rich intervals are commonly thinly laminated (<0.3 cm thick) and display a gradational upper contact and a horizontal sharp lower contact. A few intervals with ash and ash pods are also observed between 456.29 and 475.09 mbsf. Dolomitic marls and their organic-rich equivalents are coarser grained (dolomitic sandstone) in Section 22R-1 (~417 mbsf), and most sections of Core 22R consist of well-sorted dolomitic sands with biogenic clasts, including shell fragments.

An exemplary smear slide of a dolomitic marl with ash of Subunit IIIb is shown in Figure **F13B**. Sample 398-U1599C-26R-1, 98 cm, consists of dolomite, abundant calcareous nannofossils, foraminifera, and brown and altered volcanic glass, as well as pyroxene, mica, and quartz.

### 3.2.3.3. Subunit IIIc
Subunit IIIc extends from 476.65 to 552.82 mbsf in Hole U1599C (Sections 28R-2, 55 cm, through 36R-1, 32 cm) (Figures **F3**, **F4**, **F5**; Table **T2**) and is dominated by dolomitic sandstone with shells and organic-rich dolomitic sandstone with shells. Lithologies are typically greenish gray or gray to
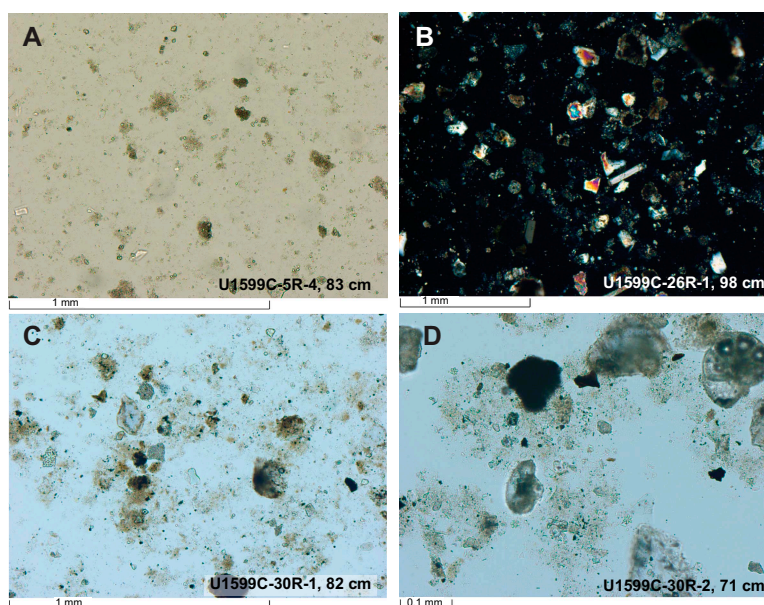


**Figure F13.** Representative smear slides from Unit III, Site U1599. (A) Dolomitic marl (Subunit IIIa), (B) dolomitic marl with ash (Subunit IIIb), and (C) dolomitic sandstone and (D) dolomitic marl (Subunit IIIc).

dark gray, well sorted, and range in grain size from fine sand to pebble. Clasts are mostly made of volcanic rock, sedimentary rock, red oxidized lithics, crystals (quartz and micas), and plant fragments. Quartz and micas are present throughout Subunit IIIc. Slight bioturbation is observed throughout the subunit and consists of burrows infilled by coarser material. The subunit ends in a dolomitic sandy conglomerate with clasts of volcanic rock, sedimentary rock, sandstone, mudstone, quartz, micas, and red oxidized lithics. This interval is moderately to poorly sorted, with grain sizes ranging from coarse sand to pebble.

Selected smear slides of representative lithologies of Subunit IIIc are shown in Figures **F11C** and **F13D**. An organic-rich sand collected in Section 398-U1599C-30R-1, 82 cm, consists of dolomite; rare calcite; abundant calcareous nannofossils; foraminifera; organic material; rare altered glass; sedimentary lithics; and mineral grains of pyroxene, feldspar, and quartz, with minor amounts of opaques and zircon (Figure **F13C**). A dolomitic sand collected in Section 30R-2, 71 cm, is characterized by dolomite; calcite; minor amounts of authigenic pyrite; calcareous nannofossils; foraminifera; and mineral grains of pyroxene, opaques, feldspar, quartz, and sedimentary lithics (Figure **F13D**).

### 3.2.4. Unit IV

Interval: 398-U1599C-36R-1, 32 cm, to 50R-CC, 10 cm (bottom of the hole)
Thickness: 145.19 m
Depth: 552.8–698.01 mbsf
Age: Early to Middle Miocene
Lithology: calcareous mudstone/sandstone, tuff, micrite, and tuffaceous sandstone

Unit IV was only recovered in Hole U1599C and is 144.98 m thick because the hole was terminated before the lower boundary was recovered. The unit begins with calcareous mudstone with interbedded layers of sandstone and a few tuff layers (Figure **F14A**). The unit transitions downward into a micrite-dominated succession with interbedded calcareous sandstone. Some sandstone intervals contain ash and are described as tuffaceous (25%–75% volcanic glass and crystals) or ash-bearing (<25% volcanic glass and crystals). The volcanic glass in these intervals is variably altered and clear.

The calcareous mudstone is dark grayish brown, usually slightly bioturbated, well sorted, and effervesces with 10% HCl. This transitions downward into micrite that alternates from greenish gray to light yellowish brown to light brownish gray and is variably oxidized (Figure **F14B**). The
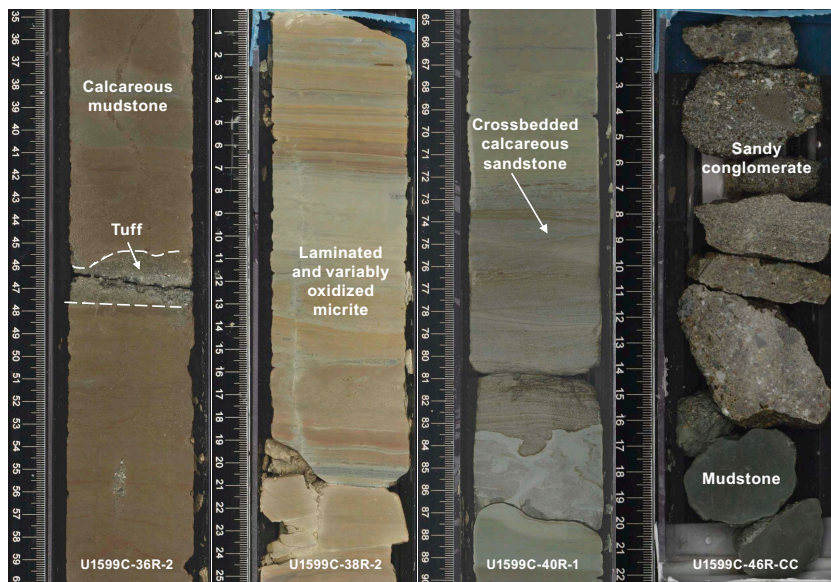


**Figure F14.** Common lithologies from Unit IV, Hole U1599C.

micrite is usually thinly laminated to thinly bedded and is well sorted with limited to no bioturbation. Interbedded calcareous sandstones are observed regularly within the micrite in Cores 398-U1599C-37R through 48R and are cross-bedded in Core 40R (Figure **F14C**). In Core 48R, coarser sedimentary intervals become common, such as calcareous gravelly sandstone and matrix-supported sandy conglomerate (Figure **F14D**). The sandstones are well sorted and sometimes normally graded or bedded. Gravelly sandstone and matrix-supported sandy conglomerate are polymictic poorly sorted greenish gray to very dark greenish gray lithologies with sedimentary, volcanic, and carbonate clasts (>2 mm) and crystals.

The sedimentary rocks become chaotically bedded in Core 398-U1599C-49R, consisting of an irregular and microfaulted mixture of variably colored micrite, dolostone, calcareous sandstone, and sandy conglomerate (sometimes normally graded). Dolostone is nodular and irregular in color, varying between light brown and pinkish gray, and has significantly higher *P*-wave velocity (see **Physical properties**). By the next and final core (50R), however, lithologies return to the more typical micrite with occasional interbedded calcareous sandstone.

An exemplary smear slide of an ash within Unit IV is shown in Figure **F15**. The sample, collected in Section 398-U1599C-36R-3, 36 cm, consists mostly of altered volcanic glass and volcanic minerals including pyroxene, amphibole, feldspar, and biotite, alongside calcite.

## 3.3. Correlations between holes

The recovered sediments from Holes U1599A–U1599C allow for correlation of sediment-specific features such as volcanic layers (e.g., discrete ash or lapilli layers) or organic-rich (sapropelic) horizons. Holes U1599A and U1599B largely overlap in an effort to fill gaps in recovery. Holes U1599A and U1599B extend to 245.66 mbsf and 241.19 mbsf, respectively, and Hole U1599C recovery begins at 223 mbsf; thus, ~22.69 m of overlap was recovered. In the following section, we highlight notable lithologic correlations between cores in Unit I (Figure **F16**) and Unit II (Figure **F17**).

### 3.3.1. Notable correlated deposits

- Lapilli-ash layer with dark gray pumice and scoria, red oxidized lithics, and a sharp lower contact to underlying ooze (Sections 398-U1599A-5H-2, 92 cm [35.82 mbsf], and 398-U1599B-4H-4, 55 cm [33.59 mbsf]) (Figure **F16A**). The uparching observed in the ooze is core disturbance resulting from slight to moderate coring-induced shear between the sediment and core liner.
- Two ash layers intercalated with ooze (Sections 398-U1599A-16F-1, 42–75 cm [~109.6 mbsf], and 398-U1599B-12F-2, 80–117 cm [~107 mbsf]) (Figure **F16B**). In both holes, the first 6 cm thick ash layer displays a sharp lower contact with the uparching disturbance and a gradational upper contact. There is also a color change from dark gray to gray from the bottom to the top. Below this ash layer is a 25 cm thick greenish gray ooze and a 3 cm thick dark gray ash layer.
- Thinly laminated organic-rich ooze interval with a sharp lower boundary. This slightly bioturbated interval is followed by greenish gray ooze (Sections 398-U1599A-19F-2, 30 cm [125 mbsf], and 398-U1599B-15F-3, 101 cm [~122 mbsf]) (Figure **F16C**).
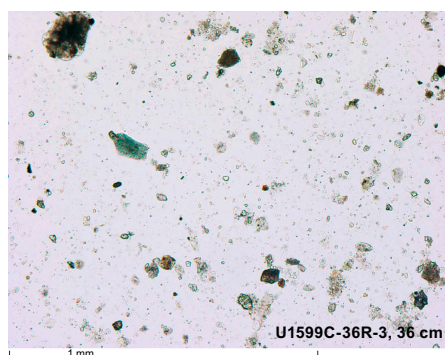


**Figure F15.** Unit IV ash, Hole U1599C.

- ~10 cm thick fine ash layer (Sections 398-U1599A-22F-1, 98 cm [138 mbsf], and 398-U1599B-18F-2, 60 cm [135 mbsf]) (Figure **F16E**). This ash has a relatively sharp lower boundary and a diffuse and gradational upper boundary.
- Ooze and organic-rich ooze interval with a gradation boundary between the two lithologies (Sections 398-U1599A-24F-1, 63–114 cm [~147 mbsf], and 398-U1599B-21F-1, 89–142 cm [~148 mbsf]) (Figure **F16D**). The organic-rich ooze in both holes is highly bioturbated by *Zoophycos* with tunnel-shaped, slightly inclined burrows.
- Dark gray–gray coarse ash observed directly above a greenish gray ooze, marking the boundary between Subunit Id and Unit II (Sections 398-U1599A-40F-1, 41 cm [222 mbsf], and 398-U1599B-36F-1, 17 cm [217 mbsf]) (Figure **F17A**).
- The only correlation across all three holes is an olive-gray organic-rich ooze with a sharp, planar contact to greenish gray ooze in Unit II at 243 mbsf in Hole U1599A, 239 mbsf in Hole U1599B, and 244 mbsf in Hole U1599C (Figure **F17B**).
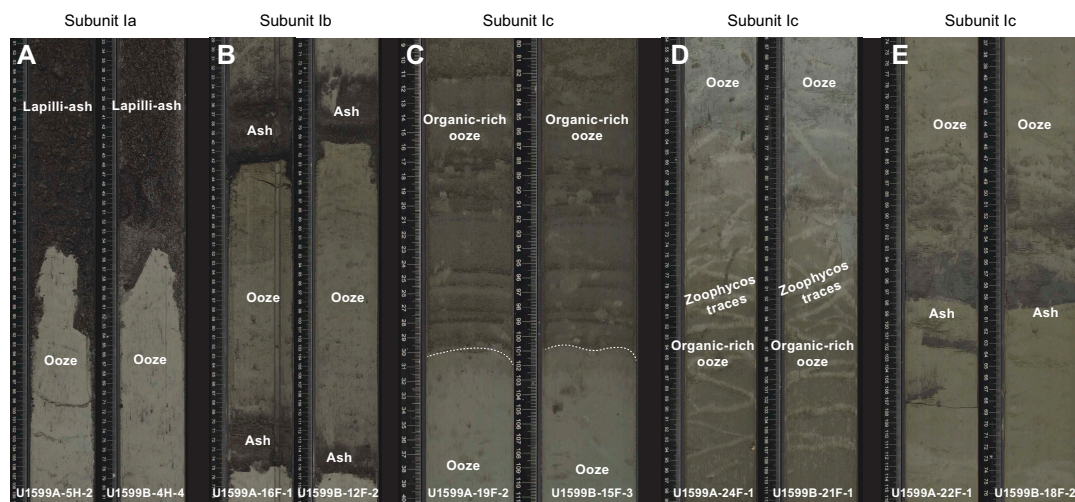


**Figure F16.** Correlations in Unit I between Holes U1599A and U1599B. A. Lapilli-ash layer with a sharp lower contact to underlying ooze. B. Double ash layer. C. Interval of thinly laminated organic-rich ooze with a sharp lower boundary. D. Organic-rich ooze highly bioturbated by *Zoophycos* with tunnel-shaped, slightly inclined burrows. E. ~10 cm thick fine ash layer with a relatively sharp lower boundary and a diffuse and gradational upper boundary.
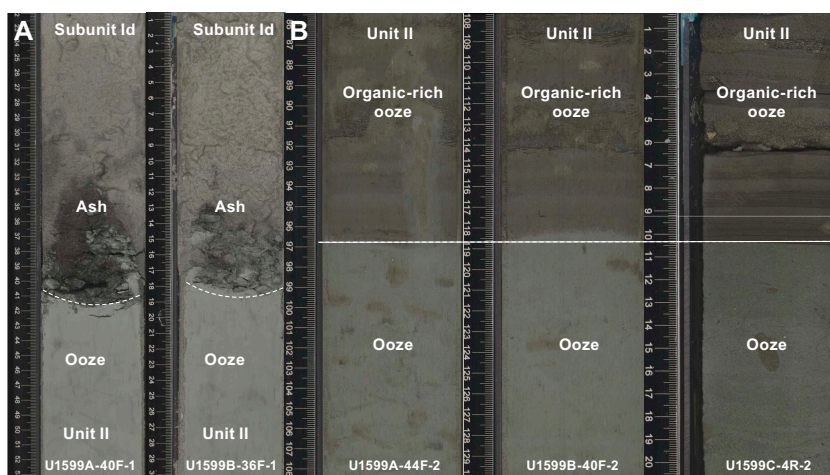


**Figure F17.** Correlations in Unit II and between Holes U1599A, U1599B, and U1599C. A. Dark gray coarse ash directly above greenish gray ooze. B. Sharp boundary between organic-rich ooze and ooze.
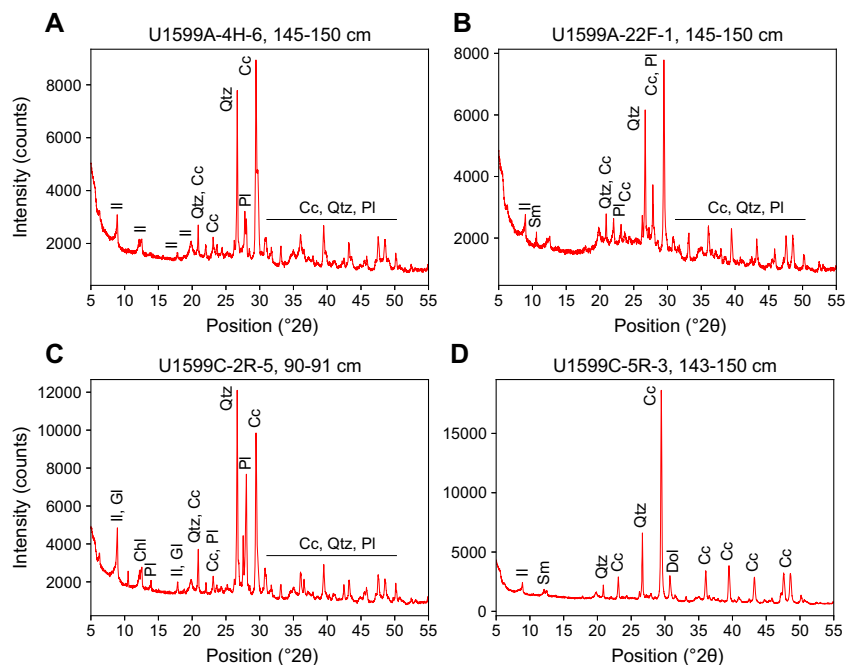
**Figure F18.** XRD spectra of Unit I–III lithologies, Site U1599. A. Ooze (Subunit Ia). B. Tuffaceous ooze (Subunit Ic). C. Calcareous tuffaceous mud (Unit II). D. Dolomitic marl (Unit III). Il = illite, Qtz = quartz, Cc = calcium carbonate (calcite, aragonite), Pl = Ca-rich or Na-rich plagioclase, Sm = smectite (montmorillonite), Gl = glauconite, Chl = chlorite, Dol = dolomite.

## 3.4. X-ray diffraction

XRD data were obtained from 21 IW squeeze cake sediment residues from Hole U1599A, 2 from Hole U1599B, and 15 from Hole U1599C. Additionally, 4 further samples from Hole U1599C were analyzed using XRD.

XRD spectra of representative lithologies from Lithostratigraphic Units I–III are shown in Figure **F18**. These comprise ooze (Figure **F18A**: Section 398-U1599A-4H-6; Subunit Ia), tuffaceous ooze (Figure **F18B**: Section 398-U1599A-22F-1; Subunit Ic), calcareous tuffaceous mud (Figure **F18C**: Section 398-U1599C-2R-5; Unit II), and dolomitic marl (Figure **F18D**: Section 398-U1599C-5R-3; Unit III). Identified minerals in these lithologies include predominantly calcium carbonate (calcite and aragonite) and quartz in addition to clay minerals of the illite and/or smectite groups and occasional glauconite and chlorite. Plagioclase has been identified in some of the lithologies also. Sediments of Unit III (Figure **F18D**) are dolomitic and contain between 9.2% and 32.8% dolomite, based on Rietveld analyses.

## 4. Stratigraphic correlation

Three holes were drilled at Site U1599. Hole U1599A cored to 245.69 mbsf using the APC (9.7–81.35 mbsf) and HLAPC systems (80.9–245.69 mbsf). Hole U1599B was drilled to 241.22 mbsf using the APC (9.7–105.2 mbsf) and HLAPC systems (104.7–241.22 mbsf). Hole U1599C was drilled without recovery to 223.0 mbsf, and rotary core barrel (RCB) coring was performed from 223.0 to 698.01 mbsf.

No correlation during coring was required due to the prevailing challenging drilling condition.

### 4.1. Correlation for establishing CCSF-A depth scale and construction of the splice

To establish the core composite depth below seafloor, Method A (CCSF-A), scale, we analyzed cores from Holes U1599A–U1599C for their physical properties using the Whole-Round Multi-

sensor Logger (WRMSL) for MS and gamma ray attenuation (GRA) density; the Natural Gamma Radiation Logger (NGRL) for NGR intensity; and photos after the cores were split into working and archive halves (see **Physical properties**; also see **Physical properties** in the Expedition 398 methods chapter [Kutterolf et al., 2024a]). The MS data were the most reliable physical parameter for correlations, whereas NGR and GRA density measurements were often overprinted by the irregular distribution of core material in cores with low recovery and high water content.

Because no mudline was preserved, we used Core 398-U1599A-2F as the anchor for stratigraphic correlation. Using this anchor core, we attempted to determine the relative depth offset of each core by establishing affine ties between the holes based on the maximum correlation of all measured physical properties. These depth offsets are reported in Table **T3**. Figure **F19** shows the MS of the three holes on the resulting CCSF-A scale, in which individual cores are shifted according to the identified correlations. This figure highlights the vertical alignment of characteristic events in the adjacent holes.

In general, we were able to identify reliable correlations between most cores of Holes U1599A and U1599B to ~160 mbsf (CCSF-A scale). From there, low recovery, as well as strong lithologic variations and the soupy nature of the recovered material, led to the occurrence of interruptions in the stratigraphic correlation. For each of these interruptions, we used the relative offset between untied (uncorrelated) cores derived from the CSF-A scale to keep the composite depth scale as close to the original CSF-A scale as possible.

Once we had established the composite depth scale, we spliced selected sequences from Holes U1599A and U1599B and added the additional but sparser parts of Hole U1599C to create the most complete and representative section possible. The end product of this process is reported in Table **T4** and illustrated in Figure **F20**. Until about 211 mbsf (CCSF, Method D [CCSF-D], scale), the splice contains gaps that are smaller than 3 m. From there, larger gaps occur.

Compared to the previous sites, cores from Site U1599 showed more significant expansion. Figure **F21** plots the CSF-A and CCSF-A scales for Holes U1599A and U1599B and shows a linear regression curve calculated for both holes together. The deviation from the dotted line indicates an affine growth factor of approximately 9%. Because Hole U1599C had only a small overlap interval with the other holes and was largely appended, we excluded it for this calculation.

**Table T3.** Affine ties, Site U1599. **Download table in CSV format.**
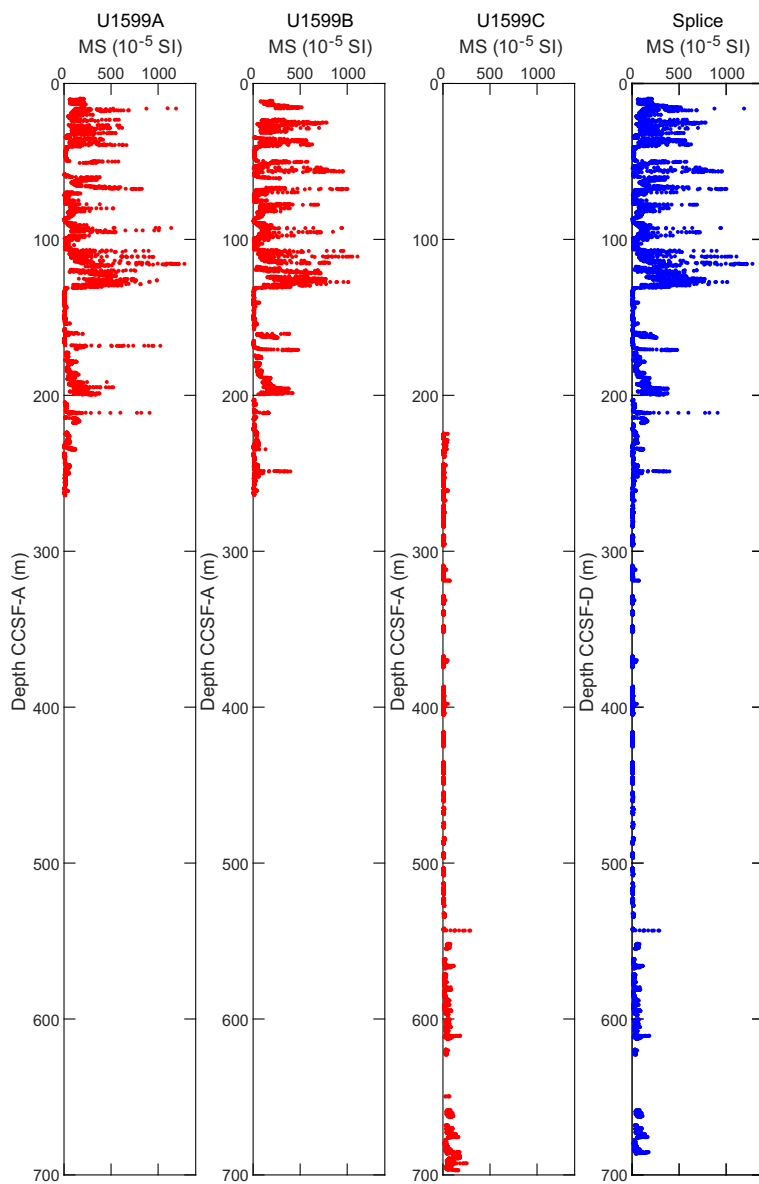
**Figure F19.** WRMSL-derived MS data, Holes U1599A–U1599C. MS data are on the CCSF-A depth scale in the interval where the holes overlap (see also Physical properties).

**Table T4.** Splice ties, Site U1599. **Download table in CSV format.**
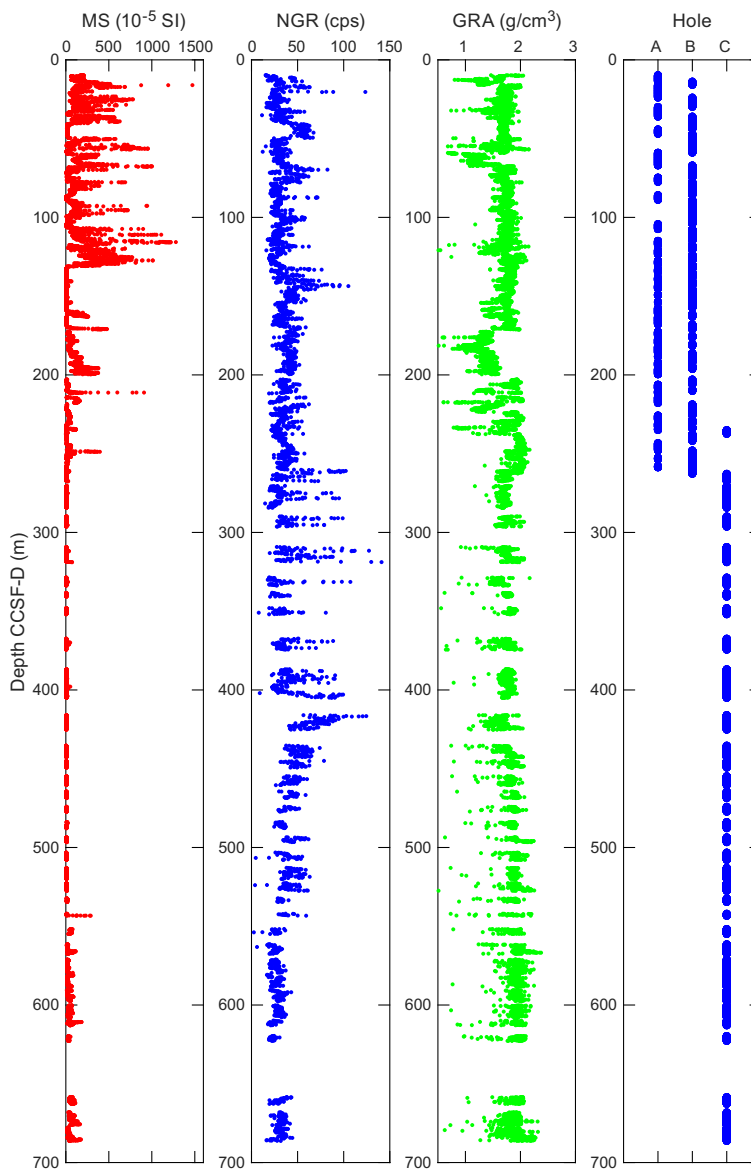
**Figure F20.** Splice, Site U1599. MS, NGR, and GRA density, as well as the respective spliced core interval from Holes U1599A–U1599C, are shown (see also Physical properties). Yellow shading = overlapping depth sections.
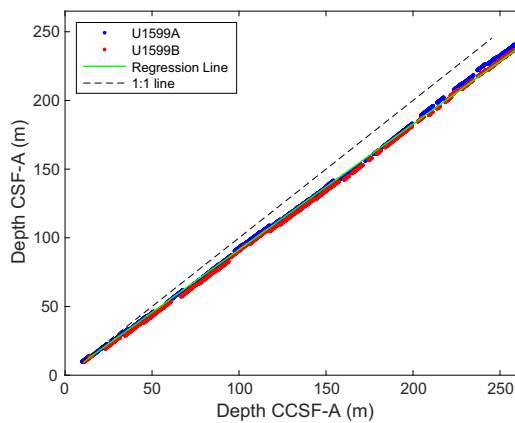


**Figure F21.** CCSF-A versus CSF-A core top depths, Holes U1599A and U1599B. Lines fit through the core top depths of all holes give an estimate of the core expansion. At Site U1599 this is estimated to be approximately 9%.

# 5. Structural geology

Structural geology analyses at Site U1599 included description of cores retrieved from Holes U1599A–U1599C. A total of 625 structures were measured, mostly in relatively consolidated intervals. Observed and measured structures in cores include bedding (73%), faults and deformation bands (20%), mineral veins (1%), and sand dikes (injection; 6%). The distributions and dip angles of planar structures (measured to an estimated accuracy of ±2°) are shown in Figure **F22**. Deformation related to drilling and core recovery was noted but not recorded. Here, we describe and provide examples of each of the features that were recorded.

## 5.1. Bedding

Bedding planes (*n* = 455) were measured mainly on thin sand beds/laminae, sapropels, micrites, and dolomite boundaries. They exhibit horizontal to subhorizontal dips (mean dip = 7.4°; median dip = 5.0°; standard deviation = 7.3°) (Figure **F22A**).

To evaluate the bedding dip variations in the ~700 m deep hole, we divided bedding measurements corresponding to the lithostratigraphic units/subunits defined by core description (see **Lithostratigraphy**) and used a box plot to indicate the distribution of bedding dips (Figure **F23**). Thus, a total of nine bedding measurement units were defined that correspond to the abovementioned lithostratigraphic units/subunits. In the box plot, each box indicates the data distribution range between the twenty-fifth and seventy-fifth percentiles, which is statistically meaningful. Median values (fiftieth percentile of all respective measurements in a unit), which are representative of the data distribution, were used for the evaluation of dip angles. This shows consistent low bedding dips across most units, with slightly steeper dips of ~7° and 11° seen only in Unit IV and Subunit 1d, respectively (Figure **F23**).
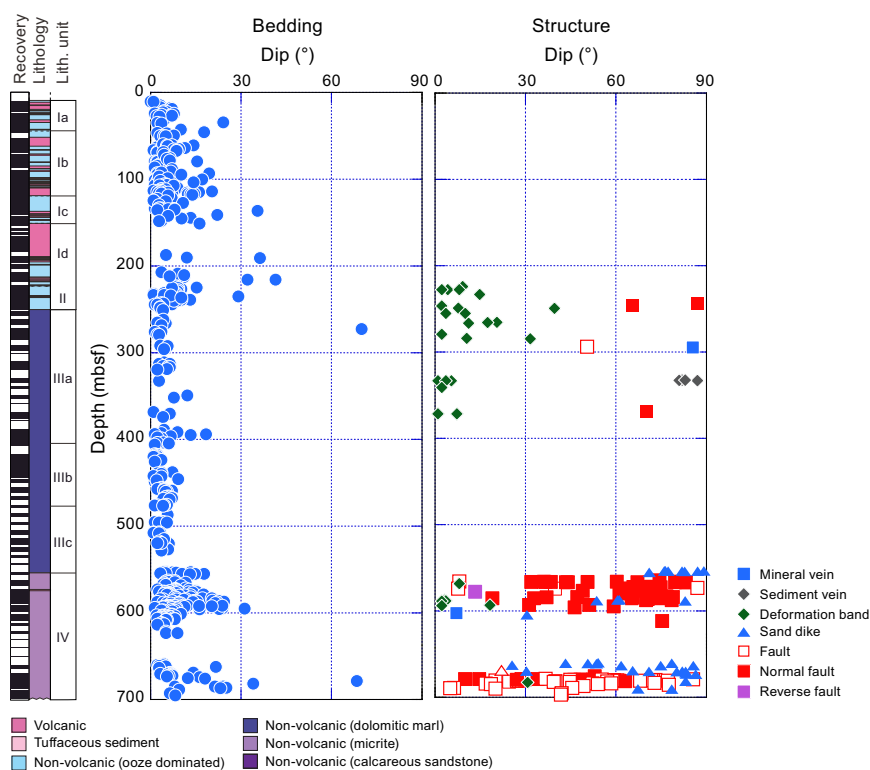


**Figure F22.** Dip data, Site U1599. Lithostratigraphic subunits are described in Lithostratigraphy.

## 5.2. Faults and sand dikes

Small-scale faults and sand dikes are apparent on split core surfaces (Figures **F24**, **F25**). They show apparent displacements from a few millimeters to a centimeter. The sense and/or amount of displacement is defined where they cut bioturbation or sedimentary structures and by asymmetric fabrics within and around the faults. Most faults at Site U1599 have a normal sense of displacement and mostly represent cohesive (healed) fault planes with closed fault planes.
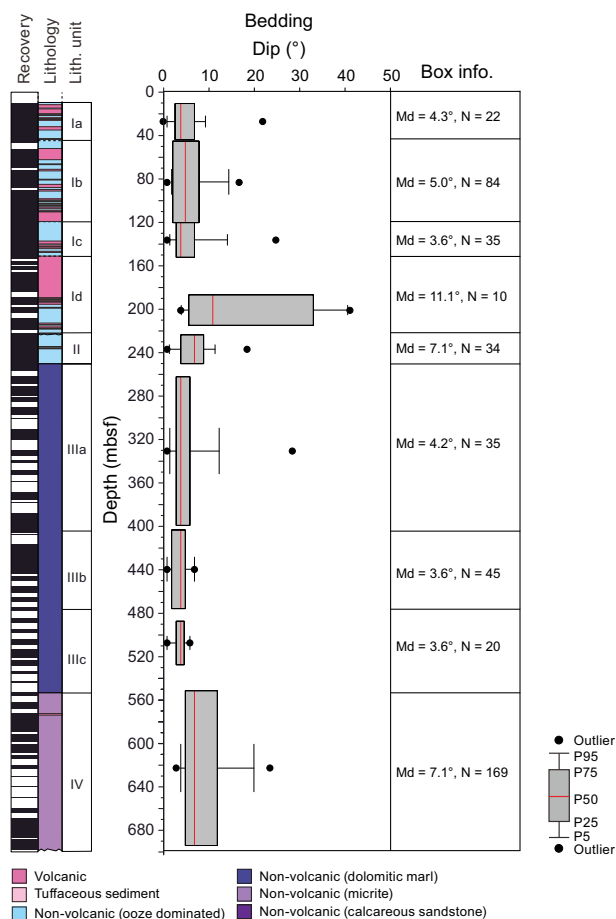


**Figure F23.** Box plots of bedding dip distribution, Site U1599. The minimum (P5), first quartile (P25), median value (P50), third quartile (P75), and maximum (P95) are shown. Only the first outlier smaller than P5 and larger than P95 is plotted as a dot. Md = median dip. N = number of samples. P = percentile. Lithostratigraphic subunits are described in Lithostratigraphy.
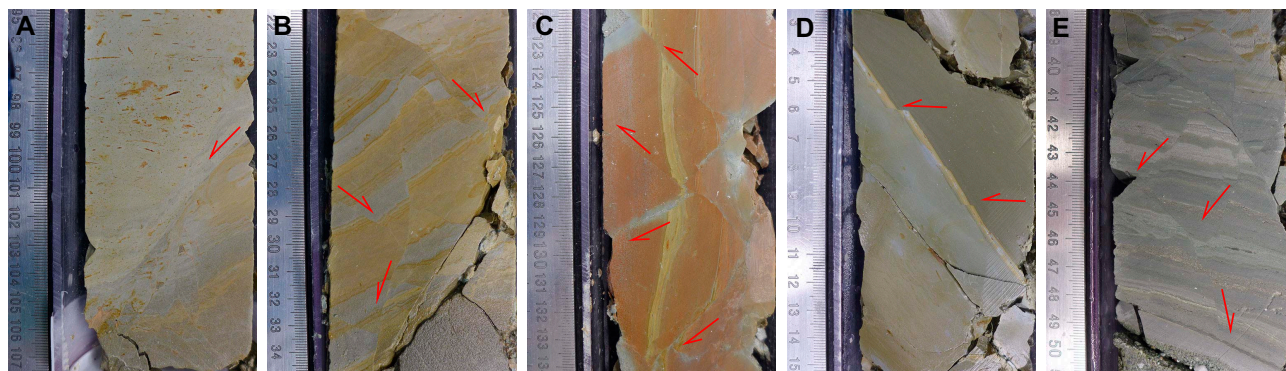


**Figure F24.** Normal faults, Hole U1599C. Arrows = fault positions and sense of shear direction. A. Normal fault (37R-4, 95–107 cm). B–E. Conjugate normal fault system (B: 37R-5, 21–35 cm; C: 49R-1, 122–134 cm; D: 49R-4, 2–15 cm; E: 49R-5, 38–51 cm).

Sand dikes are abundantly developed below Core 398-U1599C-36R. Inside, the dikes are composed of medium–coarse sand grains, and the width of each dike ranges 0.5–10 mm. Dikes are divided into two types: (1) those representing pure tensile fractures (Figure **F25A, F25B**) and (2) those displaying a hybrid-failure mode with shear and extension along them (Figure **F25C, F25D**). Tensile fracture dikes have no significant preferred orientation; they commonly wind through the rocks with orientations varying within 2–10 cm intervals. Therefore, their orientation was apparently random. In contrast, the hybrid-failure dikes show relatively sharper straight planes with a few centimeters offset and a normal sense of displacement.

Almost randomly oriented sand dikes that represent pure tensile-fracture mode form by hydrofracturing, apparently associated with earthquake-induced liquefaction. Generally, hydrofracturing occurred under small differential stress $\Delta\sigma$ (= $\sigma_1 - \sigma_3$) < 4T (Sibson, 1981), where T denotes tensile strength of rocks. However, given their random orientation, these formed under much smaller differential stress. On the other hand, the dikes that represent hybrid-failure mode formed under the stress state 4T < $\Delta\sigma$ < 5.5T (Sibson, 1981).

A dense population of faults was identified in the interval between Sections 398-U1599C-37R-4 and 40R-4 (566–595 mbsf) and below 49R-1 (678 mbsf). These intervals correspond to the core depth where sand dikes are abundantly developed between Sections 36R-2 (554 mbsf) and 41R-3 (554–605 mbsf) and below Section 47R-2 (660 mbsf). This implies that the decrease in effective stress associated with the sand liquefaction may have led to the formation of a large number of normal faults.

## 5.3. Sediment-filled veins and mineral veins

Sediment-filled veins were identified in specific intervals in the middle part of Lithostratigraphic Subunit IIIa. They are recognized as parallel sets or arrays of sigmoidal or curviplanar seams generally <1 mm wide from 332.8 to 333.5 mbsf (Section 398-U1599C-13R-3) (Figures **F22, F26**). The typical thickness of these vein arrays ranges 5–10 cm.

Mud-filled veins are classified as vein structures and are common in sediments at subduction zones (accretionary prism, slope, and forearc basins; Hanamura and Ogawa, 1993; Maltman et al., 1993). They were also identified in cores retrieved by ocean drilling including Nankai, Costa Rica, and Oregon and also in shallowly buried accretionary prism/slope sediments exposed on land in the Miura/Boso Peninsulas, Japan, and the Monterey Formation (USA) (Hanamura and Ogawa, 1993; Maltman et al., 1993; Shipboard Scientific Party, 2001; Expedition 334 Scientists, 2012). Field and experimental studies have shown that these structures are caused by shaking of sediments during earthquakes (Hanamura and Ogawa, 1993; Brothers et al., 1996).
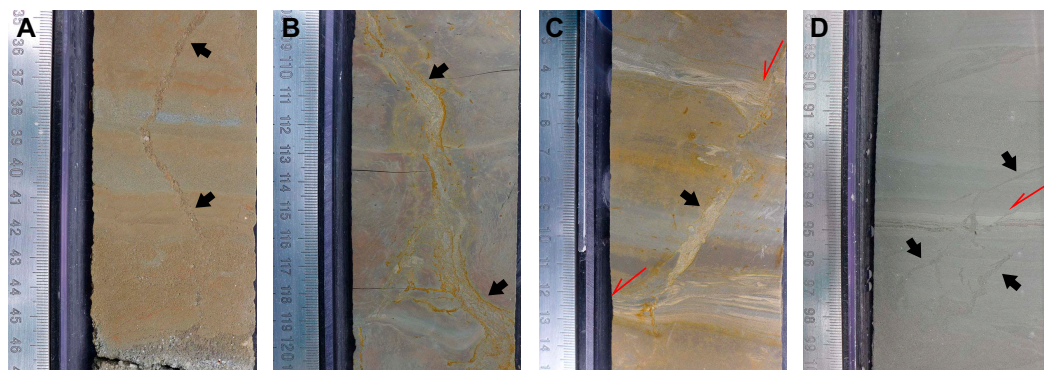


**Figure F25.** Sand dikes, Hole U1599C (black arrows). A, B. Sand dikes representing pure-tensile fracture (A: 36R-2, 35–47 cm; B: 39R-6, 108–121 cm). Note continuous layer boundaries on both sides of the dikes representing no sheared fractures. C, D. Sand dikes representing a hybrid-failure mode of shear and extension (C: 39R-6, 2–15 cm; D: 41R-3, 88–100 cm). Note small amount of displacement along the dikes indicating normal fault sense of shear. Split arrows = fault positions and sense of shear direction.
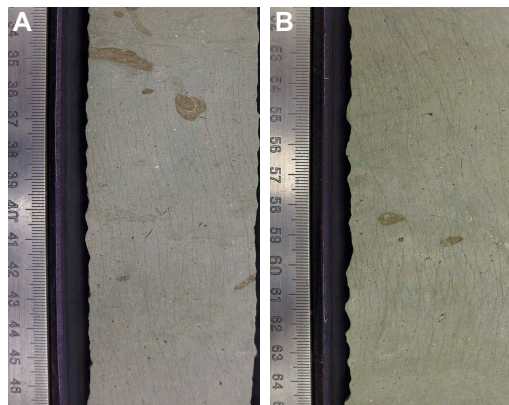
**Figure F26.** Sediment-filled veins, Hole U1599C. A, B. Typical occurrence of mud-filled vein structure (A: 13R-3, 33–47 cm; B: 13R-3, 51–65 cm).

# 6. Biostratigraphy

Planktonic and benthic foraminifera and calcareous nannofossils were examined from core catcher samples and additional split core samples from Holes U1599A–U1599C to develop a shipboard biostratigraphic framework for Site U1599. Additionally, planktonic and benthic foraminifera provided data on paleowater depths, downslope reworking, and possible dissolution.

Site U1599 cored the southeastern Anafi Basin sedimentary sequence and recovered a 697.8 m thick Holocene to Miocene sequence composed of volcanogenic sediments, calcareous and tuffaceous oozes, dolomitic marls, and micritic and calcareous sandstones. Calcareous nannofossils and planktonic foraminifera provided good resolution in the Holocene through Upper Pliocene sediments; however, significant reworking within the lower section facilitated the use of first occurrence datums for primary age control. Ages provided by benthic foraminifera were consistent with those of planktonic foraminifera and calcareous nannofossils. Biostratigraphic datums recognized at Site U1599 are given in Tables **T5** and **T6**, and an age-depth plot is shown in Figure **F27**.

Holocene to Middle Pleistocene–aged sediments (0–0.901 Ma) were recovered in Hole U1599A in Samples 2F-CC, 0–5 cm, to 43F-CC, 24–29 cm (14.25–241.06 mbsf). In Hole U1599B, Holocene to Middle Pleistocene–aged sediments (0–0.901 Ma) were recovered in Samples 1H-CC, 20–23 cm, to 43X-CC, 39–41 cm (7.56–386.6 mbsf). Hole U1599C recovered Middle Pleistocene to Early Miocene–aged sediments (~0.901 to ~18.5 Ma) from Samples 2R-CC, 16–19 cm, to 44R-CC, 1–4 cm (231.08–630.14 mbsf).

## 6.1. Calcareous nannofossils

Calcareous nannofossil biostratigraphy in Holes U1599A–U1599C was established through analysis of core catcher samples, with additional split core samples taken to better constrain biostratigraphic events. Nannofossils are rare to abundant in samples from the Pleistocene–Pliocene sequence (Hole U1599A: 14.2–245.69 mbsf; Hole U1599B: 38.39–241.22 mbsf; Hole U1599C: 231.23–630.125 mbsf) and are rare to common in Miocene samples (Hole U1599C: 580.585–630.125 mbsf). Nannofossils are well to poorly preserved throughout the sequence, and there is significant reworking of older material in most of the Pleistocene samples. Ten nannofossil biostratigraphic datum planes and two calcareous nannofossil zones are recognized at Site U1599, representing a discontinuous Pleistocene to Miocene sedimentary sequence (Figure **F28**). Distributions of calcareous nannofossil taxa are shown in Table **T7**, and biostratigraphic datums are given in Table **T5** and the GEODESC data in the Laboratory Information Management System (LIMS) database.

### 6.1.1. Pleistocene

The presence of *Emiliania huxleyi* in Sample 398-U1599A-2F-CC, 0–5 cm (14.225 mbsf), indicates a Holocene to Middle Pleistocene age (≤0.265 Ma) within Zones MNN21a and 21b (CNPL11: Backman et al., 2012; NN21: Martini, 1971; CN15: Okada and Bukry, 1980) of Rio et al. (1990) and Di Stefano and Sturiale (2010). The top occurrence of *Pseudoemiliania lacunosa* (0.467 Ma) defines the Zone MNN20/21a (CNPL10/11, NN19/20, and CN14a/CN14b) boundary. The last consistent appearance of *P. lacunosa* in Holes U1599A and U1599B occurs in Samples 398-U1599A-13F-CC, 0–5 cm, to 14F-CC, 8–10 cm (99.725–104.46 mbsf); 398-U1599B-10H-CC, 22–24 cm; and 11H-CC, 23–25 cm (95.32–105.19 mbsf). The top occurrence of *Gephyrocapsa* sp. 3 (0.61 Ma), situated between the lower part of the Brunhes Chron in Zone MNN19f, is found between Samples 398-U1599A-24F-CC, 15–17 cm, and 26F-CC, 0–2 cm (151.59–158.87 mbsf), and between Samples 398-U1599B-21F-CC, 0–2 cm, and 25F-CC, 0–1 cm (151.69–169.99 mbsf). The top occurrence of *Reticulofenestra asanoi* (0.901 Ma), situated at the top of the Jaramillo Subchron of the Matuyama Chron in Zone MNN19e, is recognized at the boundary between Samples 398-U1599A-42F-CC, 11–21 cm, and 43F-CC, 24–29 cm (236.26–241.035 mbsf); in Sample 398-U1599B-38F-CC, 11–14 cm (231.765–236.535 mbsf); and in Samples 398-U1599C-2R-CC, 16–19 cm, and 3R-CC, 13–15 cm (231.225–238.29 mbsf). The basal occurrence of *R. asanoi* (1.078 Ma), which lies just below the Jaramillo Subchron of the Matuyama Chron (Zone MNN19e), is found between Samples 4R-CC, 22–24 cm, and 5R-CC, 16–18 cm (251.14–256.7 mbsf).

**Table T5.** Calcareous nannofossil events and absolute age, Site U1599. **Download table in CSV format.**

| Calcareous nannofossil event | Age (Ma) | Top core, section, interval (cm) | Bottom core, section, interval (cm) | Top depth CSF-A (m) | Mid-depth CSF-A (m) | Bottom depth CSF-A (m) |
|---|---|---|---|---|---|---|
| | | 398-U1599A- | 398-U1599A- | | | |
| Base *Emiliania huxleyi* | 0.265 | 2F-CC, 0–5 | 3F-CC, 18–22 | 14.25 | 18.62 | 22.99 |
| Top *Pseudoemiliania lacunosa* | 0.467 | 13F-CC, 0–5 | 14F-CC, 8–10 | 99.75 | 102.10 | 104.45 |
| Top *Gephyrocapsa* sp. 3 | 0.61 | 24F-CC, 15–17 | 26F-CC, 0–2 | 151.60 | 155.23 | 158.86 |
| | | 398-U1599B- | 398-U1599B- | | | |
| Top *Pseudoemiliania lacunosa* | 0.467 | 10H-CC, 22–24 | 11H-CC, 23–25 | 95.33 | 100.255 | 105.18 |
| Top *Gephyrocapsa* sp. 3 | 0.61 | 21F-CC, 0–2 | 25F-CC, 0–1 | 151.70 | 160.845 | 169.99 |
| Top *Reticulofenestra asanoi* | 0.901 | 38F-CC, 11–14 | 39F-CC, 17–20 | 231.78 | 234.15 | 236.52 |
| | | 398-U1599C- | 398-U1599C- | | | |
| Top *Reticulofenestra asanoi* | 0.901 | 2R-CC, 16–19 | 3R-CC, 13–15 | 231.24 | 234.76 | 238.28 |
| Base *Retivulofenestra asanoi* | 1.078 | 4R-CC, 9–11 | 5R-CC, 0–2 | 251.15 | 253.92 | 256.69 |
| Top *Gephyrocapsa* spp. large (>5.5 µm) | 1.245 | 8R-CC, 24–27 | 9F-CC, 0–3 | 285.65 | 291.41 | 297.17 |
| Base *Gephyrocapsa* spp. large (>5.5 µm) | 1.617 | 11R-6, 32 | 13R-CC, 4–10 | 317.24 | 325.895 | 334.55 |
| Base *Gephyrocapsa* spp. medium (>4.0 µm) | 1.73 | 15R-CC, 0–2 | 16R-CC, 15–17 | 352.80 | 355.725 | 358.65 |
| Top *Discoaster brouweri* | 1.95 | 17R-CC, 0–2 | 18R-CC, 0–2 | 375.29 | 376.595 | 377.90 |
| Acme Base *Discoaster pentaradiatus* | 2.64 | 31R-CC, 20–22 | 32R-CC, 16–18 | 508.92 | 514.985 | 521.05 |

**Table T6.** Foraminiferal events and absolute age, Site U1599. **Download table in CSV format.**

| Foraminifer event | Age (Ma) | Top hole, core, section, interval (cm) | Bottom hole, core, section, interval (cm) | Top depth CSF-A (m) | Mid-depth CSF-A (m) | Bottom depth CSF-A (m) |
|---|---|---|---|---|---|---|
| | | 398- | 398- | | | |
| Paracme top *Neogloboquadrina* spp. (sin) | 0.51 | U1599A-24F-CC, 15–17 | U1599A-26F-CC, 0–2 | 151.60 | 155.24 | 158.88 |
| Paracme base *Neogloboquadrina* spp. (sin) | 0.91 | U1599C-4R-CC, 9–11 | U1599C-5R-CC, 0–2 | 251.06 | 253.885 | 256.71 |
| Paracme top *Neogloboquadrina* spp. (sin) | 1.21 | U1599C-7R-CC, 16–19 | U1599C-8R-CC, 24–27 | 280.05 | 282.73 | 285.41 |
| Top *Globigerinoides obliquus* s.s. | 1.28 | U1599C-7R-CC, 16–19 | U1599C-8R-CC, 24–27 | 280.05 | 282.73 | 285.41 |
| Paracme base *Neogloboquadrina* spp. (sin) | 1.37 | U1599C-10R-CC, 0–5 | U1599C-11R-6, 31–33 | 300.47 | 308.86 | 317.25 |
| Base common *Hyalinea balthica* | 1.492 | U1599C-11R-CC, 18–20 | U1599C-13R-CC, 4–10 | 319.94 | 327.275 | 334.61 |
| Base common *Neogloboquadrina* spp. (sin) | 1.79 | U1599C-16R-1, 15–17 | U1599C-17R-CC, 0–2 | 358.67 | 366.98 | 375.29 |
| Base common *Globoconella inflata* | 1.99 | U1599C-20R-CC, 8–11 | U1599C-21R-CC, 0–4 | 405.97 | 406.505 | 407.04 |
| Base *Globoconella inflata* | 2.09 | U1599C-25R-CC, 10–15 | U1599C-26R-CC, 9–12 | 450.26 | 455.81 | 461.36 |
| Top common *Globigerinoides obliquus* | 2.54 | U1599C-29R-CC, 13–15 | U1599C-30R-CC, 15–17 | 488.75 | 493.185 | 497.62 |
| Base *Neogloboquadrina atlantica* (sin) | 2.72 | U1599C-34R-CC, 12–15 | U1599C-35R-CC, 0–2 | 535.57 | 539.89 | 544.21 |

Large-form *Gephyrocapsa* spp. (>5.5 µm) that appear between 1.245 and 1.617 Ma (Zones MNN19d, CNPL8, NN19, and CN13b) are present between Samples 389-U1599C-9R-CC, 0–3 cm (297.185 mbsf); 10R-CC, 0–5 cm (300.445 mbsf); and 11R-6, 32 cm (317.24 mbsf). Samples 13R-CC, 4–10 cm; 14R-CC, 10–12 cm; and 15R-CC, 0–2 cm (334.58–352.79 mbsf), are characterized by the occurrence of *Gephyrocapsa oceanica*, *Gephyrocapsa caribbeanica*, and *P. lacunosa* and by the absence of large-form *Gephyrocapsa* spp. This assemblage indicates that the interval between 334.58 and 352.79 mbsf can be assigned to an age between 1.617 and 1.73 Ma. The Gelasian (Early Pleistocene) assemblages found at this site are characterized by the occurrence of discoasters, including marker species of Miocene to Pliocene successions. The last occurrence of *Discoaster brouweri*, which indicates the boundary of Zones MNN18/19a (NN18/19 and CN12d/CN13a), occurs at the boundary of Samples 17R-CC, 0–2 cm, and 18R-CC, 0–2 cm (375.28–377.91 mbsf). The acme base of *Discoaster pentaradiatus*, which characterizes the middle of Zone MNN16b (2.64 Ma), appears between Samples 31R-CC, 20–22 cm (508.91 mbsf), and 32R-CC, 16–18 cm (521.06 mbsf).

### 6.1.2. Miocene

There is a remarkable change in species composition of calcareous nannofossils between Samples 398-U1599C-35R-CC, 0–3 cm (544.2 mbsf), and 37R-CC, 20–22 cm (568.59 mbsf). In contrast to
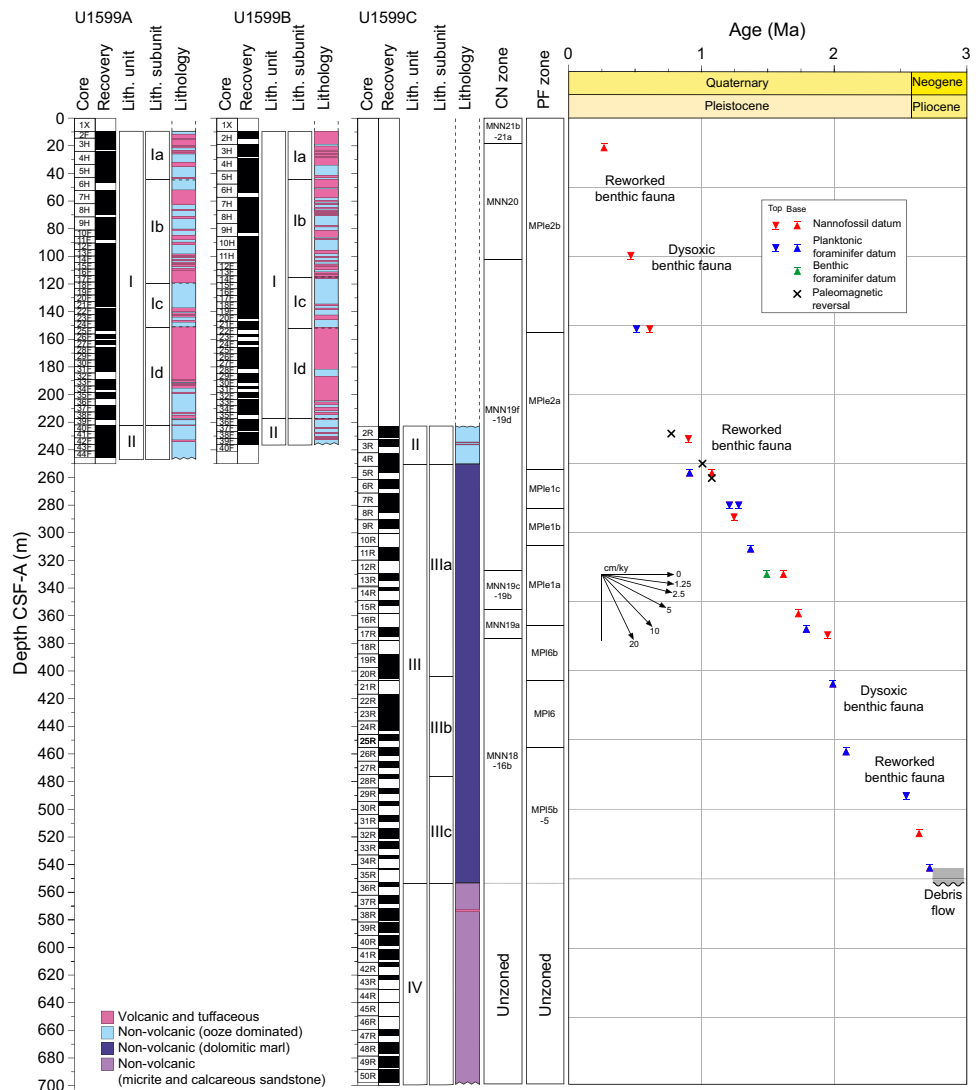


**Figure F27.** Age-depth plot, Holes U1599A–U1599C. Integrated biochronology and magnetostratigraphy are shown. CN = calcareous nannofossil. PF = planktonic foraminifer. Hiatuses are indicated for intervals that correspond to periods of probable sediment remobilization. Biohorizons correspond to those given in Tables T5 and T6.

the previous samples, sediments below Sample 37R-CC, 20–22 cm, contain *Sphenolithus hetero-morphus* and *Sphenolithus belemnos*, *Cyclicargolithus floridanus*, *Discoaster deflandrei*, and *Sphenolithus dissimilis*. These assemblages suggest that the interval between Samples 37R-CC, 20–22 cm (568.59 mbsf), and 44R-CC, 1–4 cm (630.125 mbsf), can be assigned to the Early Miocene.

## 6.2. Foraminifera

Planktonic and benthic foraminifera were examined in core catcher samples and split core samples from Holes U1599A–U1599C (Tables **T8**, **T9**). Absolute ages assigned to biostratigraphic datums follow those listed in Table **T6** in the Expedition 398 methods chapter (Kutterolf et al., 2024a). Planktonic and benthic foraminifer datums for Site U1599 are given in Table **T6**. Planktonic foraminifer abundances and indications of oceanicity (e.g., Hayward et al., 1999) and benthic foraminifer paleowater depth estimations are given in Figures **F29** and **F30**.

Because of the volcanogenic nature of the cored sedimentary sequence, residues (>125 µm) from washed samples were often significantly composed of volcaniclastic particles such as pumice, scoria, and ash that diluted the microfossil component of residues. Foraminifera dominate the biogenic component of residues, however, and age markers are present in sufficient numbers to date most samples reliably. Significant reworking made first occurrence datums most reliable. Additionally, volcanic material, clastic grains, minor pyrite, carbonaceous plant-derived matter, and
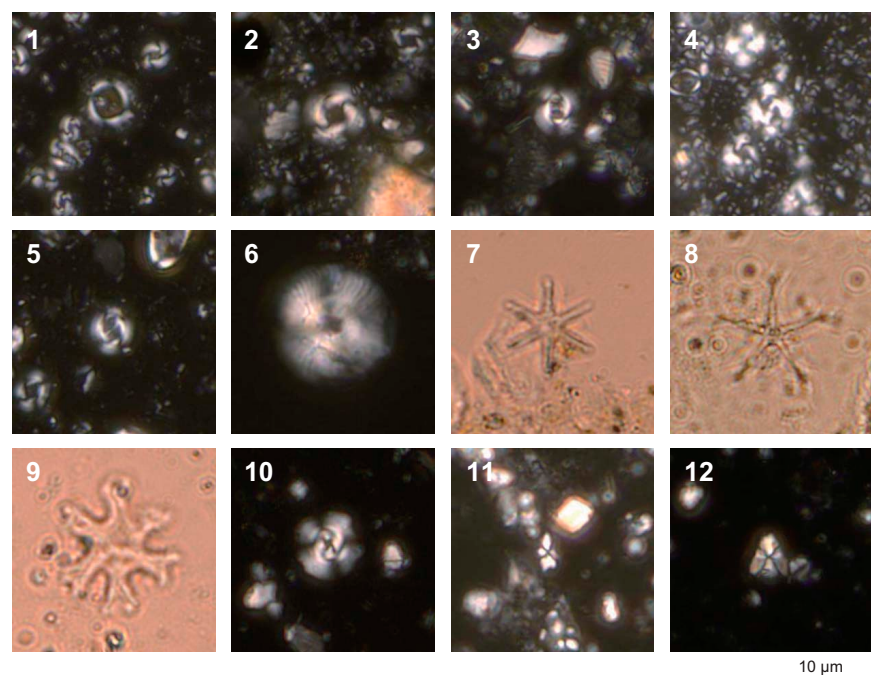


**Figure F28.** Calcareous nannofossils, Holes U1599B (1–2), U1599A (3), and U1599C (4–12). 1. *Pseudoemiliania lacunosa* (Kamptner) Gartner (11H-CC, 23–25 cm). 2. *Reticulofenestra asanoi* Sato and Takayama (39F-CC, 18–21 cm). 3. *Gephyrocapsa* sp. 3 (19F-CC, 19–21 cm). 4, 5. 10R-CC, 0–5 cm: (4) *Gephyrocapsa* spp., large form (>5.5 µm); (5) *Gephyrocapsa oceanica* Kamptner. 6. *Calcidiscus macintyrei* (Bukry and Bramlette) (16R-CC, 15–17 cm). 7. *Discoaster brouweri* Tan Sin Hok (20R-CC, 8–11 cm). 8. *Discoaster pentaradiatus* Tan Sin Hok (27R-CC 10–12 cm). 9, 10. 44R-CC, 10–4 cm: (9) *Discoaster deflandrei* Bramlette and Riedel; (10) *Cyclicargolithus floridanus* (Roth and Hay) Bukry. 11. *Sphenolithus belemnos* Bramlette and Wilcoxon (39R-CC 18–21 cm). 12. *Sphenolithus dissimilis* Bukry and Percival (40R-CC, 12–15 cm).

**Table T7.** Distribution of calcareous nannofossils, Site U1599. **Download table in CSV format.**

**Table T8.** Distribution of planktonic foraminifera, Site U1599. **Download table in CSV format.**

**Table T9.** Distribution of benthic foraminifera, Site U1599. **Download table in CSV format.**

| Core, section, interval (cm) | Bottom depth CSF-A (m) | AW Planktonic (%) | OK Planktonic (%) | Planktonic mean (%) | Oceanicity | Paleowater depth (m) |
|---|---|---|---|---|---|---|
| 398-U1599A- | | | | | | |
| 2F-CC | 14.25 | 45 | 50 | 47.5 | Extra-neritic | |
| 3H-CC | 23.05 | 90 | 90 | 90 | Oceanic | NA |
| 4H-CC | 33.56 | 55 | 45 | 50 | Extra-neritic | |
| 5H-CC | 43.56 | 70 | 95 | 82.5 | Sub-oceanic | |
| 6H-CC | 46.50 | 29 | 27 | 28 | Outer neritic | Reworked benthics |
| 7H-CC | 62.24 | 94 | 43 | 68.5 | Sub-oceanic | NA |
| 9H-CC | 81.35 | 78 | 77 | 77.5 | | |
| 10F-CC | 85.60 | 75 | 66 | 70.5 | | |
| 12F-CC | 95.34 | 37 | 34 | 35.5 | Extra-neritic | Dysoxic benthic fauna |
| 13F-CC | 99.87 | 33 | 38 | 35.5 | | |
| 14F-CC | 104.47 | 96 | 90 | 93 | Oceanic | |
| 15F-CC | 109.27 | 71 | 55 | 63 | Sub-oceanic | |
| 16F-CC | 113.52 | 48 | 51 | 49.5 | Extra-neritic | |
| 17F-CC | 118.80 | 93 | 90 | 91.5 | Oceanic | |
| 18F-CC | 123.40 | 87 | 72 | 79.5 | Sub-oceanic | |
| 19F-CC | 128.17 | 92 | 95 | 93.5 | Oceanic | Upper to mid bathyal (300-800 m) |
| 20F-CC | 132.79 | 81 | 65 | 73 | Sub-oceanic | |
| 21F-CC | 136.76 | 72 | 70 | 71 | | |
| 23F-CC | 146.44 | 60 | 52 | 56 | Extra-neritic | |
| 24F-CC, 1–3 | 151.46 | 46 | 73 | 59.5 | | |
| 24F-CC | 151.60 | 69 | 59 | 64 | Sub-oceanic | |
| 26F-CC | 158.91 | 71 | 54 | 62.5 | | |
| 27F-CC | 163.92 | 34 | 64 | 49 | | |
| 33F-CC | 193.55 | 44 | 31 | 37.5 | | |
| 34F-CC | 196.36 | 52 | 41 | 46.5 | Extra-neritic | |
| 35F-CC | 202.22 | 67 | 40 | 53.5 | | |
| 37F-CC | 212.80 | 40 | 41 | 40.5 | | |
| 38F-CC | 217.08 | 58 | 53 | 55.5 | | |
| 40F-CC | 226.72 | 76 | 77 | 76.5 | Sub-oceanic | Reworked benthics |
| 41F-CC | 231.52 | 43 | 34 | 38.5 | Extra-neritic | |
| 42F-CC | 236.28 | 71 | 67 | 69 | Sub-oceanic | |
| 43F-CC | 241.06 | 40 | 27 | 33.5 | Extra-neritic | |
| 44F-CC | 245.69 | 85 | 90 | 87.5 | Sub-oceanic | |
| 398-U1599B- | | | | | | |
| 2H-CC | 14.89 | | 0 | 0 | Inner neritic | |
| 4H-CC | 38.41 | | 35 | 35 | Extra-neritic | |
| 6H-CC | 53.80 | | BARREN | | | |
| 7H-CC | 66.79 | | 74 | 74 | Sub-oceanic | |
| 8H-CC | 76.49 | | 89 | 89 | | |
| 9H-CC | 82.92 | | 72 | 72 | | |
| 10H-CC | 95.33 | | 62 | 62 | | |
| 11H-CC | 105.20 | | 74 | 74 | | |
| 12F-CC | 109.11 | | 43 | 43 | Extra-neritic | |
| 13F-CC | 114.22 | | 53 | 53 | | |
| 14F-CC | 118.95 | | 81 | 81 | Sub-oceanic | |
| 15F-CC | 123.80 | | 58 | 58 | Extra-neritic | |
| 16F-CC | 128.53 | | 53 | 53 | | |
| 17F-CC | 133.18 | | 86 | 86 | Sub-oceanic | |
| 18F-CC | 137.93 | | 78 | 78 | | NA |
| 19F-CC | 141.57 | | 62 | 62 | | |
| 21F-CC | 151.70 | | 50 | 50 | Extra-neritic | |
| 25F-CC | 170.20 | | 33 | 33 | | |
| 26F-CC | 175.38 | | 26 | 26 | Outer neritic | |
| 27F-CC | 179.29 | | 27 | 27 | | |
| 29F-CC | 188.25 | | 51 | 51 | Extra-neritic | |
| 30F-CC | 191.64 | | 75 | 75 | Sub-oceanic | |
| 31F-CC | 195.96 | | BARREN | | | |
| 33F-CC | 208.05 | | 69 | 69 | Sub-oceanic | |
| 34F-CC | 212.80 | | BARREN | | | |
| 35F-CC | 214.90 | | 45 | 45 | Extra-neritic | |
| 36F-CC | 222.22 | | 78 | 78 | | |
| 37F-CC | 226.47 | | 81 | 81 | Sub-oceanic | |
| 38F-CC | 231.78 | | 82 | 82 | | |
| 39F-CC | 236.55 | | 73 | 73 | | |
| 40F-CC | 241.22 | | 55 | 55 | Extra-neritic | |

**Figure F29.** Foraminiferal oceanicity and paleowater depth estimates, Site U1599. Blue colors show relationship between oceanicity index and paleowater depth. Observers: AW = Adam Woodhouse, OK = Olga Koukousioura. NA = not applicable. (Continued on next page.)

other fossil material, including shells and fragments (Bivalvia and Gastropoda), Pteropoda, Scaphopoda, Bryozoa, Arthropoda (*Balanus*), echinoid spines and plate fragments, radiolarians, and ostracods, as well as fish teeth, are also present in variable amounts in most samples. In addition, reworked Pliocene foraminifera are often present.

Throughout the section, foraminifera with very good to very poor preservation are present in siliciclastic, volcaniclastic, and dolomitic sediments. Foraminifer abundances are also variable, and they are notably rare in tuffaceous oozes, likely due to sedimentary dilution, whereas coarser volcaniclastic intervals are sometimes barren. Notably, foraminifera are very rare or absent from the lowermost micritic and calcareous sandstones.

### 6.2.1. Holocene to Upper Pliocene foraminiferal biostratigraphy

Because of explosive volcanic events and rapid deposition of the upper sedimentary section, the base of the Holocene is not possible to assign accurately. Planktonic foraminifer assemblages from the Holocene–Pleistocene section of Holes U1599A–U1599C are mostly well preserved, where specimens are rarely broken or exhibiting partially dissolved shell walls.

Holocene–Upper Pliocene foraminifer faunas indicate large fluctuations in relative paleowater depth and oceanicity with highly variable planktonic abundances that range 0%–93.5% where foraminifera are present (Figure F30). The fauna are typical of Pliocene–Pleistocene Mediterranean

| Core, section, interval (cm) | Bottom depth CSF-A (m) | AW Planktonic (%) | OK Planktonic (%) | Planktonic mean (%) | Oceanicity | Paleowater depth (m) |
|---|---|---|---|---|---|---|
| 398-U1599C- | | | | | | |
| 2R-CC | 231.08 | 30 | BARREN | 30 | Extra-neritic | NA |
| 3R-CC | 238.17 | 33 | 31 | 32 | Extra-neritic | |
| 4R-CC | 251.06 | 78 | 79 | 78.5 | Sub-oceanic | Upper to mid bathyal (300-800 m) |
| 5R-CC | 256.71 | 75 | 82 | 78.5 | Sub-oceanic | |
| 6R-CC | 268.37 | 93 | 94 | 93.5 | Oceanic | |
| 7R-CC | 280.05 | 55 | 63 | 59 | Extra-neritic | Mid-lower bathyal (800-1000 m) |
| 8R-CC | 285.41 | 81 | 82 | 81.5 | Sub-oceanic | |
| 9R-CC | 297.20 | 36 | 41 | 38.5 | Extra-neritic | |
| 10R-CC | 300.47 | 25 | 29 | 27 | Outer neritic | |
| 11R-6, 31–33 | 317.25 | 33 | 55 | 44 | Extra-neritic | |
| 11R-CC | 319.94 | 82 | 95 | 88.5 | Sub-oceanic | |
| 13F-CC | 334.61 | 73 | 75 | 74 | Sub-oceanic | |
| 14R-CC | 341.71 | 48 | 57 | 52.5 | Extra-neritic | |
| 15R-CC | 352.80 | 27 | 48 | 37.5 | Extra-neritic | |
| 17R-CC | 375.29 | 34 | 64 | 49 | Extra-neritic | |
| 16R-1, 15–17 | 358.67 | 70 | 43 | 56.5 | Extra-neritic | |
| 18R-CC | 377.92 | 34 | 54 | 44 | Extra-neritic | |
| 19R-CC | 396.63 | 38 | 58 | 48 | Extra-neritic | |
| 20R-4, 61–64 | 401.65 | 45 | 44 | 44.5 | Extra-neritic | |
| 20R-CC | 405.97 | 66 | 53 | 59.5 | Extra-neritic | |
| 21R-CC | 407.04 | 44 | 38 | 41 | Extra-neritic | |
| 22R-CC | 426.04 | 41 | 48 | 44.5 | Extra-neritic | |
| 24R-CC | 443.67 | 64 | 58 | 61 | Sub-oceanic | Dysoxic benthic fauna |
| 25R-CC | 450.26 | 4 | 11 | 7.5 | Inner neritic | |
| 26R-CC | 461.36 | 22 | 10 | 16 | Outer neritic | Reworked benthics |
| 27R-CC | 469.6 | 29 | 23 | 26 | Outer neritic | |
| 28R-CC | 478.19 | 55 | 26 | 40.5 | Extra-neritic | |
| 29R-CC | 488.75 | 7 | 4 | 5.5 | Inner neritic | |
| 30R-CC | 497.62 | 38 | 8 | 23 | Outer neritic | |
| 31R-CC | 508.92 | 33 | 9 | 21 | Outer neritic | |
| 32R-CC | 521.07 | 20 | 22 | 21 | Outer neritic | |
| 33R-CC | 528.52 | 6 | 11 | 8.5 | Inner neritic | |
| 34R-CC | 535.57 | 59 | 14 | 36.5 | Extra-neritic | |
| 35R-CC | 544.21 | 20 | 33 | 26.5 | Outer neritic | |
| 36R-CC | 555.75 | | BARREN | | | NA |
| 37R-CC | 568.6 | | BARREN | | | |
| 38R-CC | 580.61 | | BARREN | | | |
| 39R-CC | 589.41 | | BARREN | | | |
| 40R-CC | 598.55 | | BARREN | | | |
| 41R-CC | 608.54 | | BARREN | | | |
| 42R-CC | 613.86 | | BARREN | | | |
| 43R-CC | 623.72 | | BARREN | | | |
| 44R-CC | 630.14 | | BARREN | | | |

**Figure F29 (continued).**

biostratigraphic zones, primarily composed of *Neogloboquadrina incompta*, *Globigerina bulloides*, *Globigerina falconensis*, *Globigerinita glutinata*, *Globigerinoides elongatus*, *Globigerinoides pyramidalis*, *Trilobatus trilobus* group, *Globigerinoides ruber* var. white, *Globoconella inflata*, *Hirsutella scitula*, *Truncorotalia truncatulinoides* s.l. (sinistral and dextral coiling), *Neogloboquadrina pachyderma*, *Orbulina universa*, *Turborotalita quinqueloba*, and *Globigerinella calida* through the Holocene to Middle Pleistocene, with the addition of species such as *Globoturborotalita woodi*, *Globigerinoides obliquus*, *Globigerinoides extremus*, *Neogloboquadrina atlantica* (sinistral and dextral), and *Globoturborotalita decoraperta* through the Lower Pleistocene to Upper Pliocene (Figure **F31**). Common reworked specimens are found throughout the studied interval.
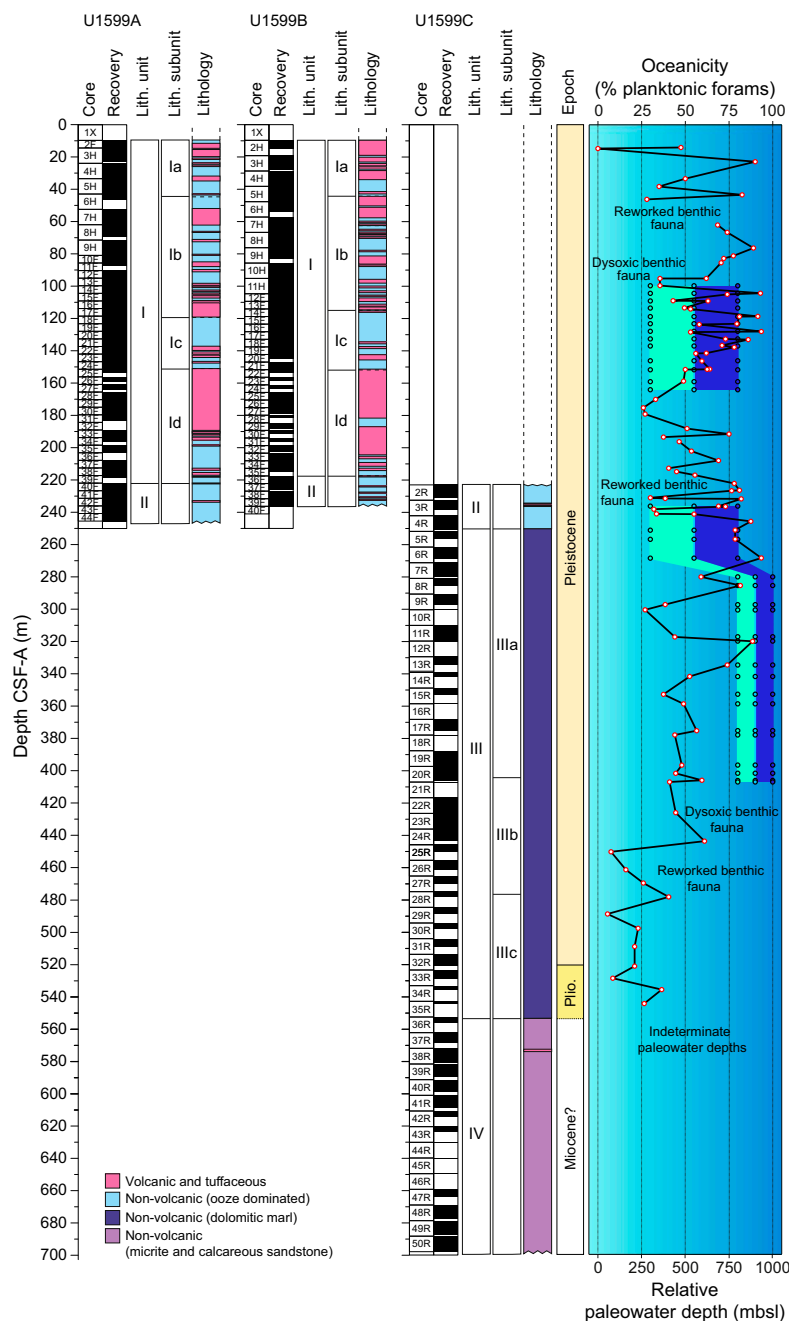


**Figure F30.** Biostratigraphic summary, Site U1599. Interpreted oceanicity: solid line/red points = interpreted oceanicity of Hayward et al. (1999), dashed line = extrapolation through barren/unreliable sample data. Interpreted paleowater depths: light blue points/shading = shallower paleowater depth interpretation, dark blue points/shading = deeper paleowater depth interpretation.

Foraminiferal faunas are sufficiently common to biostratigraphically divide the Pleistocene into the majority of Pleistocene to Upper Pliocene Mediterranean planktonic foraminiferal biostratigraphic zones determined via both primary and secondary marker species (Lirer et al., 2019):

- Zone MPle2b (0.00–0.53 Ma), Hole U1599A: 14.25–151.46 mbsf.
- Zone MPle2a (0.53–0.94 Ma), Holes U1599A, U1599C: 151.6–251.06 mbsf.
- Zone MPle1c (0.94–1.21 Ma), Hole U1599C: 256.71–280.05 mbsf.
- Zone MPle1b (1.21–1.37 Ma), Hole U1599C: 285.41–300.47 mbsf.
- Zone MPle1a (1.37–1.79 Ma), Hole U1599C: 317.25–358.67 mbsf.
- Zone MPl6b (1.79–2.00 Ma), Hole U1599C: 375.29–405.97 mbsf.
- Zone MPl6 (2.00–2.09 Ma), Hole U1599C: 407.04–450.26 mbsf.
- Zones MPl5b-5 (2.09–3.19 Ma), Hole U1599C: 451.36–535.57 mbsf.

The faunal criteria on which these age assignments are based are given in the sections below.

### 6.2.1.1. Zone MPle2b (0.00–0.53 Ma)

Samples 398-U1599A-2F-CC, 0–5 cm, to 24F-CC, 1–3 cm (14.25–151.46 mbsf), are assigned to Zone MPle2b based on the paracme top of sinistrally coiled *Neogloboquadrina* spp. (<0.51 Ma) occurring between Samples 24F-CC, 1–3 cm, and 24F-CC, 15–17 cm (151.46–151.6 mbsf), above which this species is more common. Additionally, *T. truncatulinoides* s.l. (first common occurrence = 0.53) occurs sporadically throughout this interval.
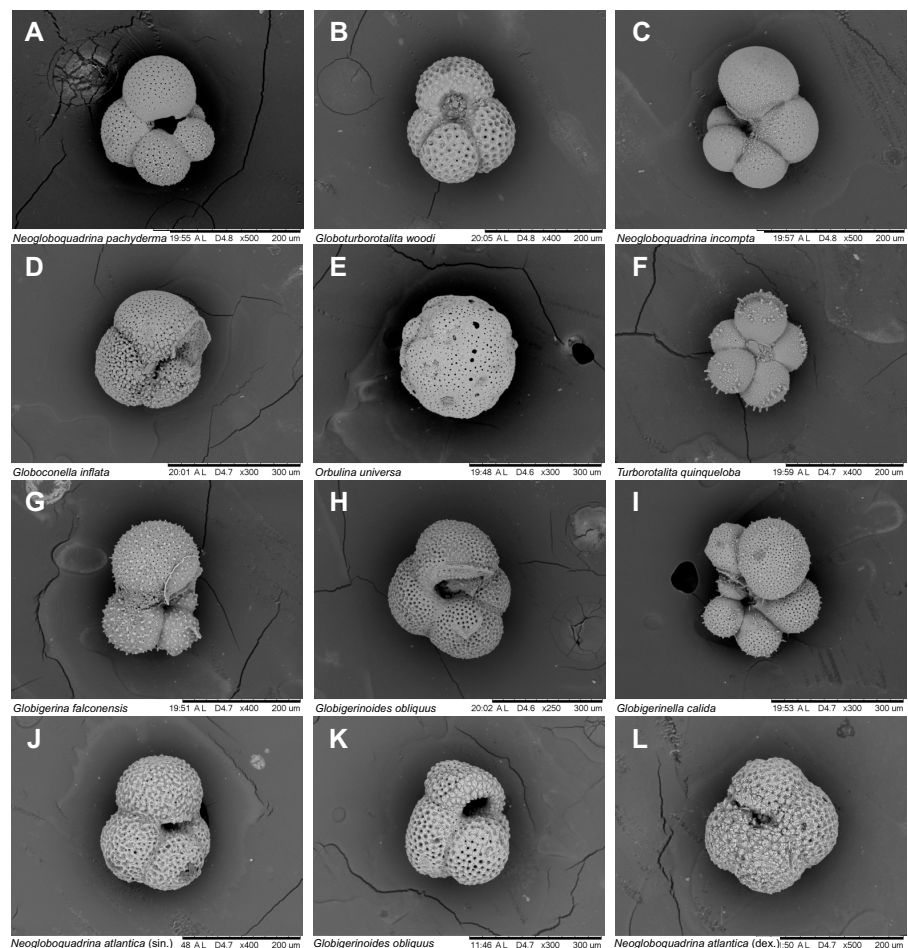


**Figure F31.** Planktonic foraminifera. A. *Neogloboquadrina pachyderma*. B. *Globoturborotalita woodi*. C. *Neogloboquadrina incompta*. D. *Globoconella inflata*. E. *Orbulina universa*. F. *Turborotalita quinqueloba*. G. *Globigerina falconensis*. H. *Globigerinoides obliquus*. I. *Globigerinella calida*. J. *Neogloboquadrina atlantica* (sinistral). K. *Globigerinoides obliquus*. L. *Neogloboquadrina atlantica* (dextral). (A, C, E–G, I: 398-U1599A-5H-CC, 36–41 cm; B, H: 398-U1599C-22R-CC, 0–3 cm; D: 24R-CC, 9–14 cm; J–L: 31R-CC, 20–22 cm.)

### 6.2.1.2. Zone MPle2a (0.53–0.94 Ma)

Samples 398-U1599C-24F-CC, 15–17 cm, to 4R-CC, 9–11 cm (151.6–251.06 mbsf), are assigned to Zone MPle2a based on the absence of *T. truncatulinoides* s.l. (0.53–0.934 Ma) and the sporadic occurrences of sinistrally coiled *Neogloboquadrina* spp. (0.51–0.91 Ma) throughout this interval.

### 6.2.1.3. Zone MPle1c (0.94–1.21 Ma)

Samples 398-U1599C-5R-CC, 0–2 cm, to 7R-CC, 16–19 cm (256.71–300.47 mbsf), are assigned to Zone MPle1c based on the high abundances of sinistrally coiled *Neogloboquadrina* spp. (0.91–1.21 Ma) throughout this interval.

### 6.2.1.4. Zone MPle1b (1.21–1.37 Ma)

Samples 398-U1599C-8R-CC, 24–27 cm, to 10R-CC (285.41–300.47 mbsf) are assigned to Zone MPle1b based on the absence or rare occurrence of sinistrally coiled *Neogloboquadrina* spp. (1.21–1.37 Ma). Moreover, the last occurrence of *G. obliquus* s.s. (last occurrence = 1.28 Ma) is observed in Sample 8R-CC, 24–27 cm (285.41 mbsf).

### 6.2.1.5. Zone MPle1a (1.37–1.79 Ma)

Samples 398-U1599C-11R-6, 31–33 cm, to 16R-1, 15–17 cm (317.25–358.67 mbsf), are assigned to Zone MPle1a based on the first common occurrence of sinistrally coiled *Neogloboquadrina* spp. (1.79 Ma) in Sample 16R-1, 15–17 cm (358.67 mbsf). Additionally, Sample 11R-CC (319.94 mbsf) marks the first common occurrence of the benthic foraminifer *Hyalinea balthica* (1.492 Ma; Lourens et al., 1998).

### 6.2.1.6. Zone MPl6b (1.79–2.00 Ma)

Samples 398-U1599C-17R-CC, 0–2 cm, to 20R-CC, 8–11 cm (375.29–405.97 mbsf), are assigned to Zone MPl6b based on the absence or rare occurrence of sinistrally coiled *Neogloboquadrina* spp (>1.79 Ma) and the first common occurrence of *G. inflata* (1.99 Ma) in Sample 20R-CC, 8–11 cm (405.97 mbsf).

### 6.2.1.7. Zone MPl6 (2.00–2.09 Ma)

Samples 398-U1599C-21R-CC, 0–4 cm, to 25R-CC, 10–15 cm (407.04–450.26 mbsf), are assigned to Zone MPl6 because it represents the interval between the first occurrence of *G. inflata* (2.09 Ma) and the first common occurrence of *G. inflata* (2.00 Ma).

### 6.2.1.8. Zones MPl5b–5 (2.09–3.19 Ma)

Samples 398-U1599C-26R-CC, 9–12 cm, to 34R-CC, 12–15 cm (451.36–535.57 mbsf), are assigned to Zones MPl5b–5 based on the absence of *G. inflata*; the last common occurrence of *G. obliquus* s.s. in Sample 30R-CC, 15–17 cm (497.62 mbsf); and the lowest occurrence of *N. atlantica* (sinistral) in Sample 34R-CC, 12–15 cm (535.57 mbsf). The base of these zones is likely missing due to the presence of a debris flow below this interval. Additionally, there is significant reworking throughout this interval in the form of *Hirsutella margaritae*, *Sphaeroidinellopsis* sp., and *Dentoglobigerina altispira*.

### 6.2.1.9. Nondistinctive Zone (5.33–? Ma)

Downcore of the debris flow underlying Zones MPl5b–5, Samples 398-U1599C-35R-CC, 0–2 cm, to 44R-CC, 1–4 cm (544.21–630.14 mbsf), are assigned to the Nondistinctive Zone or older due to the absence of normal marine planktonic foraminiferal assemblages, and, where present, faunas are dwarfed and exhibit very poor preservation. The microfossil component within this section is primarily composed of rare, moderately preserved Ostracoda. Furthermore, a significant quantity of carbonaceous plant matter and charcoal is present within this interval.

## 6.2.2. Planktonic foraminiferal oceanicity

Planktonic foraminifer abundances are highly variable, ranging 0%–93.5% when foraminifera are present (Figure **F30**). Oceanicity values are generally in agreement with benthic foraminiferal paleowater depth indicators in intervals where reworking is low or absent. In such intervals, the oceanicity data for Site U1599 indicate that relatively consistent extraneritic to suboceanic conditions (100–1000 mbsl) prevailed within Samples 398-U1599A-2F-CC, 0–5 cm, to 398-U1599C-6R-CC, 0–2 cm (14.25–268.37 mbsf). Below this depth, oceanicity values are mostly in disagreement with paleowater depth reconstructions from Samples 398-U1599C-7R-CC, 16–19

cm, to 21R-CC, 0–4 cm (280.05–407.04 mbsf), where oceanicity values continue to indicate shallower conditions. Downcore from this interval, oceanicity values decrease significantly, indicating shallowing conditions approaching Sample 398-U1599C-35R-CC, 0–2 cm (544.21 mbsf), below which oceanicity values are indeterminate.

### 6.2.3. Benthic foraminifera paleowater depths

Benthic foraminiferal distributions are variable, indicating paleowater depths from uppermost bathyal (200–400 m) to lower bathyal (>1000 m) (Figure **F30**). The low abundance or complete absence of benthic foraminiferal faunas in some samples (e.g., 398-U1599A-2F-CC, 0–5 cm, to 10F-CC, 0-3 cm [14.25–85.60 mbsf]; 24F-CC, 15–17 cm, to 26F-CC, 0–5 cm [151.60–158.91 mbsf]; and 398-U1599B-17F-CC, 20–22 cm, to 39F-CC, 18–21 cm [133.18–236.55 mbsf]) are possibly correlated with rapid emplacement of volcaniclastic sediments and/or inhospitable environmental conditions. Samples 398-U1599A-13F-CC, 17 cm, to 34F-CC, 21–23 cm (99.87–196.36 mbsf), record an upper to midbathyal depth (300–800 m), as indicated by the presence of species such as *Cibicides pachyderma* and *Gyroidina* spp., *Cassidulina* spp., *H. balthica*, and *Ioanella tumidula*. Samples 398-U1599C-7R-CC, 16–19 cm, to 21R-CC, 0–4 cm (280.05–407.04 mbsf), exhibit mid- to lower bathyal paleowater depth markers, as indicated by the presence of *Oridorsalis umbonatus*, whereas lower bathyal markers including *Cibicidoides wuellerstorfi* and *Cibicidoides mundulus* also commonly occur. Additionally, samples in various intervals present broken and reworked foraminifer faunas, which in some cases are abundant, as in Sample 398-U1599A-6H-CC, 0–1 cm (46.37 mbsf), and likely represent downslope reworking and sediment transportation. Furthermore, Samples 398-U1599C-26R-CC, 9–12 cm, to 35R-CC, 0–2 cm (461.36–544.21 mbsf), exhibit a lot of reworked specimens and also typical shelf species, potentially suggesting gradual shallowing of the environment. For Sample 398-U1599A-12F-CC, 18–23 cm (95.34 mbsf), and Samples 398-U1599C-22R-CC, 0–3 cm, to 25R-CC, 10–15 cm (426.04–450.26 mbsf), no paleowater depth estimation was possible because of the dominance of dysoxia-tolerant species such as *Bolivina dilatata* and *Bulimina costata* (e.g., Abu-Zied et al., 2008), most possibly representing intervals with high organic matter content.

# 7. Paleomagnetism

Paleomagnetic analysis at Site U1599 focused on measurement and demagnetization of archive-half sections to determine magnetostratigraphic age controls. Three reversal boundaries could be tied with confidence to the geomagnetic polarity timescale (GPTS; Gradstein et al., 2020): (1) the Brunhes/Matuyama transition (0.773 Ma) occurs at 228.3 mbsf (CCSF); (2) the top of the Jaramillo Subchron (C1r.1n; 1.008 Ma) is observed at 250.0 mbsf; and (3) the base of the Jaramillo Subchron (1.076 Ma) occurs at 260.5 mbsf. No magnetostratigraphic correlations were possible deeper than 260.5 mbsf (CCFS) due to a combination of degradation of the record by diagenetic alteration and lack of available independent biostratigraphic markers to aid correlation.

## 7.1. Downhole variations in magnetic characteristics

Remanence measurements were made using the 2G Enterprises Model 760R-4K superconducting rock magnetometer (SRM) system on archive-half section pieces recovered using APC coring in Holes U1599A and U1599B and RCB coring in Hole U1599C. Remanences were measured every 2 cm and were filtered to reject data from points within 8 cm of section ends. This produced a combined site-level data set consisting of natural remanent magnetization (NRM) and alternating field (AF) demagnetization data (after applied fields of 15, 20, and 25 mT) measured at 19,428 intervals downhole. Point MS data obtained from the archive-half sections were also filtered to preserve only data corresponding to the intervals where remanence measurements were made. In addition, 59 discrete samples were subject to AF demagnetization in maximum applied fields of up to 50–100 mT to further constrain magnetic polarities.

Downhole variations in magnetic properties for Holes U1599A, U1599B, and U1599C are shown in Figures **F32**, **F33**, and **F34**, respectively. Declinations of magnetizations are azimuthally unconstrained and show wide variations between cores, as expected. Inclinations are observed to become shallower than the NRM directions following demagnetization, reflecting removal of a

ubiquitous drilling-induced remanent magnetization. Variations in inclinations after demagnetization at 25 mT fall into three zones: (1) from 0 to 190 mbsf in Holes U1599A and U1599B, inclinations are consistently positive and close to the expected geocentric axial dipole (GAD) value of 56° for the site (Figures **F32**, **F33**); (2) below 190 mbsf in Holes U1599A and U1599B and throughout Hole U1599C, inclinations are widely scattered but dominantly positive; and (3) below 550 mbsf, inclinations are dominantly negative (Figure **F34**). The significance of these data for magnetostratigraphic dating is discussed further below. Median destructive fields throughout the sampled sequence are typically 10–25 mT, indicating dominance of low-coercivity magnetic minerals.

We applied an automated principal component analysis (PCA) approach to analyze archive-half section data acquired at higher AF demagnetization steps to identify samples displaying linear decay toward the origin during demagnetization (see **Paleomagnetism** in the Site U1591 chapter [Druitt et al., 2024b]). This involved comparing free-fitting and anchored PCA directions through the 15, 10, and 25 mT step remanences calculated with PuffinPlot software and accepting only those free-fitting PCAs with maximum angular deviations <15° that differ by <15° from the corresponding anchored PCAs. The resulting PCA data set represents the highest quality inclination estimates obtained in each of the holes sampled at Site U1599. We also calculated the Fisher mean directions of the remanences measured at each interval downhole after demagnetization at 15, 20, and 25 mT. For samples where no valid PCA was found, we accepted those Fisher mean directions with precision parameters >15 and $\alpha_{95}$ cones of confidence <15°. Samples that yielded neither statistically acceptable PCAs nor Fisher mean directions were represented in the final site database
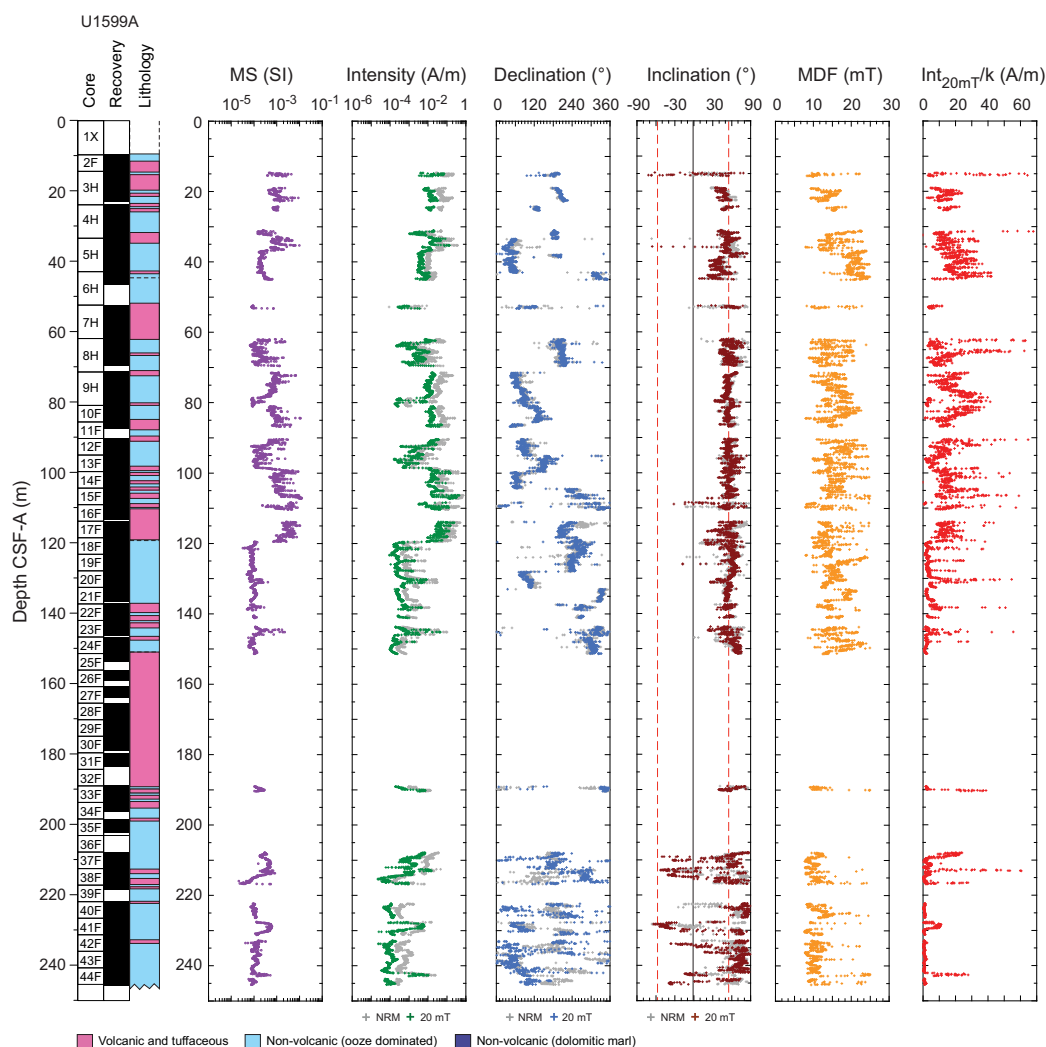


**Figure F32.** Archive-half section magnetic data, Hole U1599A. Red dashed lines = GAD inclinations expected at this site.

by their 25 mT step inclinations. The combination of these three different estimates of inclinations downhole was then used to attempt correlation to the GPTS after converting from the CSF-A to the CCSF depth scale to allow results from all three holes to be placed on a common depth scale.

## 7.2.  Correlations with the geomagnetic polarity timescale

The uppermost 228 m (CCSF) of the sampled sequence carries normal polarity remanences acquired during the Brunhes Chron (C1n; 0–0.773 Ma; Gradstein et al., 2020) (Figure **F35**). The Brunhes/Matuyama transition is placed at 228 mbsf (Figure **F36**), with the reversely magnetized interval 228–250 mbsf assigned to Chron C1r.1r (0.773–1.008 Ma; Gradstein et al., 2020). The Jaramillo Subchron (1.008–1.076 Ma; Gradstein et al., 2020) is present at 250–260.5 mbsf (Figure **F36**). Beneath this, the interval 260.5 to ~360 mbsf (Figures **F36**, **F37**) shows scattered positive and negative inclinations that cannot be tied to the GPTS, probably reflecting disruption of the primary magnetic signal by diagenetic alteration. Inclinations in interval ~360–530 mbsf are of normal polarity and cluster around the expected GAD field inclination of +56° (Figure **F37**). However, biostratigraphic markers suggest that this depth interval should correlate with reversed polarity Chrons C1r.3r, C2r.1r, and C2r.2r, again suggesting remagnetization during diagenesis. Finally, consistently negative inclinations observed in interval 550–674 mbsf (Figure **F37**) indicate that this interval carries reversed magnetization, but the lack of a reliable magnetostratigraphy above this zone and absence of biostratigraphic markers below 543 mbsf make correlation of this reversed interval with the GPTS impossible.
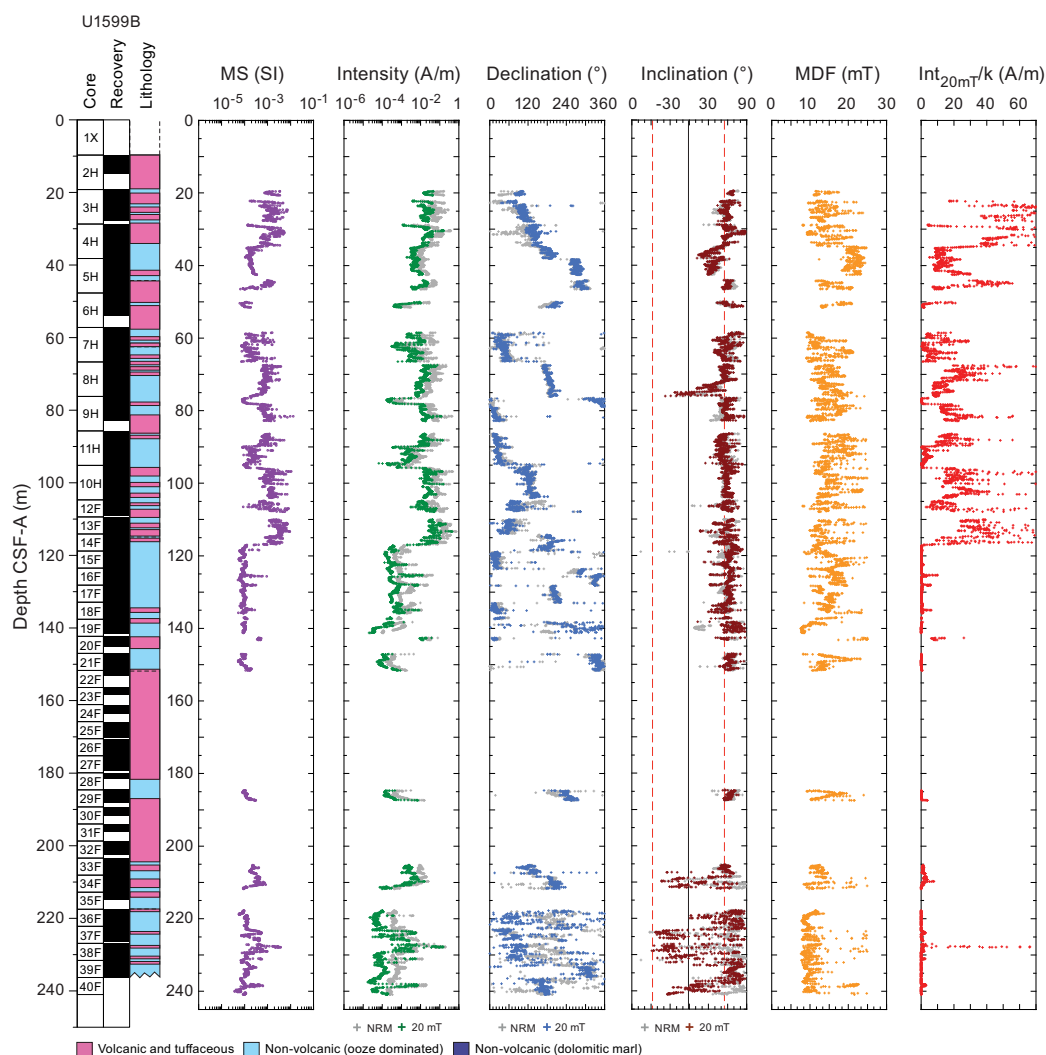


**Figure F33.** Archive-half section magnetic data, Hole U1599B. Red dashed lines = GAD inclinations expected at this site.
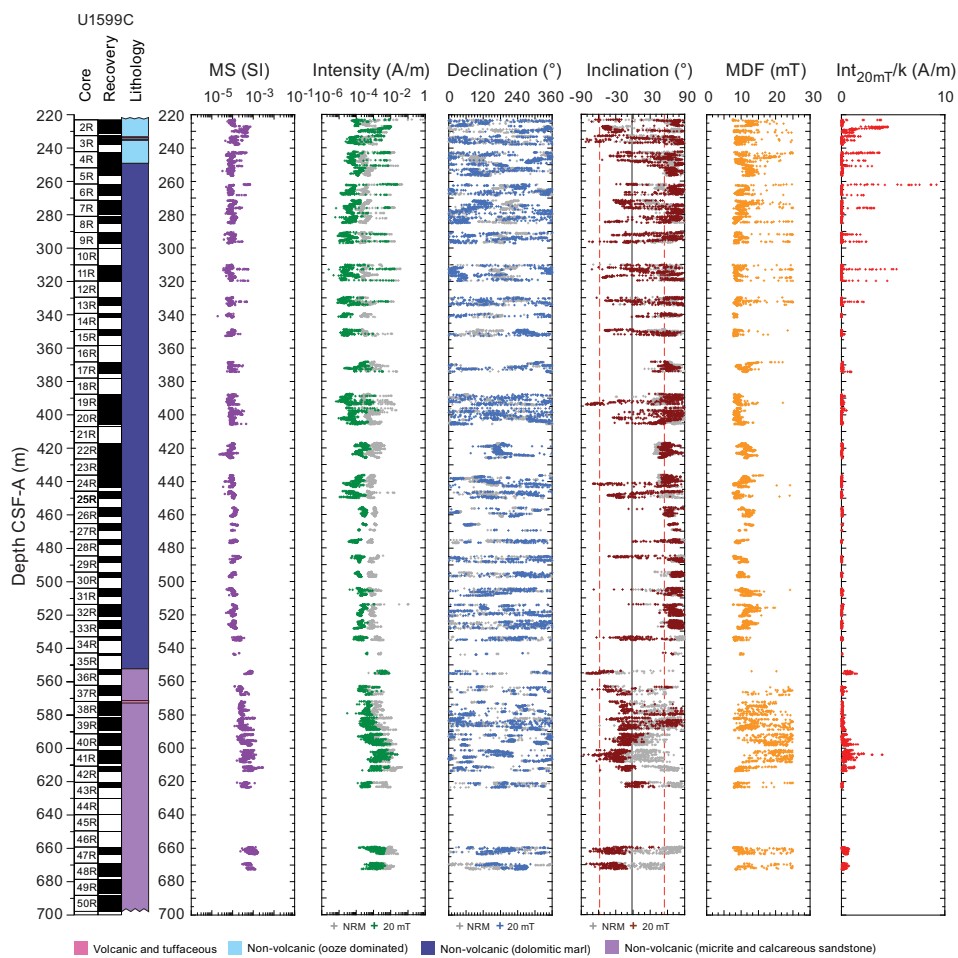
**Figure F34.** Archive-half section magnetic data, Hole U1599C. Red dashed lines = GAD inclinations expected at this site.
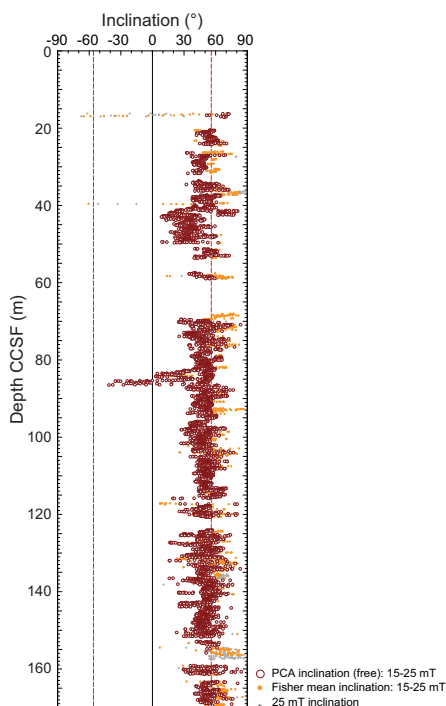


**Figure F35.** Archive-half section magnetic inclinations, Site U1599. Most of the interval correlates to the Brunhes Chron. Red dashed lines = GAD inclinations expected at this site.
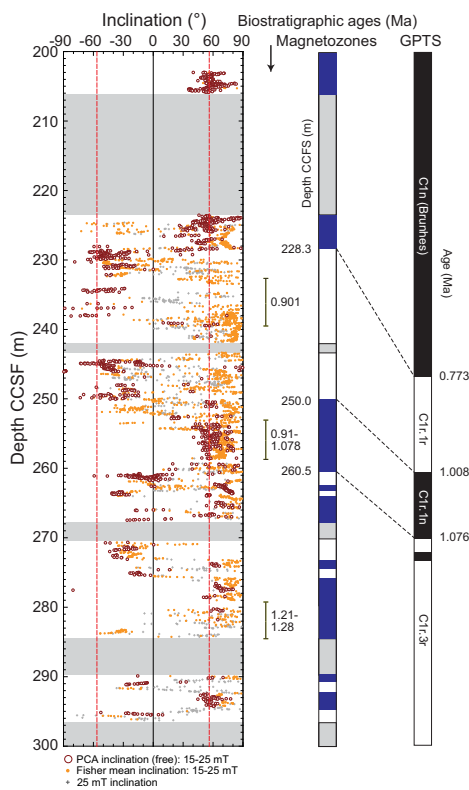
**Figure F36.** Archive-half section magnetic inclinations for 200–300 mbsf, Site U1599. Red dashed lines = GAD inclinations expected at this site. Dark blue/white = normal/reversed polarity magnetozones, gray shading = no available paleomagnetic data. GPTS = geomagnetic polarity timescale.
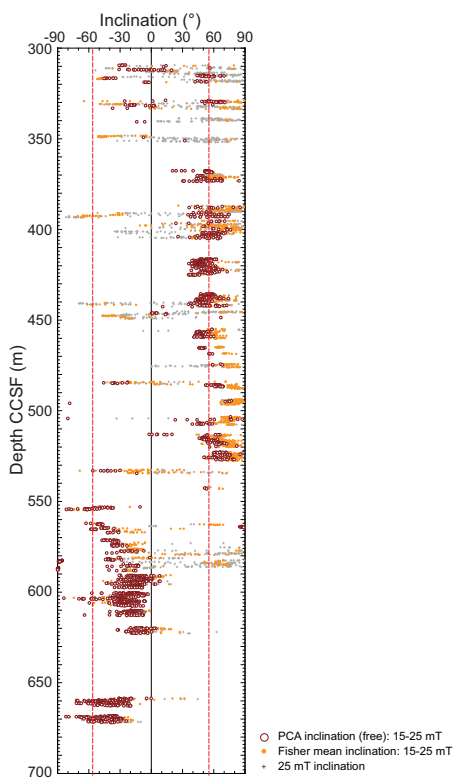


**Figure F37.** Composite archive-half section magnetic inclinations for 300–700 mbsf, Site U1599. Red dashed lines = GAD inclinations expected at this site.

# 8. Physical properties

There is a general trend of increasing *P*-wave velocity, bulk density, and thermal conductivity with increasing depth at Site U1599. MS is highly variable in volcaniclastic layers of Lithostratigraphic Units I and II, and it is sometimes very high. Grain densities in volcanic lapilli layers of Unit I are sometimes <2.0 g/cm³. The dolomitic marls of Unit III have low MS, and *P*-wave velocity increases systematically with increasing depth except for a sandy interval where *P*-wave velocity decreases slightly before increasing more gradually with increasing depth. In the micrites of Unit IV, MS is higher than in Unit III and *P*-wave velocity increases with increasing depth.

## 8.1. Whole-round GRA density, MS, *P*-wave velocity, and NGR

Figure **F38** summarizes data collected on whole-round cores measured on the GRA densitometer, MS loop, and *P*-wave logger on the WRMSL, as well as NGR. All cited depths are on the CSF-A scale. A few possible systematic sources of error in these data should be considered when interpreting absolute values and trends.

- Redistribution of unconsolidated volcaniclastic materials in core liners during APC coring and on the core receiving platform can lead to sorting by particle size and density.
- APC cores often contained large amounts of water. As a result, WRMSL measurements of bulk density are systematically lower than discrete measurements at this site.
- Whole-round measurements in sections that match discrete measurement values on split cores are thus most reliable.

To assess the role of possible disturbance to sediment properties while the core is waiting to be measured, an experiment was undertaken on a typical section containing pumice lapilli. The chosen section does not show the obvious sign of redistribution in the form of an along-section gradient in density (i.e., the pattern in bulk density seen in Figure **F40** in the Site U1592 chapter [Kutterolf et al., 2024b]). Section 398-U1599B-27F-2 was passed through the WRMSL 10 min after the core was divided into sections on the catwalk. The section was then twice passed through the WRMSL 14 h later, with the two repeat measurements separated by 9 min. WRMSL GRA bulk density and MS are shown in Figure **F39**. During the 14 h interval, the section was stored horizon-
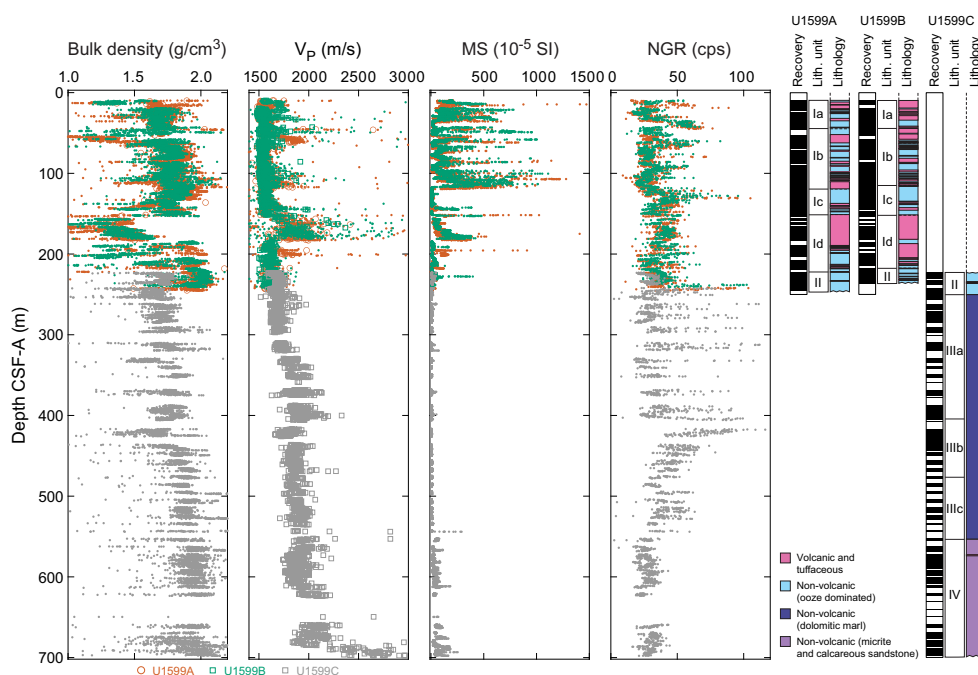


**Figure F38.** Physical properties, Site U1599. Dots = whole-round measurements, open symbols = discrete measurements. MS values >1500 × 10⁻⁵ SI are not shown. *P*-wave velocities >3.0 km/s are not plotted and are tabulated in Table T11. cps = counts per second.

tally and subjected only to the motion of the ship. After the 14 h of repose, one interval of low bulk density had increased in density, and overall there is slightly less variability in density along the section. There is no change in MS, suggesting that the source of MS is mainly minerals contained within pumice lapilli that were too large to be easily redistributed laterally. However, fine-grained ash (glass) with lower MS and higher bulk density than lapilli were able to be redistributed laterally through the framework of larger clasts as the whole core section was repeatedly tilted or handled during transport between instruments and the storage rack. The along-section variation in bulk density was therefore altered without affecting the variation in MS. This experiment highlights that in addition to typical drilling disturbance, physical properties of unconsolidated volcaniclastic material can also potentially be altered by motion of the ship and core handling prior to measurement.

MS is highly variable within the volcaniclastic deposits in Lithostratigraphic Unit I and can be very high (>2500 × 10$^{-5}$ SI; Figure **F38**). High values of MS correspond to volcaniclastic layers. The MS of Unit III is much lower than that of Units I and II and lower than that of Unit IV. NGR is more variable in Unit III than in volcaniclastic-dominated Units I and II and micrites of Unit IV.

Overall, there is no clear systematic increase in bulk density and *P*-wave velocity with increasing depth in Unit I, but there is a monotonic increase in nonsandy marls of Unit III and micrites of Unit IV. Whether the lack of signature of compaction in Unit I is real, a consequence of the limited depth of the holes, or an artifact of drilling and recovery disturbances cannot be readily determined. Lapilli-ash layers that are more than several meters thick (~50 and ~160–180 mbsf) have high *P*-wave velocities.

### 8.1.1. Discrete measurements

#### 8.1.1.1. Material strength
Sediment strength was measured with a pocket penetrometer (PP) on the catwalk immediately after section splitting. Automated vane shear (AVS) strength measurements were made on
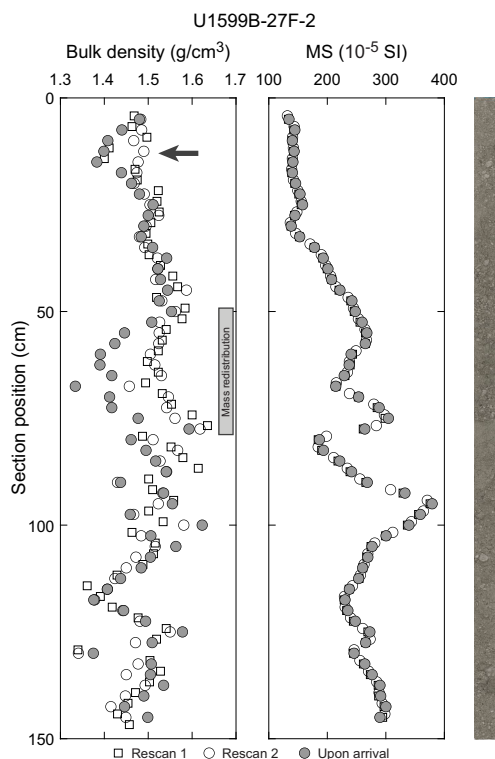


**Figure F39.** Whole-round measurements of bulk density and MS (Section 398-U1599B-27F-2). Image (right) shows archive-half section after subsequent splitting and drying. Bulk density: shading = interval of significant mass redistribution between initial measurement and subsequent rescans, arrow = smaller interval where mass redistribution only occurred between Rescans 1 and 2.

working-half sections. Totals of 22 and 7 AVS measurements were made on working-half sections in Holes U1599A and U1599B, respectively (Figure **F40**; Table **T10**). Totals of 22 and 25 PP measurements were made (Table **T10**) on fine-grained materials that remained intact in core liners upon recovery on the catwalk in Holes U1599A and U1599B, respectively. There is a general trend of increasing shear strength with increasing depth, and the magnitudes of the AVS and PP measurements are similar in the uppermost 150 mbsf.

### 8.1.1.2. *P*-wave velocity

Totals of 651, 616, and 1852 discrete *P*-wave velocity measurements were conducted on Hole U1599A, U1599B, and U1599C working-half sections, respectively (Figure **F40**; Table **T11**). *P*-wave velocity ranges 1.43–4.03 km/s (mean = 1.78 km/s). Discrete measurements of *P*-wave velocity on working-half core sections from Holes U1599A and U1599B are similar to those measured using the WRMSL on whole-round cores (Figure **F38**).

In the uppermost 250 m, there is no clear increase of *P*-wave velocity with increasing depth. In Lithostratigraphic Unit III, in contrast, *P*-wave velocity increases systematically through the non-sandy marls at 250–400 mbsf. *P*-wave velocity increases with increasing depth in Unit IV.

Discrete measurements were sometimes challenging to make in coarse, pumice-rich deposits because signals were especially noisy. Furthermore, particle size was a substantial fraction of the distance between the two calipers used to make the measurements; hence, the measurements may not be representative of true bulk properties (i.e., sample size is not much larger than a representative elementary volume).

### 8.1.1.3. Moisture and density

Totals of 98 and 51 discrete samples were collected from Holes U1599A and U1599C, respectively, to conduct moisture and density (MAD) measurements (Figure **F40**; Table **T12**). Bulk density derived using MAD measurements on discrete samples should be more reliable than GRA density
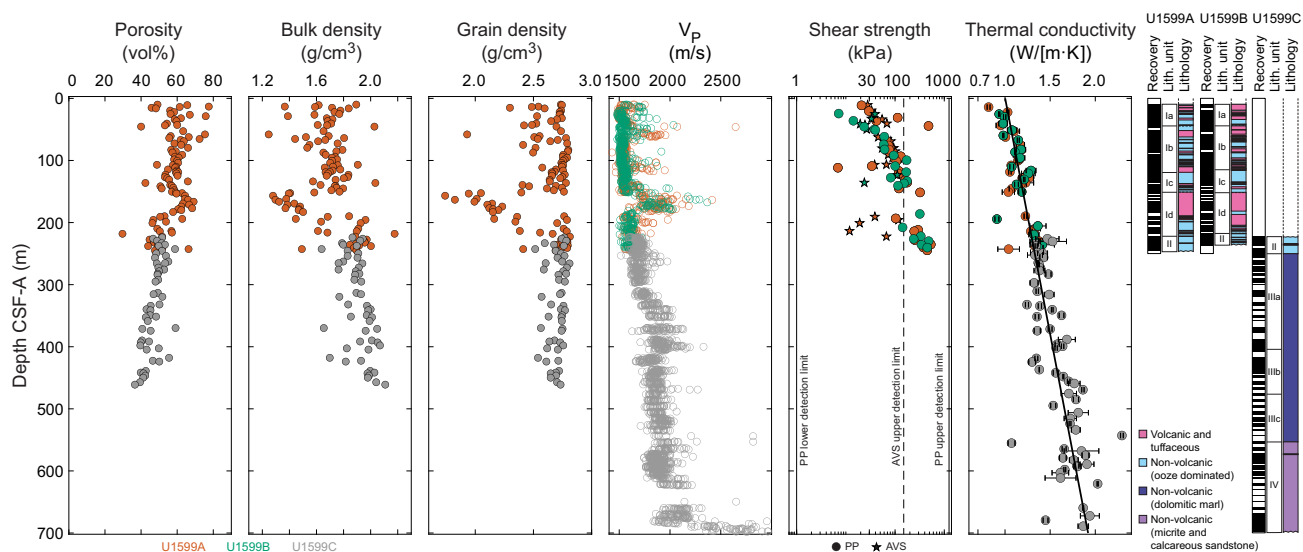


**Figure F40.** Discrete physical properties measurements, Site U1599. *P*-wave velocity values >3.0 km/s are not plotted and are tabulated in Table T11. Dashed line = AVS upper measurement limit, solid lines = PP measurement limits.

**Table T10.** Shear strength, Site U1599. **Download table in CSV format.**

**Table T11.** *P*-wave velocity, Site U1599. **Download table in CSV format.**

**Table T12.** MAD measurements, Site U1599. **Download table in CSV format.**

**Table T13.** Thermal conductivity, Site U1599. **Download table in CSV format.**

data from WRMSL measurements on whole-round cores, although in both cases, coring and recovery disturbances may have impacted measured values.

Porosity ranges 30–78 vol% (mean = 54 vol%; standard deviation = 8 vol%). Bulk density ranges 1.25–2.18 g/cm$^3$ (mean = 1.78 g/cm$^3$). Bulk density is lower in volcaniclastic materials than other lithologies.

Grain density ranges 1.74–2.81 g/cm$^3$ (mean = 2.61 g/cm$^3$; median = 2.70 g/cm$^3$). The lowest values occur in volcaniclastic subunits, mostly in lapilli layers at 120–230 mbsf.

Overall, there is a general trend of decreasing porosity and increasing bulk density with increasing depth. The largest deviation from this general trend occurs in the coarse lapilli between ~160 and 180 mbsf in Subunit Id, where the grain density is also low.

### 8.1.1.4. Thermal conductivity

A total of 107 thermal conductivity measurements were made on selected working-half sections (Table **T13**; Figure **F40**). Measurements could not be made on coarse volcaniclastic materials; hence, the values we report are not representative of the full range of recovered lithologies. A linear fit to the thermal conductivity data is

$$k(z) = (1.002 \pm 0.026) + (1.31 \pm 0.07)z \text{ W/(m·K)},$$

where $z$ is in kilometers and reported ± values are standard errors.

# 9. Geochemistry

## 9.1. Volcaniclastic bulk geochemistry

To determine the geochemistry of the volcanic and tuffaceous materials, nine tephra samples were handpicked from various layers within Hole U1599A. Following cleaning, grinding, fusion, and dissolution, the materials were analyzed shipboard for major (Si, Al, Fe, Mg, and Ca), minor (Ti, Mn, Na, K, and P), and trace (Sc, V, Cr, Co, Ni, Cu, Zn, Rb, Sr, Y, Zr, Nb, Ba, Ce, and Nd) elements using inductively coupled plasma–atomic emission spectroscopy (ICP-AES) (see **Geochemistry** in the Expedition 398 methods chapter [Kutterolf et al., 2024a]). Several unknown samples were run multiple times to determine analytical reproducibility.

### 9.1.1. ICP-AES: major, minor, and trace elements

Of the volcaniclastic units sampled, one was classified as a basalt and eight as dacites (Table **T14**; Figure **F41**). Bulk chemistry values are less evolved than glass chemistry reported in Kutterolf et al. (2021), as expected due to bulk analyses including both minerals and glass.

Concentrations are reported for all analyzed trace elements, but Ce, Cr, Cu, Nb, Ni, P, Rb, S, and V were below detection limits in the majority of samples and are not shown for respective samples in Table **T14**; volcaniclastic analytical errors are ±1% for major elements and ±5%–10% for trace elements (see **Geochemistry** in the Expedition 398 methods chapter [Kutterolf et al., 2024a]). Trace element ratios were used to broadly discriminate between the volcanic centers of Kolumbo, Santorini, and Christiana.

## 9.2. Interstitial water geochemistry

To determine the inorganic constituents of IW, a total of 38 water samples were taken from the mudline and whole-round squeezing of sediment intervals from Holes U1599A (21 samples), U1599B (2 samples), and U1599C (15 samples). Aliquots of IW were used for shipboard analyses, and the remaining water was taken for shore-based analysis following protocols specified by individual scientists. An additional six samples were processed for shore-based analysis only. The retrieved pore waters were analyzed shipboard for salinity, alkalinity, pH, major anions (Cl$^-$, SO$_4^{2-}$,

and Br⁻), major cations ($Ca^{2+}$, $Na^+$, $Mg^{2+}$, and $K^+$), and major (S, Ca, Mg, K, and Na) and minor (B, Ba, Fe, Li, Mn, P, Si, and Sr) elements using the methods described in **Geochemistry** in the Expedition 398 methods chapter (Kutterolf et al., 2024a).

### 9.2.1. Salinity, alkalinity, and pH

Salinity values range 34–46 throughout Site U1599 (Table **T15**; Figure **F42**). The highest salinity value of 46 was recorded at 61.6 mbsf (Section 398-U1599B-7H-3). There are local salinity maxima at 61.6, 199.9, 332.4, and 448.7 mbsf.

**Table T14.** ICP-AES data for major, minor, and trace elements, Site U1599. **Download table in CSV format.**
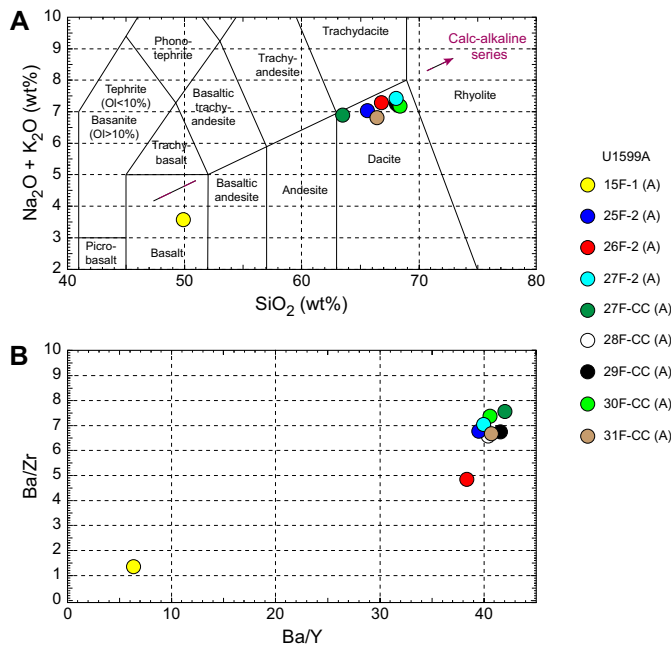


**Figure F41.** ICP-AES analyses of selected volcaniclastic units used to discriminate between potential volcanic sources, Hole U1599A. A. Total alkali vs. $SiO_2$ plot with the rock nomenclature of Le Maitre et al. (2002) overlain used for sample naming. Ol = olivine. B. Ba/Y vs. Ba/Zr plot used to correlate samples.

**Table T15.** Alkalinity, pH, and salinity values, Site U1599. **Download table in CSV format.**
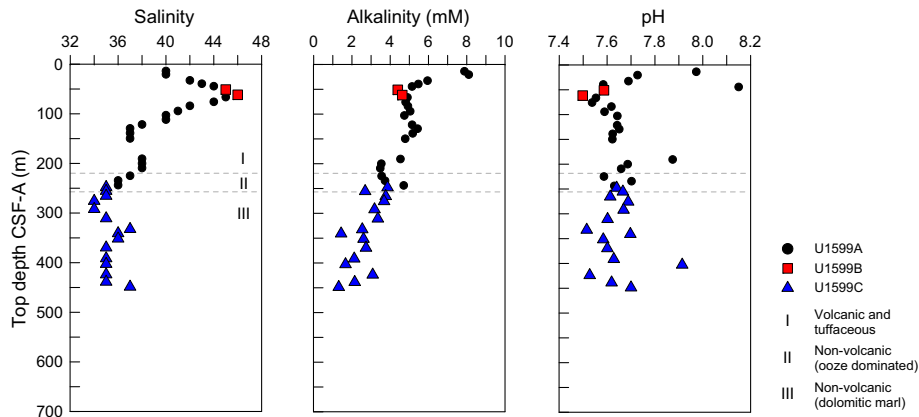


**Figure F42.** IW salinity, alkalinity, and pH, Site U1599. Lithostratigraphic Units I–III are described in Lithostratigraphy.

Alkalinity decreases downhole with some variation. There is a decrease in total alkalinity (7.9–3.7 mM) with depth to just above the base of Hole U1599A at 234.27 mbsf, followed by an increase in the lowermost sample (Table **T15**; Figure **F42**). Hole U1599B exhibits nearly constant alkalinity in the two sampled cores. Hole U1599C shows overall lower alkalinity values than the other two holes, with an overall decrease to a site alkalinity minimum of 1.3 mM at the base of the hole (448.7 mbsf).

Values for pH vary at the sampled depths, ranging 7.5–8.2 (average = 7.7 ± 0.1) (Table **T15**; Figure **F42**).

### 9.2.2. Bromide, chloride, boron, sodium, potassium, magnesium, calcium, and sulfate

Calcium, Mg, K, and $SO_4^{2-}$ follow similar trends and have similar local maxima as salinity, but $Br^-$, $Cl^-$, B, and Na do not (Table **T16**; Figure **F43**). Magnesium, K, and $SO_4^{2-}$ have the most similar profile shapes. Bromide, $Cl^-$, B, and Na initially increase with depth to 66.3 mbsf, similar to salinity; below this depth, they do not have similar local maxima as salinity, Ca, Mg, K, and $SO_4^{2-}$ but instead show less variation with depth.

### 9.2.3. Lithium, strontium, iron, manganese, barium, and silicon

Trends for Sr, Mn, Ba, and Si do not follow salinity, although Li does (Table **T16**; Figure **F44**). Lithium has four maxima at 44.4, 224.9, 351.7, and 448.7 mbsf, all of which are near maxima in Mg, K, $SO_4^{2-}$, and salinity. Strontium increases with depth to a maximum of 711.6 µM at 292 mbsf

**Table T16.** IW data for major anions and cations measured using ion chromatography and major and minor elements measured using ICP-AES, Site U1599. **Download table in CSV format.**
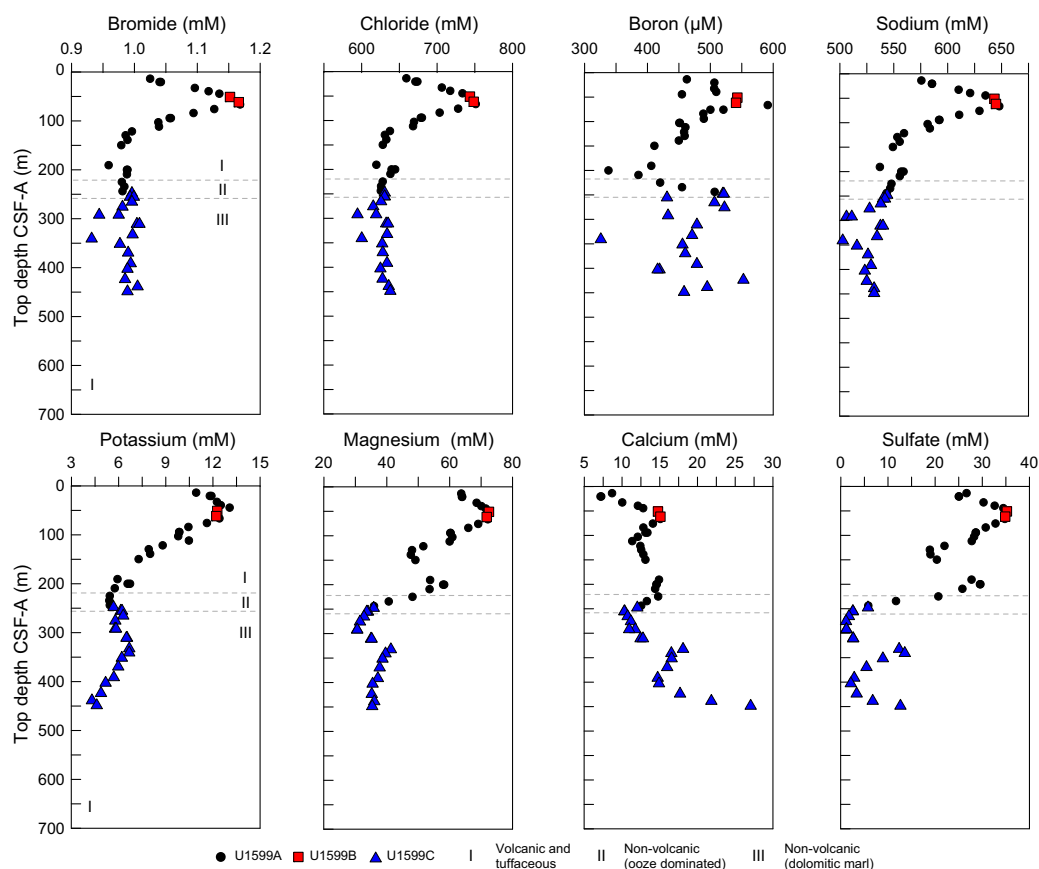


**Figure F43.** IC and ICP-AES concentrations of Br, Cl, B, Na, K, Mg, Ca, and $SO_4^{2-}$ in IW samples, Site U1599. Lithostratigraphic Units I–III are described in Lithostratigraphy.

before decreasing downhole. Manganese is elevated in the uppermost 150 m and has lower values with slight variations at depth. Iron was only detectable in nine samples that occurred in regions with elevated Mn concentrations. Barium is near zero in all samples except at 250–325 mbsf and again at 375–425 mbsf, corresponding to minima in $SO_4^{2-}$. There are no clear trends for IW Si concentrations, and P is below detection limit in all but one sample.

## 9.3. Sediment bulk geochemistry

A total of 39 sediment samples were analyzed for bulk geochemistry (Table **T17**). All were analyzed for total carbon, hydrogen, and nitrogen (CHN) and for inorganic carbon and carbonate content following the protocols explained in **Geochemistry** in the Expedition 398 methods chapter (Kutterolf et al., 2024a). For CHN analysis, duplicates were run for ~10% of the samples to determine analytical reproducibility (standard deviations: N = 0.01; C = 0.04) (Figure **F45**).
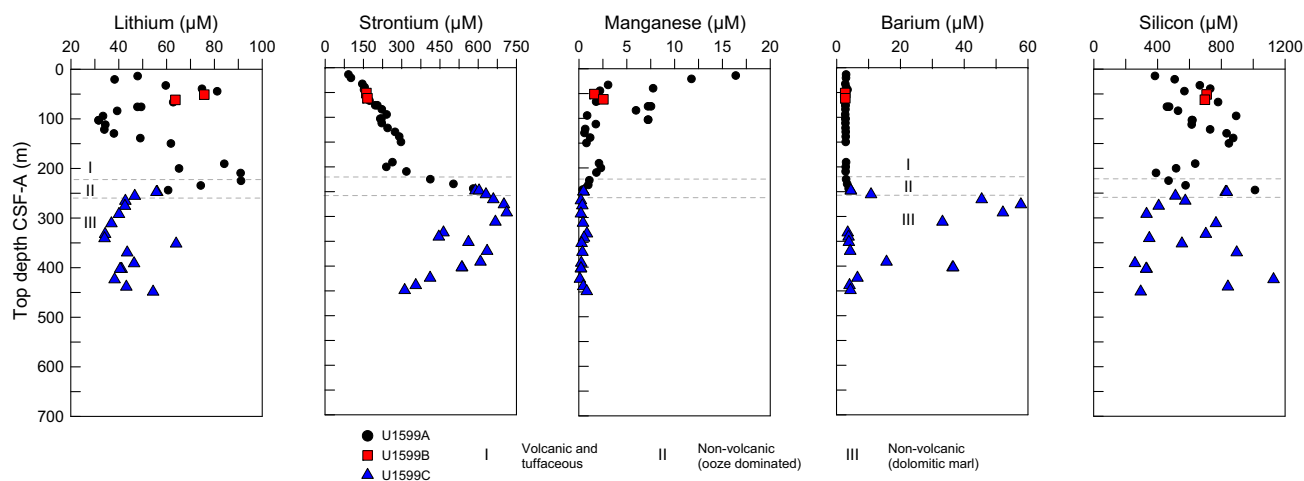


**Figure F44.** ICP-AES concentrations of Li, Sr, Mn, Ba, and Si in IW samples, Site U1599. Lithostratigraphic Units I–III are described in Lithostratigraphy.

**Table T17.** Total inorganic carbon, percent CaCO₃, total carbon, total nitrogen, and TOC data, Site U1599. **Download table in CSV format.**
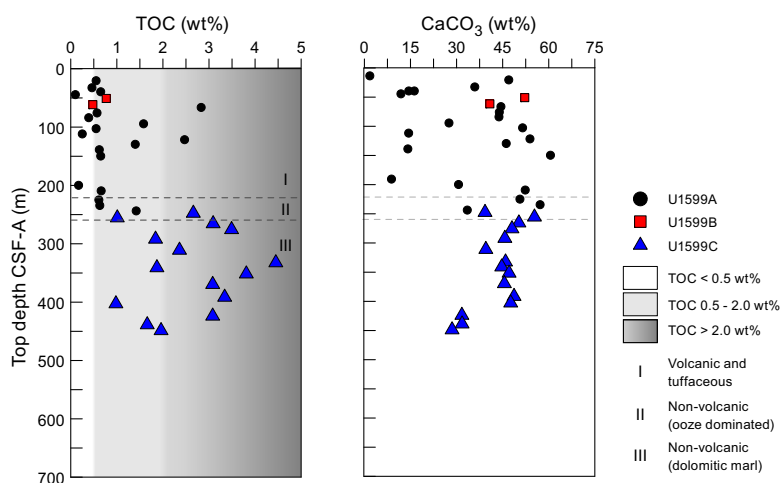


**Figure F45.** TOC and carbonate, Site U1599. Lithostratigraphic Units I–III are described in Lithostratigraphy. Sapropel units follow Kidd et al. (1978).

### 9.3.1. Sapropel identification

Total organic carbon (TOC) was calculated using total carbon and inorganic carbon values. Following the convention set forth by Kidd et al. (1978), units with TOC values >2.0 wt% were identified as sapropels, and units with TOC of 0.5–2.0 wt% were identified as sapropelitic. Using these values, 19 units were identified as sapropelitic and 11 units were identified as sapropels (Figure **F45**).

## 9.4. Headspace gas analysis

Headspace gas analyses were performed at a resolution of one sample per full-length core (9.5 m advance) throughout Hole U1599A. The aim was to monitor the presence and abundance of $C_1$–$C_3$ hydrocarbons as part of the standard IODP safety protocol (Pimmel and Claypool, 2001). A total of 26 headspace gas samples from this hole were analyzed using gas chromatography (GC) (see **Geochemistry** in the Expedition 398 methods chapter [Kutterolf et al., 2024a]). Methane, ethane, and propane concentrations were below the detection limit throughout Hole U1599A.

Headspace gas analyses were resumed on Hole U1599C when a depth was reached that exceeded that of Hole U1599A (247.7 mbsf). Below this depth, headspace gas analyses were performed at a resolution of one sample per core to the base of the hole. A total of 45 headspace gas samples were analyzed using GC. Methane concentrations in Hole U1599C increased between 266 and 311 mbsf, reaching a maximum of 816.3 ppmv at 275.7 mbsf before returning to below detection limit to the base of the hole. Methane, ethane, and propane concentrations were below the detection limit in all other samples.

# 10. Microbiology

A total of 35 whole-round core samples were collected for microbiological analyses (Table **T18**). After the cores were transferred to the core receiving platform, the whole-round samples were collected based on the sediment color. Reddish to orange coloration was used as an indicator for iron-rich layers that often host the microbial communities we sought. To choose the appropriate incubation temperature, the core temperature was measured in the section above the sample.

The whole rounds were transferred to the microbiology laboratory, and the following subsamples were collected for microbial community composition analysis, metagenomics, cell counting, microscope, and microbial cultivation: POLYmeta, POLYmicro, POLYanae, POLYcell, POLYFe, POLYmicroscope, and POLYFe-agar.

In total, 246 subsamples were collected for microbiological analysis from the whole-round core samples.

**Table T18.** Whole-round core samples, Site U1599. **Download table in CSV format.**

# References

Abu-Zied, R.H., Rohling, E.J., Jorissen, F.J., Fontanier, C., Casford, J.S.L., and Cooke, S., 2008. Benthic foraminiferal response to changes in bottom-water oxygenation and organic carbon flux in the eastern Mediterranean during LGM to Recent times. Marine Micropaleontology, 67(1–2):46–68. **https://doi.org/10.1016/j.marmicro.2007.08.006**

Backman, J., Raffi, I., Rio, D., Fornaciari, E., and Pälike, H., 2012. Biozonation and biochronology of Miocene through Pleistocene calcareous nannofossils from low and middle latitudes. Newsletters on Stratigraphy, 45(3):221–244. **https://doi.org/10.1127/0078-0421/2012/0022**

Brothers, R.J., Kemp, A.E.S., and Maltman, A.J., 1996. Mechanical development of vein structures due to the passage of earthquake waves through poorly-consolidated sediments. Tectonophysics, 260(4):227–244. **https://doi.org/10.1016/0040-1951(96)00088-1**

Di Stefano, A., and Sturiale, G., 2010. Refinements of calcareous nannofossil biostratigraphy at the Miocene/Pliocene Boundary in the Mediterranean region. Geobios, 43(1):5–20. **https://doi.org/10.1016/j.geobios.2009.06.007**

Druitt, T., Kutterolf, S., and Höfig, T.W., 2022. Expedition 398 Scientific Prospectus: Hellenic Arc Volcanic Field. International Ocean Discovery Program. **https://doi.org/10.14379/iodp.sp.398.2022**

Druitt, T.H., Kutterolf, S., Ronge, T.A., Beethe, S., Bernard, A., Berthod, C., Chen, H., Chiyonobu, S., Clark, A., DeBari, S., Fernandez Perez, T.I., Gertisser, R., Hübscher, C., Johnston, R.M., Jones, C., Joshi, K.B., Kletetschka, G., Koukousioura, O., Li, X., Manga, M., McCanta, M., McIntosh, I., Morris, A., Nomikou, P., Pank, K., Peccia, A., Polymenakou, P.N., Preine, J., Tominaga, M., Woodhouse, A., and Yamamoto, Y., 2024a. Site U1589. In Druitt, T.H., Kutterolf, S., Ronge, T.A., and the Expedition 398 Scientists, Hellenic Arc Volcanic Field. Proceedings of the International Ocean Discovery Program, 398: College Station, TX (International Ocean Discovery Program). **https://doi.org/10.14379/iodp.proc.398.103.2024**

Druitt, T.H., Kutterolf, S., Ronge, T.A., Beethe, S., Bernard, A., Berthod, C., Chen, H., Chiyonobu, S., Clark, A., DeBari, S., Fernandez Perez, T.I., Gertisser, R., Hübscher, C., Johnston, R.M., Jones, C., Joshi, K.B., Kletetschka, G., Koukousioura, O., Li, X., Manga, M., McCanta, M., McIntosh, I., Morris, A., Nomikou, P., Pank, K., Peccia, A., Polymenakou, P.N., Preine, J., Tominaga, M., Woodhouse, A., and Yamamoto, Y., 2024b. Site U1591. In Druitt, T.H., Kutterolf, S., Ronge, T.A., and the Expedition 398 Scientists, Hellenic Arc Volcanic Field. Proceedings of the International Ocean Discovery Program, 398: College Station, TX (International Ocean Discovery Program). **https://doi.org/10.14379/iodp.proc.398.105.2024**

Expedition 334 Scientists, 2012. Expedition 334 summary. In Vannucchi, P., Ujiie, K., Stroncik, N., and the Expedition 334 Scientists, Proceedings of the Integrated Ocean Drilling Program. 334: Tokyo (Integrated Ocean Drilling Program Management International, Inc.). **https://doi.org/10.2204/iodp.proc.334.101.2012**

Fisher, R.V., and Schmincke, H.-U., 1984. Pyroclastic Rocks: Berlin (Springer). **https://doi.org/10.1007/978-3-642-74864-6**

Gradstein, F.M., Ogg, J.G., Schmitz, M.D., and Ogg, G.M. (Eds.), 2020. The Geologic Time Scale 2020: Amsterdam (Elsevier BV). **https://doi.org/10.1016/C2020-1-02369-3**

Hanamura, Y., and Ogawa, Y., 1993. Layer-parallel faults, duplexes, imbricate thrusts and vein structures of the Miura Group: keys to understanding the Izu fore-arc sediment accretion to the Honshu fore arc. Island Arc, 2(3):126–141. **https://doi.org/10.1111/j.1440-1738.1993.tb00081.x**

Hayward, B.W., Grenfell, H.R., Reid, C.M., and Hayward, K.A., 1999. Recent New Zealand shallow-water benthic foraminifera: taxonomy, ecologic distribution, biogeography, and use in paleoenvironmental assessment. In Institute of Geological & Nuclear Sciences Monograph, 21: Lower Hutt, NZ.

Hooft, E.E.E., Nomikou, P., Toomey, D.R., Lampridou, D., Getz, C., Christopoulou, M.-E., O'Hara, D., Arnoux, G.M., Bodmer, M., Gray, M., Heath, B.A., and VanderBeek, B.P., 2017. Backarc tectonism, volcanism, and mass wasting shape seafloor morphology in the Santorini-Christiana-Amorgos region of the Hellenic Volcanic Arc. Tectonophysics, 712–713:396–414. **https://doi.org/10.1016/j.tecto.2017.06.005**

Jutzeler, M., White, J.D.L., Talling, P.J., McCanta, M., Morgan, S., Le Friant, A., and Ishizuka, O., 2014. Coring disturbances in IODP piston cores with implications for offshore record of volcanic events and the Missoula megafloods. Geochemistry, Geophysics, Geosystems, 15(9):3572–3590. **https://doi.org/10.1002/2014GC005447**

Kidd, R.B., Cita, M.B., and Ryan, W.B.F., 1978. Stratigraphy of eastern Mediterranean sapropel sequences recovered during DSDP Leg 42A and their paleoenvironmental significance. In Hsü, K., Montadert, L., et al., Initial Reports of the Deep Sea Drilling Project. 42(1): Washington, DC (US Government Printing Office), 421–443. **https://doi.org/10.2973/dsdp.proc.42-1.113-1.1978**

Kutterolf, S., Druitt, T.H., Ronge, T.A., Beethe, S., Bernard, A., Berthod, C., Chen, H., Chiyonobu, S., Clark, A., DeBari, S., Fernandez Perez, T.I., Gertisser, R., Hübscher, C., Johnston, R.M., Jones, C., Joshi, K.B., Kletetschka, G., Koukousioura, O., Li, X., Manga, M., McCanta, M., McIntosh, I., Morris, A., Nomikou, P., Pank, K., Peccia, A., Polymenakou, P.N., Preine, J., Tominaga, M., Woodhouse, A., and Yamamoto, Y., 2024a. Expedition 398 methods. In Druitt, T.H., Kutterolf, S., Ronge, T.A., and the Expedition 398 Scientists, Hellenic Arc Volcanic Field. Proceedings of the International Ocean Discovery Program, 398: College Station, TX (International Ocean Discovery Program). **https://doi.org/10.14379/iodp.proc.398.102.2024**

Kutterolf, S., Druitt, T.H., Ronge, T.A., Beethe, S., Bernard, A., Berthod, C., Chen, H., Chiyonobu, S., Clark, A., DeBari, S., Fernandez Perez, T.I., Gertisser, R., Hübscher, C., Johnston, R.M., Jones, C., Joshi, K.B., Kletetschka, G., Koukousioura, O., Li, X., Manga, M., McCanta, M., McIntosh, I., Morris, A., Nomikou, P., Pank, K., Peccia, A., Polymenakou, P.N., Preine, J., Tominaga, M., Woodhouse, A., and Yamamoto, Y., 2024b. Site U1592. In Druitt, T.H., Kutterolf, S., Ronge, T.A., and the Expedition 398 Scientists, Hellenic Arc Volcanic Field. Proceedings of the Inter-

national Ocean Discovery Program, 398: College Station, TX (International Ocean Discovery Program). **https://doi.org/10.14379/iodp.proc.398.106.2024**

Kutterolf, S., Freundt, A., Hansteen, T.H., Dettbarn, R., Hampel, F., Sievers, C., Wittig, C., Allen, S.R., Druitt, T.H., McPhie, J., Nomikou, P., Pank, K., Schindlbeck-Belo, J.C., Wang, K.-L., Lee, H.-Y., and Friedrichs, B., 2021. The medial offshore record of explosive volcanism along the central to eastern Aegean Volcanic Arc: 1. tephrostratigraphic correlations. Geochemistry, Geophysics, Geosystems, 22(12):e2021GC010010. **https://doi.org/10.1029/2021GC010010**

Le Maitre, R.W., Steckeisen, A., Zanettin, B., Le Bas, M.J., Bonin, B., and Bateman, P. (Eds.), 2002. Igneous Rocks: A Classification and Glossary of Terms (Second edition): Cambridge, UK (Cambridge University Press). **https://doi.org/10.1017/CBO9780511535581**

Lirer, F., Foresi, L.M., Iaccarino, S.M., Salvatorini, G., Turco, E., Cosentino, C., Sierro, F.J., and Caruso, A., 2019. Mediterranean Neogene planktonic foraminifer biozonation and biochronology. Earth-Science Reviews, 196:102869. **https://doi.org/10.1016/j.earscirev.2019.05.013**

Lourens, L.J., Hilgen, F.J., and Raffi, I., 1998. Base of large Gephyrocapsa and astronomical calibration of early Pleistocene sapropels in Site 967 and Hole 969D: solving the chronology of the Vrica Section (Calabria, Italy). In Robertson, A.H.F., Emeis, K.-C., Richter, C., and Camerlenghi, A. (Eds.), Proceedings of the Ocean Drilling Program, Scientific Results. 160: College Station, TX (Ocean Drilling Program), 191. **https://doi.org/10.2973/odp.proc.sr.160.017.1998**

Maltman, A.J., Byrne, T., Karig, D.E., and Lallemant, S., 1993. Deformation at the toe of an active accretionary prism: synopsis of results from ODP Leg 131, Nankai, SW Japan. Journal of Structural Geology, 15(8):949–964. **https://doi.org/10.1016/0191-8141(93)90169-B**

Martini, E., 1971. Standard Tertiary and Quaternary calcareous nannoplankton zonation. Proceedings of the Second Planktonic Conference, Roma, 1970:739–785.

Okada, H., and Bukry, D., 1980. Supplementary modification and introduction of code numbers to the low-latitude coccolith biostratigraphic zonation (Bukry, 1973; 1975). Marine Micropaleontology, 5(3):321–325. **https://doi.org/10.1016/0377-8398(80)90016-X**

Pimmel, A., and Claypool, G., 2001. Introduction to shipboard organic geochemistry on the JOIDES Resolution. Ocean Drilling Program Technical Note, 30. **https://doi.org/10.2973/odp.tn.30.2001**

Preine, J., Hübscher, C., Karstens, J., and Nomikou, P., 2022a. Volcano-tectonic evolution of the Christiana-Santorini-Kolumbo rift zone. Tectonics, 41(11):e2022TC007524. **https://doi.org/10.1029/2022TC007524**

Preine, J., Karstens, J., Hübscher, C., Nomikou, P., Schmid, F., Crutchley, G.J., Druitt, T.H., and Papanikolaou, D., 2022b. Spatio-temporal evolution of the Christiana-Santorini-Kolumbo volcanic field, Aegean Sea. Geology, 50(1):96–100. **https://doi.org/10.1130/G49167.1**

Rio, D., Raffi, I., and Villa, G., 1990. Pliocene-Pleistocene calcareous nannofossil distribution patterns in the western Mediterranean. In Kastens, K.A., Mascle, J., et al., Proceedings of the Ocean Drilling Program, Scientific Results. 107: College Station, TX (Ocean Drilling Program), 513–533. **https://doi.org/10.2973/odp.proc.sr.107.164.1990**

Shipboard Scientific Party, 2001. Leg 190 summary. In Moore, G.F., Taira, A., Klaus, A., et al., Proceedings of the Ocean Drilling Program, Initial Reports, 190. College Station, TX (Ocean Drilling Program), 1–87. **https://doi.org/10.2973/odp.proc.ir.190.101.2001**

Sibson, R.H., 1981. Controls on low-stress hydro-fracture dilatancy in thrust, wrench and normal fault terrains. Nature, 289(5799):665–667. **https://doi.org/10.1038/289665a0**